

学位論文

Search for Proton Decay Using an Improved Event
Reconstruction Algorithm in Super-Kamiokande

(スーパーカミオカンデにおける改良型
事象再構成アルゴリズムを用いた陽子崩壊探索)

平成29年5月博士（理学）申請

東京大学大学院理学系研究科

物理学専攻

須田 祐介

Abstract

Most of grand unified theories predict proton decay as a result of baryon number violation, which has not been found so far. The proton decay mode of $p \rightarrow e^+\pi^0$ is predicted as the most dominant decay mode in many non-super-symmetric grand unified theories. In this thesis, we discuss the result of a search for $p \rightarrow e^+\pi^0$ in Super-Kamiokande. We collect 483 live days data from 4973 live days to 5456 live days since the latest published paper [1]. Almost half of all data is collected by a new electronics which enables us to reduce the background rate by approximately half using a neutron tagging technique. A newly developed event reconstruction algorithm is applied to the data with the new electronics. This new algorithm is able to extend the fiducial volume by 10% from 22.5 kton to 24.7 kton and reduce the background rate by about 30% compared to the conventional analysis while keeping the same level of the signal efficiency. We analyze the 179.5 kton-years data (from September 2008 to August 2016) by using the new algorithm and find no candidate for this decay mode. By combining with zero-observation results of a conventional algorithm in the 172.5 kton-years data (from the beginning of the experiment to August 2008) [1], the lifetime limit for $p \rightarrow e^+\pi^0$ is set to be $\tau/B > 1.88 \times 10^{34}$ years at 90 % confidence level. This limit is 18% longer than that of the latest published paper and the current most stringent constraint on non-super-symmetric grand unified theories in the world.

Acknowledgments

I am deeply grateful to my supervisor, Masashi Yokoyama for his enormous support and patience. He gave me a lot of appropriate advice every important point. I strongly remember the encouragement he gave me when I was about to have a breakdown after I opened the data. My thesis would never completed without his guidance.

I would like to thank all of previous and current Super-Kamiokande collaborators, especially the following people: Masayuki Nakahata, Masato Shiozawa, Shigetaka Moriyama, Yoshinari Hayato, Roger Wendell, Makoto Miura, Jun Kameda, Shoei Nakayama, Hidekazu Tanaka, Ed Kearns, Chris Walter and Shunichi Mine. Shiozawa-san's insightful comments were always helpful for my analysis. I learned a lot of things related to our proton decay analysis from Miura-san. I was trained by Mine-san the presentation skill.

I also thank Kimihiro Okumura, Yasuhiro Nishimura and Euan Richard for helping my works on the FC reduction during the expert period.

A crucial element of this thesis is the new event reconstruction algorithm, fitQun. I would like to express my gratitude to the members of the fitQun working group: Sophie Berkman, Patrick de Perio, Miao Jiang, Akira Konaka, Andy Missert, Hirohisa Tanaka, Shimpei Tobayama, Mike Wilking and Eric Zimmerman. My special thanks go to Tobayama-san who introduced me fitQun and gave me many important suggestions. His passionate attitude to research was highly impressive. I appreciate the support from Mine-san, Tobayama-san and Jiang-san on many fitQun studies, especially on its energy scale study.

I spend most of time during my master and doctoral programs in Kamioka. I thank the following people made my Kamioka life happy: Tomonobu Tomura, Hiroyoshi Uchida, Kunxian Huang, Seiko Hirota, Shota Takahashi, Keishi Hosokawa, Yuki Nakano, Osamu Takachio, Hiroki Takiya, Naoya Oka, Katsuma Nakagawa, Yuto Haga, Isao Kametani, Keiji Tateishi, Yosuke Ohnishi, Masatoshi Kobayashi, Yuji Okajima, Asato Orii, Ryosuke Akutsu, Daisuke Fukuda, Fumimasa Muto, Yutaro Sonoda and all of the Kamioka Observatory member. Talking with Tomura-san and my friends was always fun and essential to survive in Kamioka. Life in Kamioka made me stronger as a person.

I also thank my college friends: Shion Chen, Chikuma Kato, Chihiro Kozaikai, Tatsuya Mori, Miki Nishimura, Takanao Tsuyuki and Harumichi Yokoyama.

I would like to show my appreciation to the members in my lab: Hiroaki Aihara, Yoshiyuki Onuki, Denis Epifanov, Ian Watson, Konosuke Iwamoto, Sogo

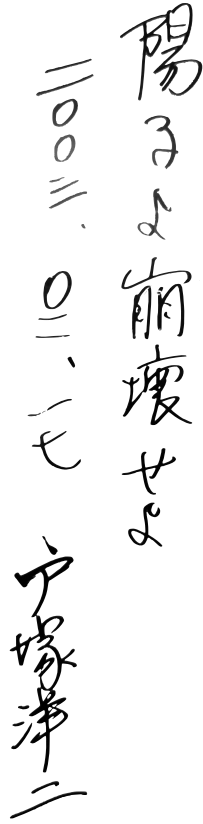


Figure 1: Word by Yoji Totsuka. It is pronounced as “*Yohshi-yo Hohkai-seyo*” which literally means “*Decay, protons*”.

Mineo, Clement Ng, Yasutaka Kanazawa, Nobuhiro Shimizu, Taichiro Koga, Junya Sasaki, Yifan Jin, Naruhiro Chikuma, Fuminao Hosomi, Hiroko Niikura, Tianmeng Lou, Alejandro Mora Grimaldo Johnny, Wan Kun, Tatsuki Ose, Riku Tamura, Ryo Fujita and Kuniko Kono.

My deep appreciation goes to my family and friends Kohei Kato, Takeru Kageyama, Kaito Sasaki and Kanako Katayama.

Finally, I want to thank the word written by Yoji Totsuka on February 17, 2003, as shown in Figure 1. He was the first spokesperson of Super-Kamiokande and hoped that proton decay is observed. This word strongly motivated me to search for proton decay and always gave me a hope. I hope that protons hear our wish someday in the future.

Contents

1	Introduction	1
2	Physics motivation	4
2.1	Standard Model and its Problems	4
2.2	Grand Unified Theories	5
2.2.1	$SU(5)$ Model	5
2.2.2	SUSY $SU(5)$ Model	6
2.2.3	$SO(10)$ Model	7
2.2.4	Proton Decay Search	8
3	Super-Kamiokande Experiment	10
3.1	Overview	10
3.2	Principle of the Detector	11
3.3	Water and Air	15
3.4	Photosensors	15
3.5	Data Acquisition	17
3.5.1	System for SK-I to SK-III	17
3.5.2	System for SK-IV	19
3.6	Detector Calibration	19
3.6.1	PMT Gain	20
3.6.2	PMT Timing	22
3.6.3	Water Transparency	24
4	Monte Carlo Simulations	28
4.1	Signal	28
4.2	Background	31
4.2.1	Neutrino Flux	31
4.2.2	Neutrino Interactions	32
4.3	Detector	35
5	Data Set	37
5.1	First Reduction	37
5.2	Second Reduction	39
5.3	Third Reduction	39

CONTENTS

5.4	Fourth Reduction	41
5.5	Fifth Reduction	41
5.6	Final FC Data Set	45
6	Event Reconstruction	47
6.1	Overview of Two Algorithms	47
6.2	APfit	48
6.2.1	Vertex Fitting	48
6.2.2	Ring Counting	49
6.2.3	Particle Identification	51
6.2.4	Momentum Determination	53
6.2.5	Michel Electron Tagging	55
6.3	fitQun	55
6.3.1	Likelihood Function	55
6.3.2	Vertex Pre-fitter	69
6.3.3	Hit Clustering	69
6.3.4	Single-Ring Fitter	70
6.3.5	Multi-Ring Fitter	74
6.4	Performance in MC Simulation: APfit vs. fitQun	77
6.5	Fiducial Volume	83
6.6	Energy Scale	84
6.6.1	High Energy Stopping Muon Sample	84
6.6.2	Low Energy Stopping Muon Sample	86
6.6.3	Michel Electron Energy Spectrum	88
6.6.4	Neutral Pion Mass	88
6.6.5	Energy Scale Error	90
6.6.6	Uniformity of Energy Scale Error	91
7	Data Analysis	94
7.1	Selection Criteria	94
7.2	Systematic Errors	107
7.3	MC-Data Agreement in the Outside the Signal Region	118
7.4	Result	121
7.5	Lifetime Limit	127
8	Discussion	129
8.1	Comparison with GUT models	129
8.2	Further Improvements for fitQun	130
8.3	Discovery Potential in Future	130
9	Conclusion	138
A	Special Handling for the Blasting in the Mine	140
B	Time Variation of PMT Hit Rate	143
C	Development of FitQun for SK-I to SK-III	146

CONTENTS

D Mass Production of Atmospheric Neutrino MC	149
---	------------

Chapter 1

Introduction

Where do we come from? What are we? Where are we going? – Paul Gauguin. These might be philosophical questions, but we can paraphrase them in a physics point of view; How does our universe begin and end? What are fundamental particles and interactions between them?

As for the first question, it is considered that our universe at birth was a tiny space with an extremely high temperature and has been expanding at an accelerating rate. The end of the universe is not clear, but dark energy and dark matters which are unknown thing may play a crucial role. Such cosmological discussions rely on the general relativity proposed by A. Einstein in 1916. In its 100th anniversary year, the LIGO and Virgo collaborations announced that they observed gravitational waves from a binary black hole merger [2]. By this observation, the last remaining prediction of the general relativity is confirmed.

About the second question, we have a beautiful theory of elementary particles, so-called the standard model (SM). The SM contains three fundamental forces except for gravity; strong, weak and electromagnetic forces. Weak and electromagnetic forces are unified at a high energy. Most of elementary particle phenomena can be explained by the SM very precisely. The last missing piece of the SM prediction was a Higgs boson, but it was recently discovered by the ATLAS [3] and the CMS [4] experiments in 2012.

However, there are still a lot of things which imply the existence of physics beyond the SM; the unification of three forces, neutrino masses, electric charge quantization and so on. Neutrinos are the one of the fundamental particle in the SM which assumes neutrinos are massless. This assumption is completely excluded by the observation of neutrino oscillations at the Super-Kamiokande experiment in 1998 [5]. The theory beyond the SM must exist. The most attractive model is a grand unified theory (GUT) which merges three fundamental forces at very high energy. Most of GUTs predict that a nucleon spontaneously decays into lighter particles, “nucleon decay” as shorthand, while protons are considered as stable in the SM. Since the temperature of the early universe is extremely high, the verification of GUT is one of the important issues to answer the questions above. Moreover, a proton’s fate might be related to the end of

universe. Therefore, we search for proton decay particular in $p \rightarrow e^+\pi^0$ which is the most dominant decay mode in many GUTs.

Since protons live a long time, we need to monitor a large number of protons. Our experimental equipment is the Super-Kamiokande (SK) detector which is the largest volume detector for nucleon decay search. The most sensitive proton decay mode in the SK detector is $p \rightarrow e^+\pi^0$. Figure 1.1 shows a schematic diagram of $p \rightarrow e^+\pi^0$ and its typical Monte Carlo simulation event display in SK. There are four distinct observation periods; SK-I, -II, -III and -IV. The current period is SK-IV which has the most stable operation and the best detector performance. As of today, the amount of data taken in the SK-IV period is almost half of the whole period. We have been searching for many nucleon decay modes not only the $p \rightarrow e^+\pi^0$ mode since the experiment started in 1996. No significant data excess was found. However, the nucleon lifetime predicted by many GUTs is still in the SK search region. It can be said, nucleon decay could happen at anytime.

We have to improve our analysis method, not just waiting to observe nucleon decay. We developed a new event reconstruction algorithm, called fitQun. FitQun has better performance than a conventional algorithm, APfit, which has been used since the experiment started. At present, fitQun works only for the SK-IV data. So, we search for $p \rightarrow e^+\pi^0$ with the data of SK-I to SK-III by APfit and that of SK-IV by fitQun in this thesis.

Based on the huge efforts of the SK collaboration over the past 20 years, this thesis exists. The author highly contributed to the followings related to the contents of this thesis:

- Quality control of a data set for proton decay and atmospheric neutrino analyses as an expert (1 year)
- Validation of fitQun with some collaborators through a proper calibration
- Evaluation of a fitQun's energy scale error
- Generation of a 3000 years atmospheric neutrino Monte Carlo simulation as the background of $p \rightarrow e^+\pi^0$
- First application of fitQun to the proton decay analysis ($p \rightarrow e^+\pi^0$) through detailed checks and a tuning of fitQun
- First proton decay search ($p \rightarrow e^+\pi^0$) including an unexplored region of the SK detector (10% expansion of a conventional fiducial volume)

In Chapter 2, we discuss the physics motivation of this thesis, including a brief history and the importance of proton decay search. Our experimental set up and its calibration are explained in Chapter 3. Chapter 4 describes Monte Carlo simulations for both the signal and background events. The data set for this analysis is prepared through a proper data reduction process described in Chapter 5. Chapter 6 explains the event reconstruction algorithms. The analysis and result are shown in Chapter 7. Chapter 8 discusses about the result and the future prospects. Finally, we conclude this thesis in Chapter 9.

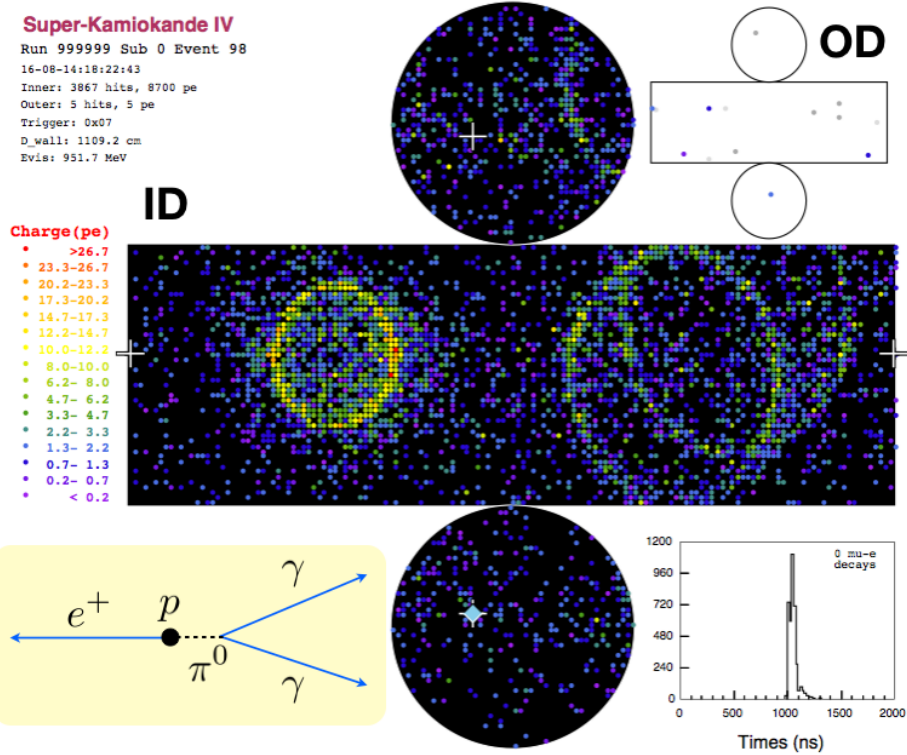


Figure 1.1: Schematic diagram of $p \rightarrow e^+ \pi^0$ (bottom left) and its typical Monte Carlo simulation event display in SK-IV (center). A free proton decayed at around the tank center. It emitted a positron on the left and a neutral pion on the right. As a result of the pion decay, three electromagnetic shower rings are observed. Each dot corresponds to a PMT and the color shows the amount of the observed charge.

Chapter 2

Physics motivation

2.1 Standard Model and its Problems

The Standard Model (SM) is a quantum field theory with the gauge group $SU(3)_C \times SU(2)_L \times U(1)_Y$, three generations of fermions and a scalar Higgs boson. $SU(3)_C$ and $SU(2)_L \times U(1)_Y$ describe the strong and electro-weak forces, respectively, which are carried by the gauge bosons $G_{1\sim 8}$, $W_{1\sim 3}$ and B . The SM fermions are listed in Table 2.1 with their representations of each group and hypercharge $Y = 2(Q - T_3)$, where Q is the electric charge and T_3 is the $SU(2)$ isospin. The Higgs boson makes some fermions and gauge bosons massive through the spontaneous symmetry breaking of $SU(2)_L \times U(1)_Y$.

Most of high energy phenomena can be very precisely explained by the SM. In summer 2012, the Higgs boson as the last missing piece of the SM was discovered by the ATLAS [3] and the CMS [4] experiments. The SM was completed, however, it is obviously not an ultimate theory because there are no gravity, dark matter and neutrino masses. Furthermore, there are many theoretical questions such as the hierarchy problem, triangle anomalies, the number of free

Table 2.1: Fermion fields in the standard model and their representations of non-Abelian groups and hypercharge. Bold numbers indicate the dimension of representations.

	$SU(3)_C$	$SU(2)_L$	$U(1)_Y$
u, d	3	2	$\frac{1}{3}$
u^c	$\bar{3}$	1	$-\frac{4}{3}$
d^c	$\bar{3}$	1	$\frac{2}{3}$
ν_e, e	1	2	-1
e^c	1	1	2

parameters and so on. In particular, the electric charge quantization of fermions highly motivates us to unify quarks and leptons. Since the electric charges are the arbitral coupling constants of $U(1)_Y$, there is no reason that the electric charge of down quarks is the third of that of electrons. But, the magnitude of electric charge of protons is measured as the same of that of electrons with an accuracy of 1×10^{-21} [6]. In addition to that, it can be said that the baryon/lepton number symmetry in the SM is just an accidental symmetry (not a local gauge symmetry), which might be violated in a high energy limit. Also, the three running coupling constants in the SM run across each other in a very high energy region $> 10^{14}$ GeV. These circumstantial evidences imply that there is a larger gauge group which is approximated to the SM group in a low energy limit. Such models are called Grand Unified Theories (GUTs). We discuss several GUTs in the following.

2.2 Grand Unified Theories

There are many GUT models and they predict nucleon decay in general. In this section, we focus on $SU(5)$, SUSY $SU(5)$ and $SO(10)$ models. Comprehensive discussions on GUTs (flipped $SU(5)$, E_6 , etc.) can be found in the document [7].

2.2.1 $SU(5)$ Model

The first grand unified theory was proposed by H. Georgi and S. Glashow in 1974 [8]. The rank of a gauge group represents the number of independent quantum numbers; the rank of $U(1)$ is one and that of $SU(n)$ is $n - 1$. So, a simple gauge group which contains the SM groups as subgroups should have a rank more than three. In addition to that, complex representations are necessary in that group. They found out that $SU(5)$ is the minimal answer.

Each family of fermions and gauge bosons in $SU(5)$ are represented by $\mathbf{10} + \bar{\mathbf{5}}$ and $\mathbf{24}$, respectively, as follows;

$$\bar{\mathbf{5}} : \begin{pmatrix} d_1^c \\ d_2^c \\ d_3^c \\ e \\ -\nu_e \end{pmatrix} \quad \text{and} \quad \mathbf{10} : \begin{pmatrix} 0 & u_3^c & -u_2^c & u_1 & d_1 \\ -u_3^c & 0 & u_1^c & u_2 & d_2 \\ u_2^c & -u_1^c & 0 & u_3 & d_3 \\ -u_1 & -u_2 & -u_3 & 0 & e^c \\ -d_1 & -d_2 & -d_3 & -e^c & 0 \end{pmatrix}, \quad (2.1)$$

$$\mathbf{24} : \begin{pmatrix} G_1^1 - \frac{2B}{\sqrt{30}} & G_2^1 & G_3^1 & \bar{X}_1 & \bar{Y}_1 \\ G_1^2 & G_2^2 - \frac{2B}{\sqrt{30}} & G_3^2 & \bar{X}_2 & \bar{Y}_2 \\ G_1^3 & G_2^3 & G_3^3 - \frac{2B}{\sqrt{30}} & \bar{X}_3 & \bar{Y}_3 \\ X^1 & X^2 & X^3 & \frac{W^3}{\sqrt{2}} + \frac{3B}{\sqrt{30}} & W^+ \\ Y^1 & Y^2 & Y^3 & W^- & -\frac{W^3}{\sqrt{2}} + \frac{3B}{\sqrt{30}} \end{pmatrix}, \quad (2.2)$$

where the suffixes of quarks show the $SU(3)_C$ color, G s correspond to gluons, X and Y are 12 new gauge bosons. Since $\text{Tr}Q = \text{Tr}(T_3 + Y/2) = 0$, this model

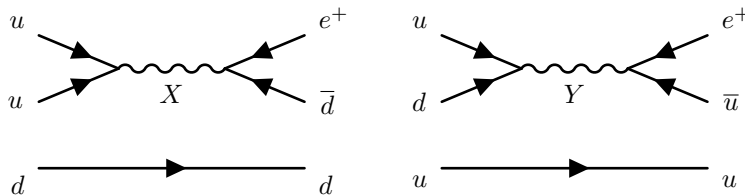


Figure 2.1: Feynman diagrams for $p \rightarrow e^+ \pi^0$ via X and Y bosons.

can explain the electric charge quantization as follow,

$$\sum_{a=1}^5 Q_a = 3Q_{d^c} + Q_e + Q_{\nu_e} = 0 \quad \rightarrow \quad Q_d = -Q_{d^c} = -\frac{1}{3}. \quad (2.3)$$

In the gauge sector, the upper left 3×3 matrix is for $SU(3)_C$ rotations and the lower right 2×2 matrix is for $SU(2)_L$ rotations whereas the other off-diagonal elements (X s and Y s) connect quarks and leptons. Thus, the baryon/lepton number is no longer a conserved quantity, and nucleons spontaneously decay. Because we, made of matters, exist stably, both of X and Y should be massive. Through a spontaneous symmetry breaking of $SU(5) \rightarrow SU(3)_C \times SU(2)_L \times U(1)_Y$ occurred at a GUT energy scale ($> 10^{14}$ GeV), they earn masses.

In the minimal $SU(5)$, the most dominant decay mode is $p \rightarrow e^+ \pi^0$ whose predicted proton lifetime is about $10^{31 \pm 1}$ years [9]. Figure 2.1 shows the Feynman diagrams for $p \rightarrow e^+ \pi^0$. However, this was already excluded by the previous experiments as seen in Section 2.2.4. Furthermore, $SU(5)$ predicts the Weinberg angle (θ_W) as $\sin^2 \theta_W = 3/8$, but this prediction was also excluded by experimental results of about 0.23 [10]. The minimal $SU(5)$ GUT model is completely ruled out.

2.2.2 SUSY $SU(5)$ Model

One attractive idea to save the $SU(5)$ model is to introduce a symmetry between fermions and bosons, so-called “super-symmetry (SUSY).” t t SUSY makes the number of both fermions and bosons double, however, three running coupling constants can completely match at around 2×10^{16} GeV [11–13] as shown in Figure 2.2.

Since we do not observe any of light leptons with spin-zero, SUSY must be broken at a low energy, typically > 1 TeV. In order to observe SUSY particles, direct searches have been conducted by the ATLAS and the CMS experiments, but no new particles were found so far. The GUT energy scale increases by SUSY, and the proton lifetime is predicted to be longer than that of non-SUSY $SU(5)$.

In the minimal SUSY $SU(5)$ model, the most dominant decay mode of protons is $p \rightarrow \bar{\nu} K^+$ since SUSY partners of Higgs (Higgsinos) which are mediators

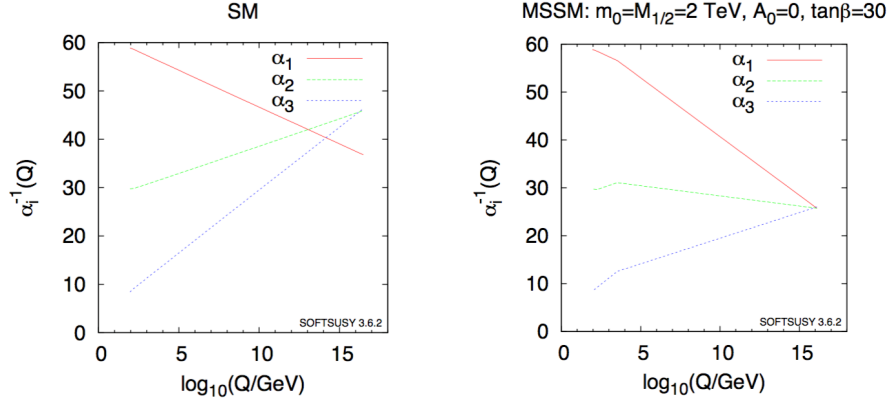


Figure 2.2: Running coupling constants in the SM (left) and the minimal SUSY SM (right) powered by SOFTSUSY [16]. Taken from [7].

prefer to couple with heavier particles [14]. Its predicted upper limit of the partial lifetime of $p \rightarrow \bar{\nu}K^+$ is $< 2.9 \times 10^{30}$ years whereas that of $p \rightarrow e^+\pi^0$ is $> 4.1 \times 10^{33}$ years [14]. Looking at Super-Kamiokande results, it seems that the minimal SUSY $SU(5)$ model is also excluded as well as the minimal $SU(5)$ model [15].

2.2.3 $SO(10)$ Model

The minimal $SU(5)$ model can not explain why neutrinos have mass. The seesaw mechanism can solve this question by introducing right-handed neutrino [17–19]. A right-handed neutrino is naturally implemented in the next larger GUT, $SU(10)$ which has rank five [20, 21]. All fermions including the right-handed neutrino can be embedded in a single $\mathbf{16}$ representation ($= \mathbf{10} + \bar{\mathbf{5}} + \mathbf{1}$).

There are many patterns of $SO(10)$ symmetry breaking as follow.

$$\begin{aligned}
 SO(10) &\rightarrow \begin{cases} SU(5) \times U(1), \\ SU(4) \times SU(2)_L \times SU(2)_R, \\ SU(3) \times SU(2)_L \times SU(2)_R \times U(1), \\ SU(4) \times SU(2)_L \times U(1) \end{cases} \\
 &\rightarrow SU(3)_C \times SU(2)_L \times U(1)_Y
 \end{aligned} \tag{2.4}$$

The second term $SU(4) \times SU(2)_L \times SU(2)_R$ is known as the Pati-Salam model in which $SU(2)_L \times SU(2)_R$ expresses a left-right symmetry (Parity is recovered at very high energy). Since there are more than one symmetry breaking energy scales in $SO(10)$, it is possible to choose them so that three running coupling constants unify.

The most dominant decay mode of $SO(10)$ is $p \rightarrow e^+\pi^0$ as well as the $SU(5)$ model and its lifetime is predicted in a large range $10^{32} - 10^{39}$ years [22, 23].

2.2.4 Proton Decay Search

The baryon number conservation law (Weyl [24] (1929), Stueckelberg [25] (1938), Wigner [26] (1949)) had been tested by various proton decay searches before the minimal $SU(5)$ model was proposed in 1974. The first experimental search for proton decay was conducted by M. Goldhaber [27] in 1954. He searched for fission products of Th^{232} induced by proton decay, and set the limit of $> 10^{20}$ years [27]. This kind of inclusive indirect search was done for several materials by using geochemical and radiochemical methods which are described in [28]; Th^{232} (Flerov *et al* [29]), $\text{Te}^{130} \rightarrow \text{Xe}^{129}$ (Evans and Steinberg [30]), $\text{K}^{39} \rightarrow \text{Ar}^{37}$ (Fireman [31]) and Mica (Bennett [32]).

At the same time, the direct search by using liquid scintillator was in fashion [27, 33–40]. The first one is Reines *et al* [27], they measured charged particles with kinetic energy of above 100 MeV from proton decay by 300 liters of liquid scintillator in the depth of 200 m.w.e.

After 1974, many GUT motivated experiments began to be proposed. The first partial lifetime limit for $p \rightarrow e^+ \pi^0$ is $> 6 \times 10^{29}$ years measured by Learned *et al* using liquid scintillators located in deep underground [40]. Thereafter, four experiments were conducted by using fine grained iron calorimeter which consists of alternative iron layers (NUSEX [41], KGF [42], Soudan [43] and Frejus experiment [44]). Although such calorimeter has excellent energy resolution and particle identification, it is not feasible to scale up the detector volume due to cost. Compared to that technique, it is much easier to construct large volume of water Cherenkov detector discussed in Chapter 3 with lower cost. Thus, the current main stream in proton decay search is to use water Cherenkov technique.

The previous water Cherenkov experiments are Homestake (150 ton in fiducial mass) [45], IMB (3.3 kton in fiducial mass) [46] and KAMIOKANDE (1.0 kton in fiducial mass) [47]. They searched for proton decay in many decay modes, but no evidences were found. As a successor of the KAMIOKANDE experiment, the Super-Kamiokande (SK) experiment has been leading proton decay search with its fiducial mass of 22.5 kton [48, 49]. Unfortunately, we found no evidence and thus set the partial lifetime limit to $p \rightarrow e^+ \pi^0$ [1] and $p \rightarrow \nu K^+$ [50] are,

$$\tau/B(p \rightarrow e^+ \pi^0) > 1.6 \times 10^{34} \text{ years} \quad (2.5)$$

and

$$\tau/B(p \rightarrow \nu K^+) > 5.9 \times 10^{33} \text{ years}, \quad (2.6)$$

which ruled out the minimal $SU(5)$ and minimal SUSY $SUSY(5)$ model, respectively.

The summary plot of previous proton decay searches is shown in Figure 2.3. SK has led this field and given the stringent constraints to GUTs for almost 20 years. This superiority of SK is expected to continue after about 10 years from today before starting a next generation of proton decay search experiment discussed in Chapter 8. Since the sensitivity of SK is within the range of the

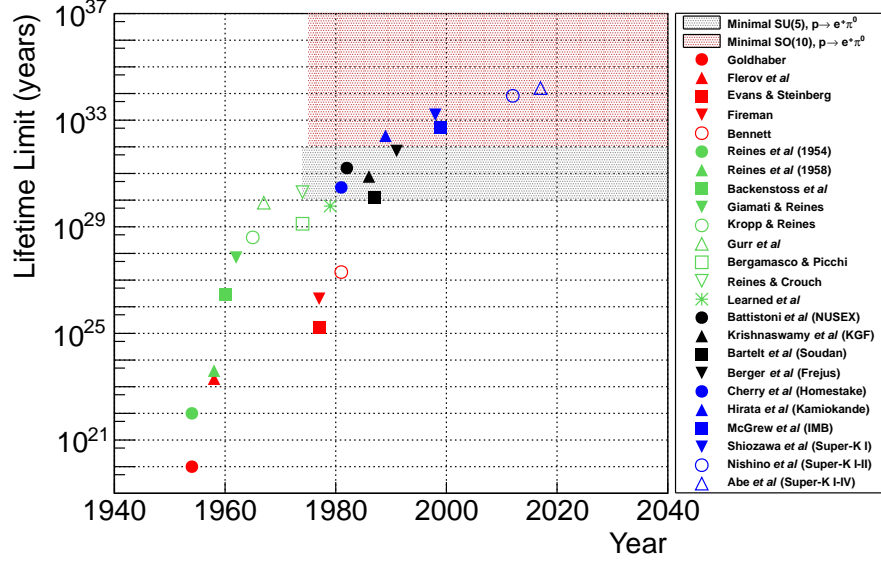


Figure 2.3: Summary of proton lifetime limits by the previous experiments. The black (red) region shows the predicted lifetime range in the minimal $SU(5)$ ($SO(10)$) model. The red, green, black and blue points correspond to the geochemical and radiochemical method, liquid scintillator, fine grained calorimeter and water Cherenkov experiments. The results of Learned *et al* and KGF, Soudan, Frejus, Homestake, KAMIOKANDE, IMB and Super-Kamiokande experiments are for $p \rightarrow e^+ \pi^0$ whereas the others are the other modes or inclusive results.

minimal $SO(10)$ model, there is still a chance to discover proton decay. However, the contamination of background events goes on increasing year after year. In this thesis, we search for $p \rightarrow e^+ \pi^0$ which is the most dominant decay mode in the minimal $SO(10)$ model and the most sensitive decay mode in SK. We expand the fiducial volume and reduce the background rate by using a new event reconstruction algorithm described in Chapter 6. This analysis is the cleanest search for $p \rightarrow e^+ \pi^0$ with the highest statistic of data in the world.

Chapter 3

Super-Kamiokande Experiment

3.1 Overview

Super-Kamiokande (SK) is a large water Cherenkov detector proposed in 1987, whose main physics target is to search for proton decay. The SK detector mainly consists of a cylindrical stainless steel tank (41.4 m in height and 39.3 m in diameter), 50 kton ultra-pure light water (H_2O) and the photomultiplier tubes (PMTs), which is shown in Figure 3.1 [51]. In order to avoid cosmic ray muon background, the detector is located in the Kamioka mine 1,000 m underground of Mt. Ikenoyama, in Kamioka town, Gifu Prefecture, Japan. At that point (2,700 m.w.e.), the cosmic ray muon flux is $6 \times 10^{-8} \text{ cm}^{-2}\text{s}^{-1}\text{sr}^{-1}$ which is five orders of magnitude smaller than that on the surface of the earth, and its rate observed in SK is about 2 kHz.

There are two concentric cylinders inside the tank; the inner detector (ID) and the outer detector (OD). The ID is a main detector which contains 32 kton of water with 36.2 m in height and 33.8 m in diameter, whereas the OD is a cosmic ray muon veto detector which covers the region surrounding the ID with the thickness of about 2 m. Both detectors are optically separated by opaque materials. The OD is also used to prevent backgrounds from the surrounding rock such as neutrons and gamma rays.

On the ID surface, 20-inch PMTs are uniformly mounted facing inward viewing the ID volume while 8-inch PMTs are uniformly mounted on the OD surface facing outward viewing the OD, as shown in Figure 3.2. In order to prevent the geomagnetic field effect to PMTs, 26 sets of Helmholtz coils are equipped on the wall of the tank and reduce the magnetic field from 450 mG to 50 mG.

The observation started on April 1996 with 11,146 ID PMTs and 1,885 OD PMTs and stopped on July 2001 for a maintenance work to replace bad PMTs. This phase is called SK-I. While refilling the tank with the water after the replacement work, an accident happened on November 12th, 2001 at 11:01

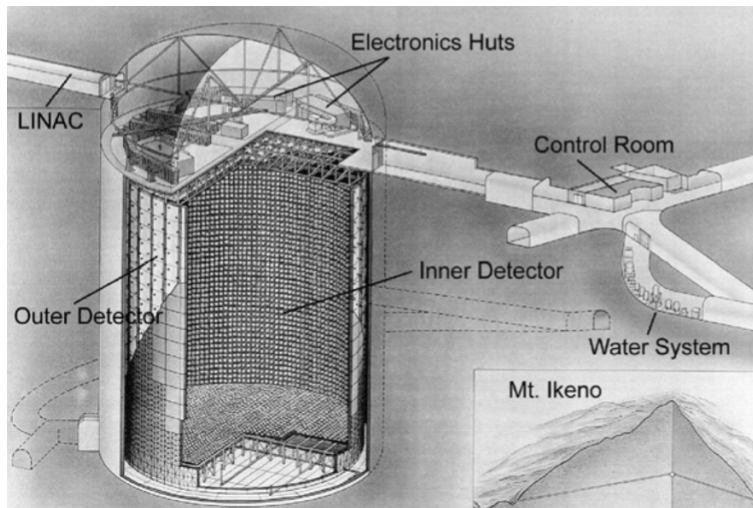


Figure 3.1: Schematic view of the Super-Kamiokande detector. Taken from [51].

JST. One of the ID PMTs at the bottom collapsed, a vacuum space suddenly emerged and was immediately crushed, and then shock wave was generated and destroyed PMTs. As a result of chain reaction of shock wave, about 60% of all PMTs were broken. In order to avoid same incident, fiber reinforced plastics (FRPs) and acrylic cases come into use to protect ID PMTs hereafter. The next phase of SK, SK-II, started from October 2002 after redistributing the surviving ID PMTs and installing new OD PMTs and stopped on October 2005. After reconstructing the SK, the third phase (SK-III) started from June 2006 with 11,129 ID PMTs. On September 2008, the read-out electronics and the data acquisition system were upgraded. The SK-IV phase has begun at that time and continues until this day. The photo-coverage of SK is 40%, except SK-II (19%). Table 3.1 shows the summary of the SK phases.

3.2 Principle of the Detector

Super-Kamiokande observes charged particles by detecting the Cherenkov radiation using PMTs. In a medium with a refractive index n , a charged particle emits electromagnetic shock wave when the velocity of the particle ($v = \beta c$) exceeds the phase velocity c/n of light, as shown in Figure 3.3. This phenomenon is known as the Cherenkov radiation. Along with the particle track, the Cherenkov light is emitted as a cone with its opening angle θ_C which satisfies,

$$\cos \theta_C = \frac{1}{n\beta}. \quad (3.1)$$

Since n is about 1.34 in water, θ_C is 42° for the particle with $\beta \simeq 1$.

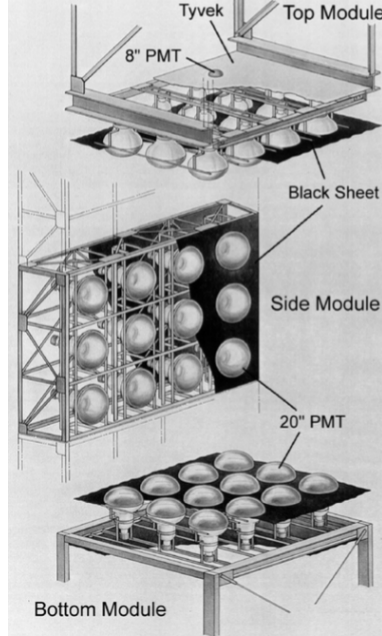


Figure 3.2: Supporting frames of PMTs. Taken from [51].

Table 3.1: Summary of the four Super-Kamiokande observation phases. The live time of SK-IV corresponds to the data collecting from Sep. 2008 to Aug. 2016.

		SK-I	SK-II	SK-III	SK-IV
Observation	Start	Apr. 1996	Oct. 2002	Jun. 2006	Sep. 2008
	End	Jul. 2001	Oct. 2005	Aug. 2008	(running)
Live time (days)		1489.2	798.6	518.1	2650.4
Number of PMTs	ID	11,146	5,182	11,129	11,129
	OD	1,885	1,885	1,885	1,885
Photo Coverage		40%	19%	40%	40%
FRP&Acrylic Case		No	Yes	Yes	Yes
Electronics	ID	ATM	ATM	ATM	QBEE
	OD	OD QTC	OD QTC	OD QTC	QBEE
Trigger		Hardware	Hardware	Hardware	Software

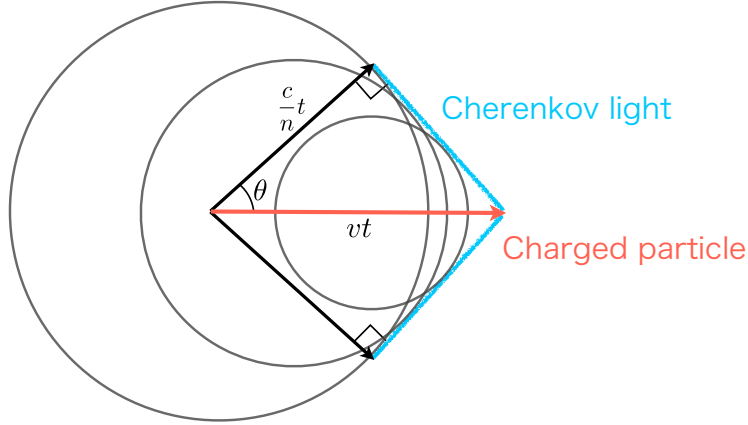


Figure 3.3: Schematic view of the Cherenkov radiation.

The momentum threshold for the Cherenkov radiation is derived from the condition of $\beta > 1/n$. For example, the Cherenkov threshold for electrons in water is 0.57 MeV/c. Table 3.2 summarizes the Cherenkov threshold for various charged particles in water.

The number of emitted photons per wavelength λ per unit travel distance x of a charged particle is given as,

$$\frac{d^2 N}{dx d\lambda} = \frac{2\pi\alpha}{\lambda^2} \left(1 - \frac{1}{n^2\beta^2} \right), \quad (3.2)$$

where α is the fine structure constant. For the wavelength between 300 nm and 600 nm, 340 photons are emitted per unit cm by the particle with $\beta \simeq 1$ in water ($n = 1.34$).

Figure 3.4 shows the Cherenkov light patterns for two different types of the particle observed in SK. The difference between those two is the sharpness of the Cherenkov ring edge. Electrons or high energy gamma-rays create fuzzy rings (“shower”) as shown in the top display since they produce electromagnetic shower and are deflected by the multiple scattering, whereas muons or charged pions create sharper rings (“non-shower”) as shown in the bottom display since they do not produce electromagnetic shower. Not only the particle type, the kinematics of particle such as the vertex, direction and momentum are determined by using the Cherenkov light arrival time and its amount received at each PMT as described in Chapter 6.

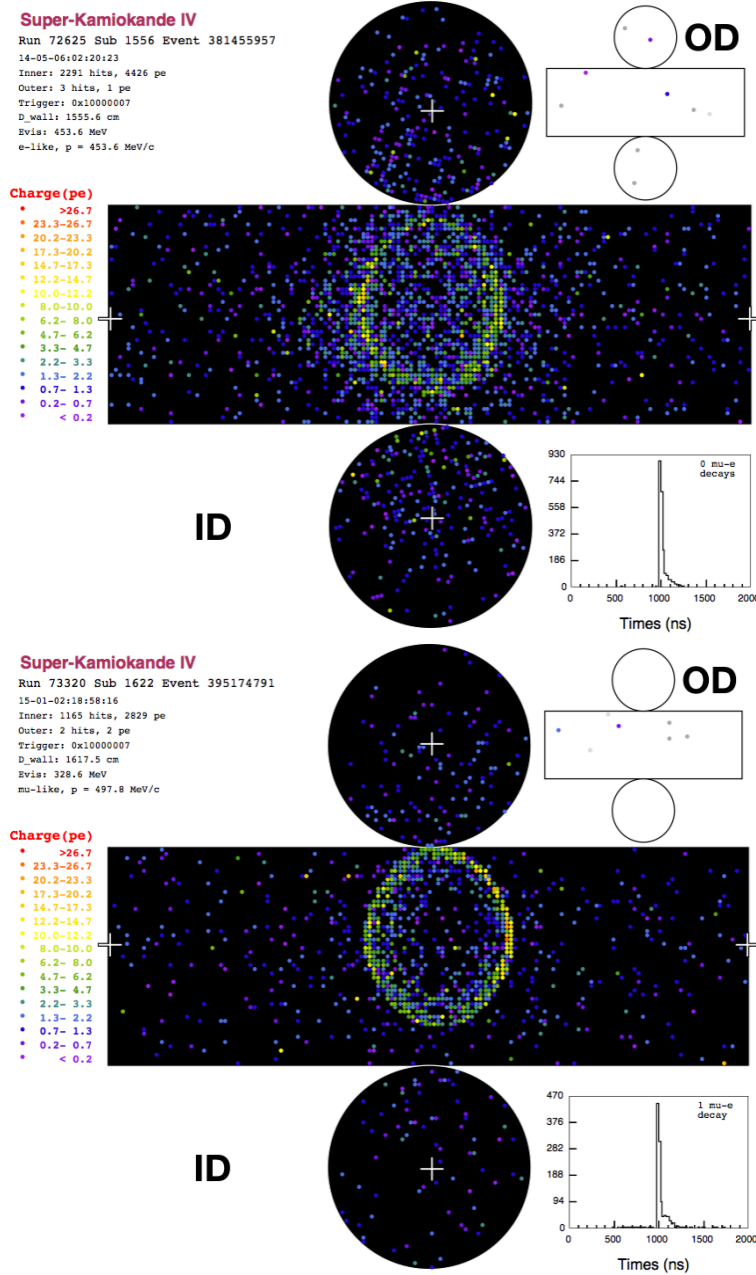


Figure 3.4: Shower (top) and non-shower (bottom) events in the fully-contained data set discussed in Chap 5. Each dot shows a PMT which detects photons, and its color indicates the amount of the charge. According to a reconstruction algorithm (fitQun discussed in Chap 6), the momentum of the particle on the top is 468 MeV/c assuming a single electron ring and that on the bottom is 506 MeV/c assuming a single muon ring.

Table 3.2: Momentum thresholds of the Cherenkov radiation in water for various charged particles assuming $n = 1.34$.

	e	μ	π^+	p
Momentum (MeV/c)	0.57	118	156	1052

3.3 Water and Air

Since Cherenkov light travels in a large distance before reaching the PMTs, a high transparency of the water is necessary. As for the water in SK, spring water in the mine is used. The water is continuously purified and circulated at a rate of about 30 tons/hour by a complex system [51]. The water purification system mainly consists of several filters, a UV sterilizer and two degasifiers in order to remove particles larger than $0.2 \mu\text{m}$, bacteria and radon dissolved in water, respectively. The water temperature is controlled at around $13 \text{ }^\circ\text{C}$ by heat exchangers in order to reduce PMT dark noise and suppress bacteria growth.

In the mine, the air is radon-rich due to the leaking from the rock and can be dissolved in the water since there is a gap between the top of the SK tank and the water surface. Radiation from radon decay becomes the low energy background. In order to reduce such background, the rock of the experimental hall was coated with a polyurethane material, and radon-free air is continuously supplied from outside the mine into the experimental area.

3.4 Photosensors

For the Cherenkov light detection in the ID, the 20-inch PMTs manufactured by Hamamatsu Photonics K.K. (R3600) are used [51]. Figure 3.5 shows a picture of the 20-inch PMT. The bialkali (Sb-K-Cs) photocathode has a quantum efficiency of 22% at a peak where wavelength is 360 nm, as shown in Figure 3.6. The dynode structure is a 11-stage Venetian blind type. The operation of the ID PMTs is conducted applying high voltage ranging in 1700-2000V between the photocathode and the last dynode. The collection efficiency of the first dynode, gain, transit time spread and dark noise rate are over 70%, 10^7 , 2.2 ns (1σ) for a single photoelectron and 3 kHz at 0.25 photoelectrons threshold, respectively. Although the acrylic covers are attached to the ID PMTs used in SK-II to SK-IV, the effect on the photon detection is small because the transparency of the cover for a normal incident photon in water is over 96% at 350 nm.

The Hamamatsu 8-inch PMTs (R1408) are used for the OD [52]. In order to increase the photon collection efficiency, a 1.3 cm thickness 60 cm square wavelength-shifting plate (ultra-violet light \rightarrow blue-green light) is equipped to each OD PMT as shown in Figure 3.7. Due to the reemission process of the plate, the timing resolution of the OD PMT gets worse from 13 ns to 15 ns

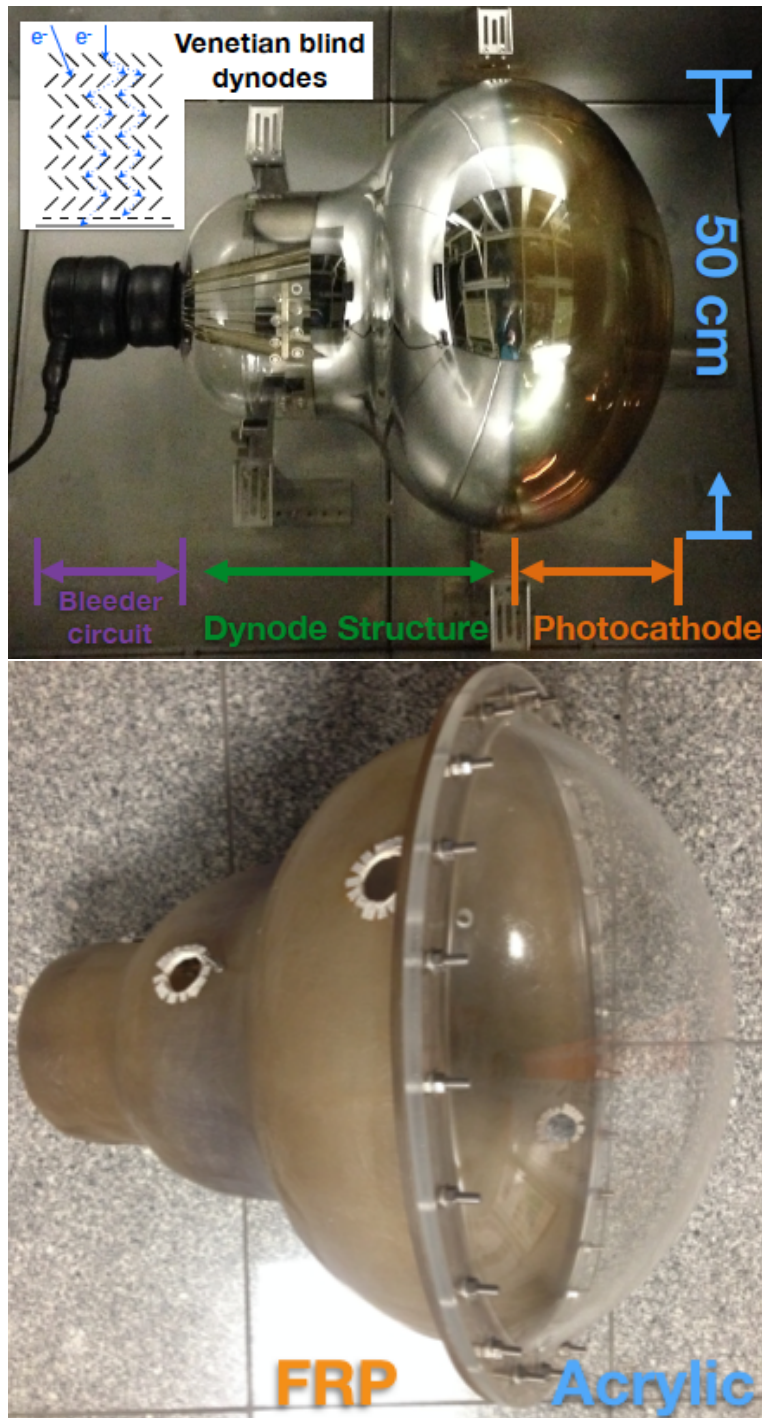


Figure 3.5: Photos of the 20-inch PMT (top) and the FRP and acrylic case (bottom).

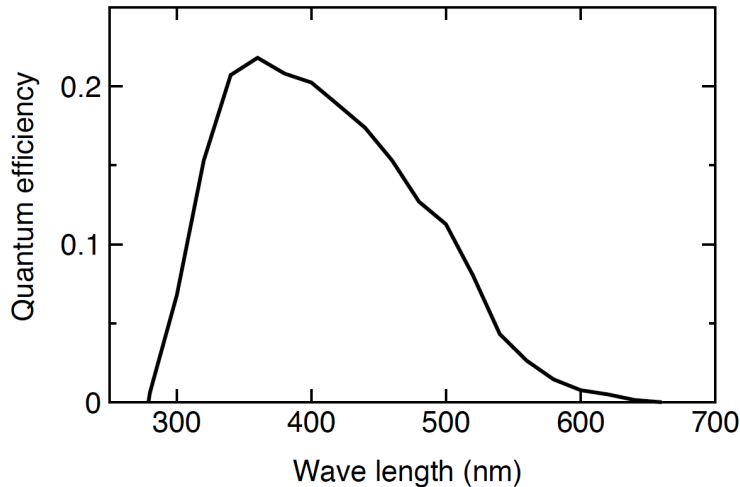


Figure 3.6: Quantum efficiency as a function of wavelength for the 20-inch PMT. Taken from [51].

in FWHM. However, the collection efficiency of the OD PMT is increased by 60%. Furthermore, the reflective material (Tyvek) sheets which have a 90% reflectivity at 400 nm are put on the tank wall and the spaces between the OD PMTs in order to enhance the photon collection efficiency. From SK-III, the Tyvek sheets are also used to separate the barrel and the top and bottom region in the OD for better rejection of “corner-clipping” cosmic-ray muon events.

3.5 Data Acquisition

A PMT signal is fed into front-end electronics via a 70 m RG58 coaxial cable, and it is considered as “hit” when the pulse height exceeds a 0.25 photoelectrons level. An event trigger is issued if the number of the hit PMTs surpasses a trigger threshold. The event consists of the time and charge of the hit PMTs within a given time window around the trigger timing. There are several triggers depending on the visible energy; the low energy (LE), high energy (HE), outer detector (OD) trigger and so on. In this analysis, we use the HE triggered events. Since the data acquisition (DAQ) system which was used in SK-I to SK-III was upgraded for SK-IV, the following sentences discuss the two different DAQ systems, separately.

3.5.1 System for SK-I to SK-III

The front-end electronics of the ID PMTs for SK-I to SK-III is the analog timing module (ATM) [53]. One ATM has 12 channels of the charge-to-analog

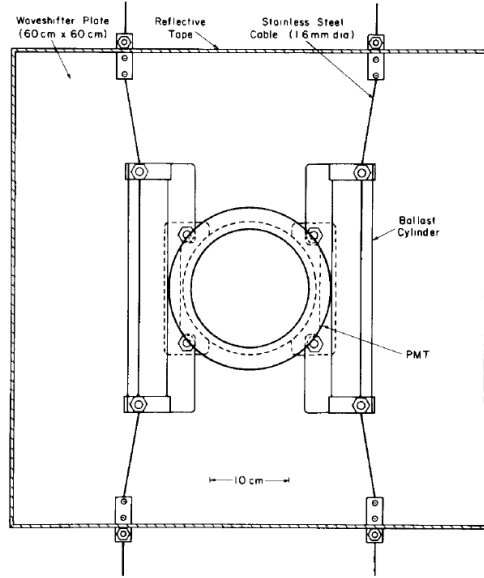


Figure 3.7: Schematic drawing of the OD PMT with the wavelength-shifting plate. Taken from [52].

converters (QACs) and time-to-analog converters (TACs), and 960 ATMs were used for the ID PMTs in total.

For each PMT, a 200 ns rectangular pulse with a 15 mV pulse height is generated when the signal is a hit. The ATM outputs the analog sum of all the rectangular pulse (HITSUM). Then, the event trigger is issued if the sum of HITSUMs from all ATMs exceeds a trigger threshold. Once the event trigger happened, each ATM starts to digitize and record the time whose the hit PMT signal surpasses the threshold and the charge integrated in a 400 ns time window around the PMT trigger timing. In order to avoid missing successive events such as Michel electrons, two switching pairs of both the QAC and TAC are prepared for each channel because the process time for one channel is $5.5 \mu\text{s}$. The time window length of events is $1.3 \mu\text{s}$ around the event trigger $[-400 \text{ ns}, +900 \text{ ns}]$. The signal arrived from 400 ns to 900 ns after the hit is neglected due to a cable reflection pulse caused by a impedance mismatch between an ATM and a PMT.

Similar to the ATM system, signals from OD PMTs are processed by charge-to-time converter modules. When an event trigger happened, the time and charge information are converted to digital by multi-hit time-to-digital converter modules (LeCroy 1877).

There are three types of the event trigger in this system; the super low energy (SLE), LE, HE and OD triggers. Table 3.3 shows the trigger thresholds of SLE, LE and HE for each SK period. The SLE threshold corresponds to 4.6 MeV

Table 3.3: Summary of the hardware triggers used in SK-I to SK-III.

	SK-I	SK-II	SK-III
SLE	186 mV	110 mV	186 mV
LE	320 mV	152 mV	302 mV
HE	340 mV	180 mV	320 mV

electrons. The OD threshold corresponds to 19 hits.

3.5.2 System for SK-IV

Since the ATM has an electronics dead time and a cable reflection issue, a new electronics QBEE [54] was developed and installed for both the ID and OD PMTs. One QBEE has 24 channels, and each channel consists of a custom charge-to-time converter (QTC) and a multi-hit time-to-digital converter (TDC). The timing and charge resolutions of the QTC are 0.3 ns for 2 pC and about 0.2 pC for below 50 pC, respectively. The charge dynamic range of the QTC is 0.2 - 2500 pC, and the charge non-linearity is better than 1% for the overall range.

The QTC records all the hits and immediately integrates the charge from the signals in a 400 ns time window for each hit, and TDC converts the QTC output into the digitized time and charge. The digitized time and charge are recorded when a software trigger is happened. The software trigger is issued when the number of hit PMTs in a 200 ns sliding time window (N_{200}) exceeds a threshold. In this system, the SLE, LE and HE triggers are defined as well as the previous system and these event time windows become larger. In addition to these triggers, special high energy (SHE) and “after trigger (AFT)” triggers were introduced for a neutron tagging algorithm which is used in this analysis. The AFT trigger is issued only for an event triggered by a SHE trigger without an OD trigger and save an additional 500 μ s of data. The software triggers employed in this system are summarized in Table 3.4.

3.6 Detector Calibration

It is necessary for any physics analysis to keep the charge and time response of each PMT are the same for the same intensity and timing of the incident light. Thus, the detector calibration is important. Moreover, calibration results discussed below are used as inputs to the detector simulation and the event reconstruction algorithms.

In this section, we focus on measurements in the ID. The PMT gain calibration is discussed at first since the hit timing depends on the amount of the hit charge. The relative timing calibration and the water transparency mea-

Table 3.4: Summary of the software triggers used in SK-IV.

Trigger Type	N_{200} Threshold	Time Window (μs)
SLE	34 \rightarrow 31	-0.5 \sim +1.0
LE	47	-5 \sim +35
HE	50	-5 \sim +35
SHE	70 \rightarrow 58	-5 \sim +35
AFT	SHE without OD	+35 \sim +535
OD	22	-5 \sim +35

surement and its time variation are then discussed. Details of the calibration methods and other calibration items (e.g. relative QE correction, PMT&black sheet reflection, OD calibration) can be found in [51, 55].

3.6.1 PMT Gain

The first step of the PMT gain calibration is to set the high-voltage (HV) for each PMT so that the output charge of each PMT is the same for the same light intensity. As for the calibration source, a xenon lamp is used. Its flash light is passed through an ultra-violet filter and injected into a scintillator ball which is installed at the tank center via an optical fiber, and then isotropic diffused light is emitted. Since the SK detector is cylindrical, the arrived light intensity to each PMT depends on the PMT location. In order to compensate this geometrical effect, 420 “standard PMTs” whose HVs were adjusted to output the same charge for the same light intensity were mounted in the tank. The HVs of other PMTs in the tank are adjusted in order to match the output charge to that of the nearest standard PMT. The reproducibility of the observed charge for all ID PMTs with respect to their reference values is 1.3%.

The next step is to determine the relative gain difference among PMTs. The calibration source for this relative gain calibration is a nitrogen laser (USHO KEC-100, a pulse width of 0.4 ns in FWHM at a wavelength of 337 nm). The output light is monitored by a faster response 2-inch PMT (Hamamatsu H2431-50, rise time: 0.7 ns). The wavelength of this light is shifted to 398 nm with a pulse width of 0.2 ns by a dye, and the light is passed through neutral filters and injected into a diffuser ball placed in near the tank center via an optical fiber. This shifted wavelength corresponds to almost maximum point of the effective hit taking into account of the Cherenkov spectrum, light absorption and QE spectrum. By using this laser system, two measurements are conducted. The first one uses high-intensity flashes (I_s) for every PMT and records the average observed charge $Q_{\text{ops}}(i)$ for each PMT i which is given as;

$$Q_{\text{obs}}(i) \propto I_s \times a(i) \times \epsilon_{\text{QE}}(i) \times G(i), \quad (3.3)$$

where $a(i)$, $\epsilon_{\text{QE}}(i)$ and $G(i)$ are the acceptance, QE and gain of the i -th PMT.

The second one uses low-intensity flashes (I_w) which make a single photoelectron (p.e.) hit for a few PMTs, and counts the number of hits $N_{\text{obs}}(i)$ for each PMT which is given as;

$$N_{\text{obs}}(i) \propto I_w \times a(i) \times \epsilon_{\text{QE}}(i). \quad (3.4)$$

Then, the gain of each PMT is obtained by taking the ratio of the above two equations namely,

$$G(i) \propto \frac{Q_{\text{obs}}(i)}{N_{\text{obs}}(i)}. \quad (3.5)$$

The relative gain for each PMT is calculated by normalizing $G(i)$ to the average gain over all PMTs, and is used as a PMT-by-PMT correction factor in conversion from the output charge to the number of p.e.s. The RMS of the relative gain distribution is 5.9%.

Finally, the absolute gain for all PMTs is determined. The calibration source is a nickel-californium ball located at the tank center. From this ball, 6.1-9.0 MeV low energy gamma-rays are uniformly emitted by capturing neutrons from the decay of ^{252}Cf by a nickel nucleus. After applying the relative gain factor to each PMT, the single p.e. charge distribution for all PMTs is obtained as shown in Figure 3.8. The averaged single p.e. charge value is determined from the single p.e. distribution after subtracting a similar distribution taken in an off-timing region of the calibration. PMT gain conversion factors are determined as 2.055, 2.297, 2.243 and 2.658 pC per single p.e. for SK-I, II, III and IV, respectively. This single p.e. distribution is used in the detector simulation.

The time variation of the PMT gain is measured by using the cosmic-ray muons going through the detector, so-called ‘‘through-going’’ muons. Since muons deposit almost constant energy of about 2 MeV/cm independent of their energy, the muon track can be regarded as a constant light source. While assuming the observed light is the direct light, the observed charge of the i -th PMT is given as follows,

$$Q(i) = Q_{0,i} \frac{f(\theta)}{l_i} \exp\left(-\frac{l_i}{L'}\right), \quad (3.6)$$

where $Q_{0,i}$ is a constant value, $f(\theta)$ is the PMT acceptance as a function of the light incident angle θ to the PMT, l_i is the photon travel length and L' is the measured attenuation length. Here, the vertical downward muons are used and their tracks are reconstructed by connecting the entering and exiting points on the ID wall. From this equation, the effective observed charge ($\ln(Q(i)l_i/f(\theta))$) is calculated as a function of l . The intercept of that function represents the PMT gain. Figure 3.9 shows the time variation of the averaged PMT gain for each SK. The time dependence of the averaged PMT gain is about 2% per year, however, the reason of the increase is unknown. In the analysis in SK-I to SK-III, we take into account of the PMT gain correction for these variations in the event reconstruction step.

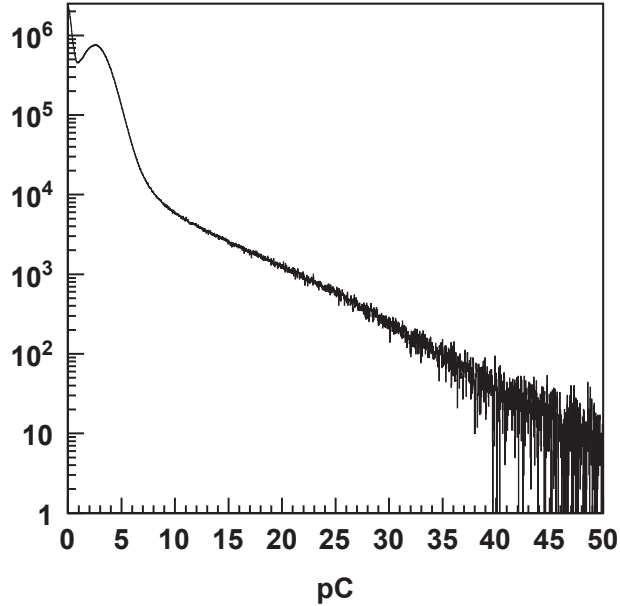


Figure 3.8: Single photoelectron distribution for all PMTs measured by the calibration using the nickel-californium ball. Taken from [55].

For SK-IV, another method to evaluate the PMT gain time variation is available. By taking the early off timing hit distribution for each PMT in the through-going muon sample, one can estimate the PMT absolute gain by looking at the single photoelectron peak. Recently, it revealed that the PMT gain time variation depends on their production year as shown in Figure 3.10. In the analysis in SK-IV, the observed charge of each PMT is corrected by using these PMT gain variations (five production year sets are used).

3.6.2 PMT Timing

The PMT hit timing of each PMT varies due to the variation of the cable length, electronics processing time and timing response dependence of the charge which is known as a time-walk effect. In order to correct the hit timing variation, a two-dimensional time versus charge (TQ) plot is taken for each PMT by using the nitrogen laser system described above. Time-of-flight (TOF) is subtracted from the travel time between the diffuser ball to the respective PMT and then the hits within a ± 50 ns time window of the monitor PMT hit timing are chosen. Figure 3.11 shows a TQ plot. For each charge bin, the TOF subtracted timing distribution is fitted by an asymmetric Gaussian which is used in the detector simulation as shown in Figure 3.12 (in the simulation for SK-I to SK-III, a symmetric Gaussian is used instead). A polynomial function as a function

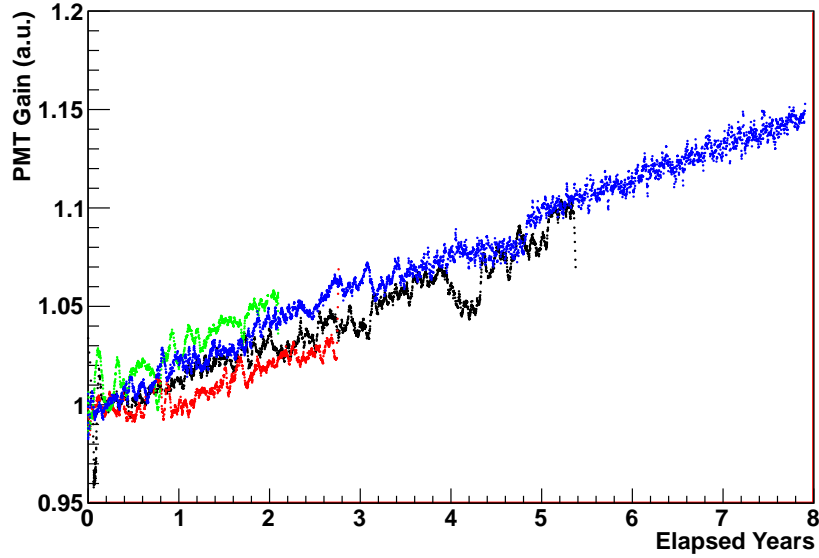


Figure 3.9: Time variation of the averaged PMT gain measured by using the PMTs in the bottom of the tank. The horizontal axis is the elapsed years from the beginning of each SK. The colors show the detector periods; black, red, green and blue are for SK-I, -II, -III and -IV, respectively.

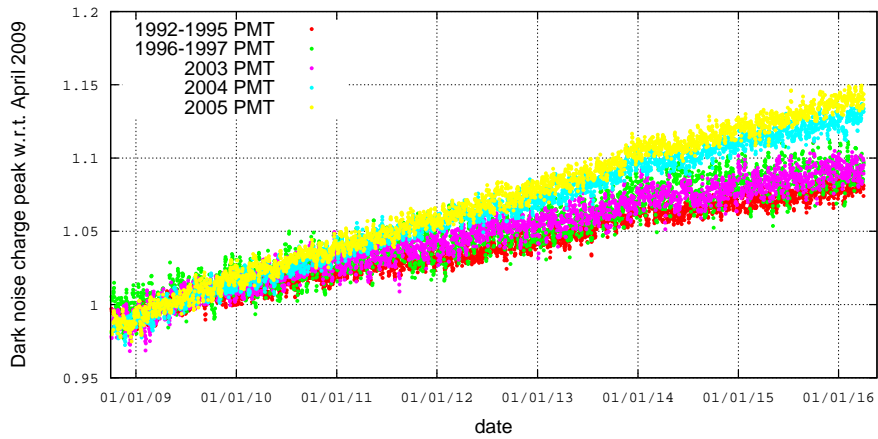


Figure 3.10: PMT production year dependence of the PMT gain time variation in SK-IV. Five different production year groups are displayed.

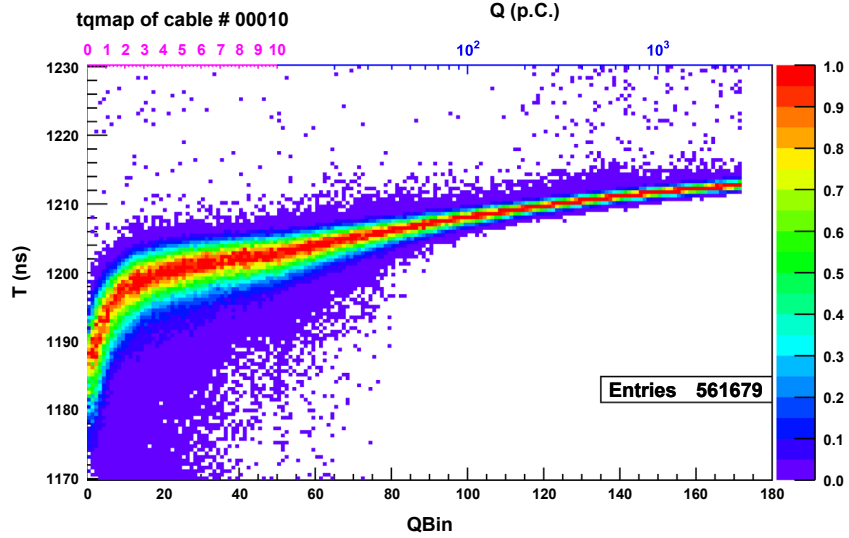


Figure 3.11: Example of the TQ plot. The vertical and horizontal axes represent to the TOF subtracted hit timing and the hit charge, respectively. Taken from [55].

of charge is then obtained by fitting those fitted peak timings and standard deviations, so-called “TQ map.” The TQ map of each PMT is used to correct the hit timing.

3.6.3 Water Transparency

The light absorption and scattering in the water are measured by comparing calibration data results with the detector simulation. Detailed discussion can be seen in the document [51, 55]. As for the data, a nitrogen laser light is injected into the tank via an optical fiber and the hit timing distribution of each PMT are recorded for each five different wavelength of the laser; 337, 375, 405, 445 and 473 nm. When the light of wavelength λ travels a distance l , its intensity is simulated to decrease as $\exp(-l/L(\lambda))$ in the detector simulation. Here, $L(\lambda)$ is the attenuation length in the water which is defined as;

$$L(\lambda) = (\alpha_{\text{sys}}(\lambda) + \alpha_{\text{asy}}(\lambda) + \alpha_{\text{abs}}(\lambda))^{-1}, \quad (3.7)$$

where $\alpha_{\text{sys}}(\lambda)$, $\alpha_{\text{asy}}(\lambda)$ and $\alpha_{\text{abs}}(\lambda)$ are empirical coefficients of the light “symmetric” scattering, “asymmetric” scattering and absorption, respectively. Rayleigh scattering and the symmetric component of Mie scattering are considered as the symmetric scattering, and the asymmetric component of Mie scattering is for the asymmetric scattering. These coefficients are given as the following empirical functions, and their nine parameters P_{0-8} are then obtained by fitting to

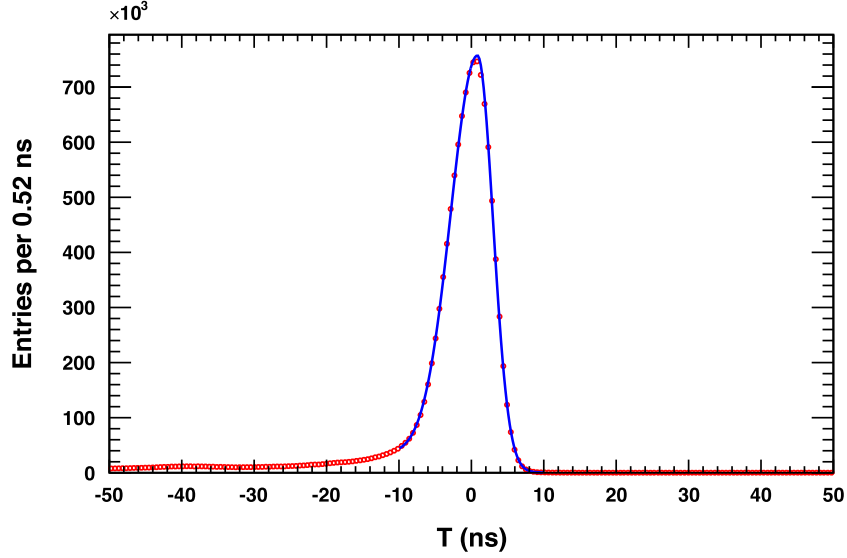


Figure 3.12: Timing distribution of the charge bin 14 (single photoelectron level) for all ID PMTs. The red points show the data and the blue line shows the fitted asymmetric Gaussian function. Taken from [55].

the data;

$$\alpha_{\text{abs}}(\lambda) = \frac{P_0 P_1}{\lambda^4} + C(\lambda), \quad (3.8)$$

$$\alpha_{\text{sym}}(\lambda) = \frac{P_4}{\lambda^4} \left(1.0 + \frac{P_5}{\lambda^2} \right), \quad (3.9)$$

$$\alpha_{\text{asy}}(\lambda) = P_6 \left(1.0 + \frac{P_7}{\lambda^4} (\lambda - P_8)^2 \right), \quad (3.10)$$

where $C(\lambda)$ is the factor derived by the measurement result for $\lambda \geq 464$ nm [56], whereas the following equation is employed for $\lambda \leq 464$ nm,

$$C(\lambda) = P_0 P_2 \left(\frac{\lambda}{500} \right)^{P_3}. \quad (3.11)$$

Figure 3.13 shows the fitted coefficients which are used in the detector simulation.

The time variation of the water transparency is measured by using the through-going muon sample. From Equation 3.6, the water attenuation length L can be evaluated. Figure 3.14 shows the time variation of the measured water

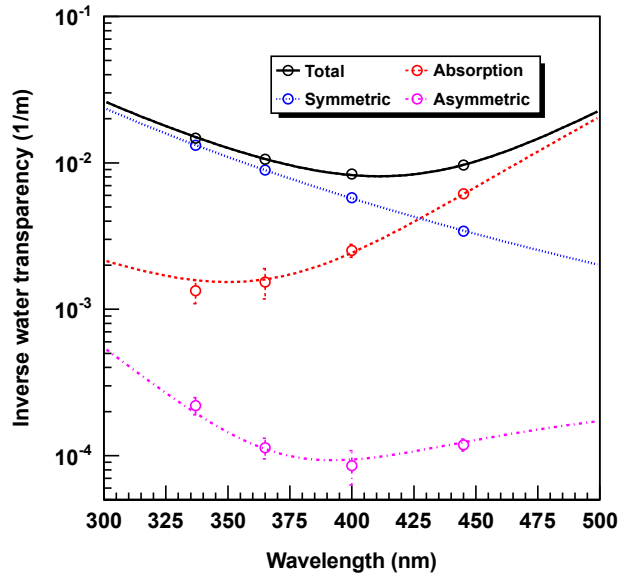


Figure 3.13: Fitted coefficients of the water transparency as a function of the wavelength of the nitrogen laser. The dotted lines are the fitted functions and the solid line is the sum of them. The points are the data measured in April 2009. Taken from [55].

attenuation length in the detector, which is used in the event reconstruction algorithm for the water attenuation correction. Thanks to the sophisticated water control system and closing the tank since the beginning of SK-III, the variation of the water quality in SK-IV is the smallest.

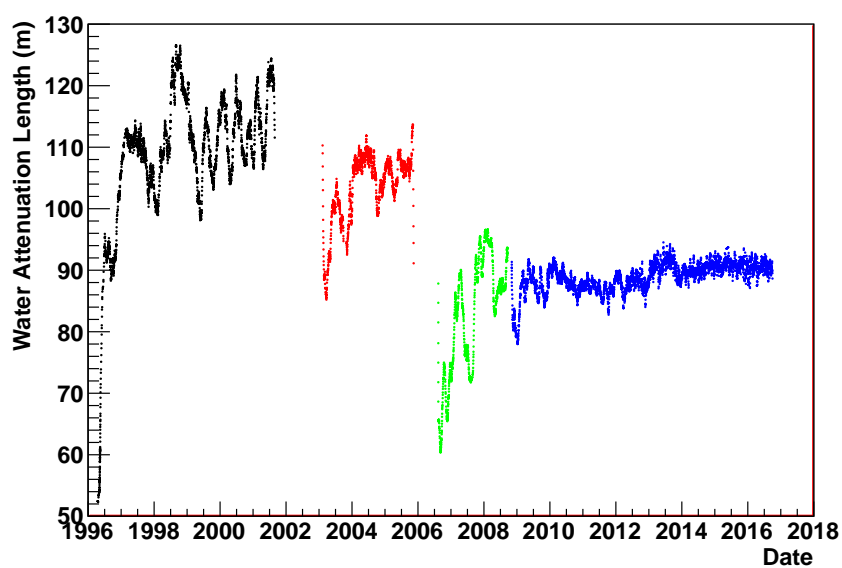


Figure 3.14: Time variation of the water attenuation length from the beginning of SK to Aug. 31st, 2016. The colors show the detector periods; black, red, green and blue are for SK-I, -II, -III and -IV, respectively. Since the detector conditions such as the water circulation, OD segmentation Tyvek sheet, electronics and so on have been changed, it is hard to compare the absolute water attenuation length between each SK period.

Chapter 4

Monte Carlo Simulations

In this chapter, we describe how the signal and background events for $p \rightarrow e^+ \pi^0$ are simulated in this analysis, including the detector behavior. We employ a Monte Carlo (MC) method. As for the background, the atmospheric neutrinos are only considered since other noise events are negligible and can be highly rejected by the data reduction described in Chapter 5.

4.1 Signal

In this analysis, we assume that proton decay equally happened in each proton of H_2O which contains two and eight protons in hydrogen and oxygen nuclei, respectively. Protons in hydrogen which are called “free protons” are stationary and do not interact with other nucleons. Free protons decay into a positron and a neutral pion back-to-back with a monochromatic momentum of 459.43 MeV/c. Then, neutral pions immediately decay into two gammas (the branching ratio of this mode is 98.8% and the rest is for Dalitz decay). On the other hand, protons in oxygen which are called “bound protons” suffer from several effects as described below.

For the decay of bound protons, we first consider the Fermi motion and the nuclear binding energy in ^{16}O . We simulate the nucleon momentum in ^{16}O based on an electron- ^{12}C scattering experiment [57]. Figure 4.1 (left) shows the simulated proton momentum distributions for both the s -state and p -state of ^{16}O . The binding energy is simulated as a Gaussian distribution, and this effect is considered by subtracting the binding energy from the proton mass in the rest. The mean and σ of the binding energy distributions are (39.0 MeV/c, 10.2 MeV/c) for the s -state and (15.5 MeV/c, 3.82 MeV/c) for the p -state. The simulated proton invariant mass in ^{16}O is shown in Figure 4.1 (right).

In addition to the Fermi motion, we consider an effect from a spectator nucleon in ^{16}O . When a proton is going to decay and its wave function is overlapping the other one, this proton decay becomes a two-body system decay and the momentum of the decaying proton is changed. This decay is called the

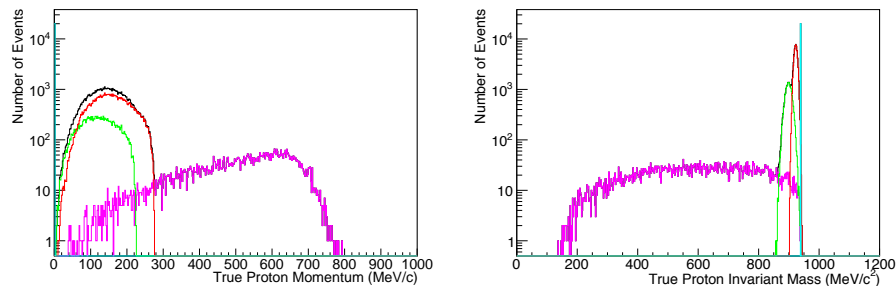


Figure 4.1: Simulated proton momentum (left) and invariant mass (right) distributions. The cyan, black, green, red and purple histograms correspond to free, bound, s -state, p -state and correlated decay protons, respectively.

correlated decay. According to T. Yamazaki and Y. Akaishi [58], the predicted probability of the correlated decay is about 10%. Figure 4.1 shows the proton momentum and invariant mass distributions in ^{16}O .

While a positron emerged in ^{16}O can immediately escape without any interaction, a neutral pion often interacts hadronically with nucleons via inelastic scattering, absorption or charge exchange which converts a neutral pion to a charged pion. These pion final state interactions (π -FSI) are simulated in NEUT [59], and the cross sections for each interaction are calculated from a cascade model [60] which was tuned by various π -(p, n) and π - N scattering data [61].

Figure 4.2 shows the comparison between the tuned π^\pm - ^{12}C scattering cross section in NEUT and the experimental data. The cumulative fractions of the π^0 -FSI are shown in Figure 4.3. The momentum and angular distributions of the scattered pions are determined from the results of the phase shift analysis of the π - N scattering experiments [62]. Because of the Pauli exclusion principle, the FSI nucleon momentum should be larger than the Fermi surface momentum given as follows;

$$p_F(r) = \left(\frac{3}{2} \pi^2 \rho(r) \right)^{\frac{1}{3}}, \quad (4.1)$$

where $\rho(r)$ is the nuclear density as a function of the distance r from the nuclear center. We use the Woods-Saxon nuclear density model [63] for the calculation of ρ as follows.

$$\rho(r) = \frac{\rho(0)}{1 + \exp\left(\frac{r-a}{b}\right)}, \quad (4.2)$$

where $\rho(0) = 0.48m_\pi^3$, m_π is the invariant mass of pions, $a = 2.69$ fm is the maximum nuclear radius of ^{16}O and $b = 0.41$ fm is the surface thickness of ^{16}O . Figure 4.4 shows both ρ and p_F as a function of r .

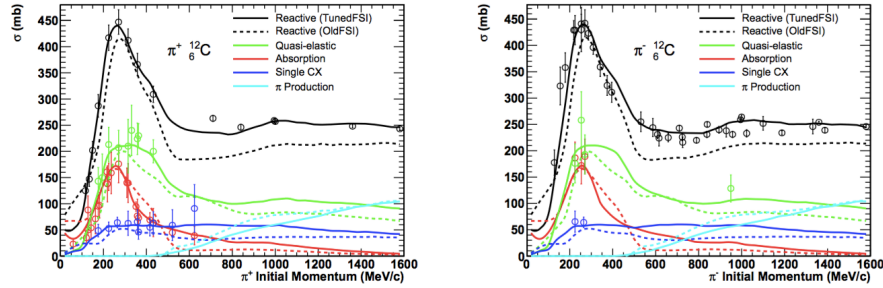


Figure 4.2: Cross sections for $\pi^+{}^{-12}\text{C}$ (left) and $\pi^-{}^{-12}\text{C}$ (right) as a function of pion initial momentum. The dots are for the experimental data, the solid lines are for the calculation by NEUT and the dotted lines are for the old FSI model. Taken from [61].

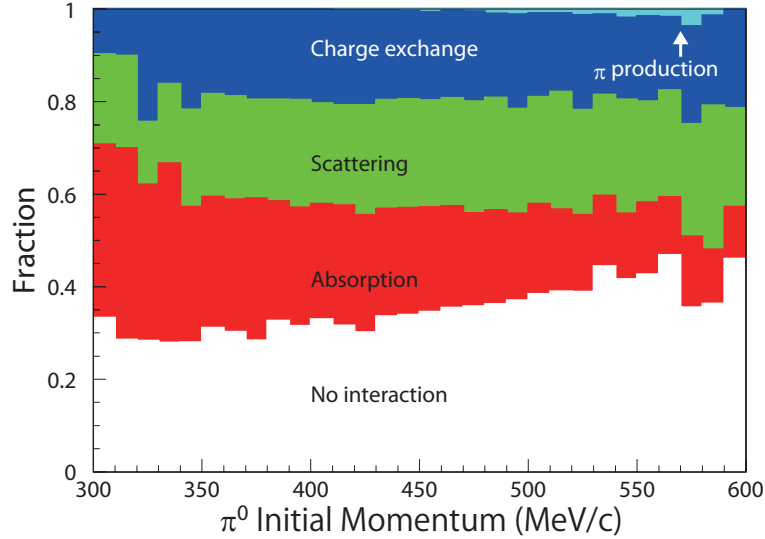


Figure 4.3: Cumulative fractions of the π^0 -FSI as a function of π^0 initial momentum. Taken from [1].

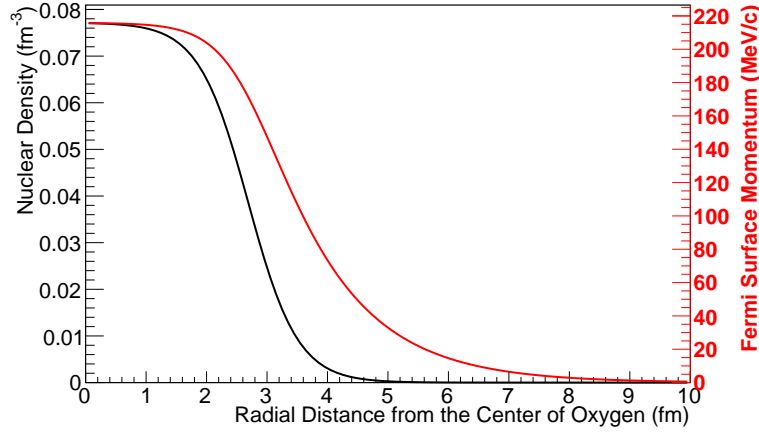


Figure 4.4: Woods-Saxon nuclear density (black) and the Fermi surface momentum (red) as a function of the radial distance from the center of ^{16}O .

After proton decay in ^{16}O , the remaining nuclei can be in an excited state and it de-excites through gamma-rays or nucleon emission. We simulate those emissions based on H. Ejiri[64].

4.2 Background

As for the background of proton decay, atmospheric neutrinos are only considered since other noise events are negligible. In this section, we discuss how many atmospheric neutrinos are expected to come in the SK detector and their interactions in water.

4.2.1 Neutrino Flux

The atmospheric neutrino flux at the Super-Kamiokande site is calculated by M. Honda *et al.* [65, 66], called the Honda flux. The Honda flux is estimated based on the primary cosmic ray flux measurements by the AMS [67, 68] and BESS [69, 70] experiments, and takes into account the effects of the solar activity and the geomagnetic field to the primary cosmic ray flux. The interaction of the primary cosmic ray with the atmosphere is calculated based on JAM [71] (primary cosmic ray energy for below 32 GeV) and DPMJET-III [72] (for above 32 GeV). Neutrino oscillations are not considered in the atmospheric neutrino MC, but those effects are taken into account by reweighing each MC event in the analysis step.

The expected zenith angle distributions of the atmospheric neutrino flux at SK by the Honda flux are shown in Figure 4.5. The peaks at the horizontal

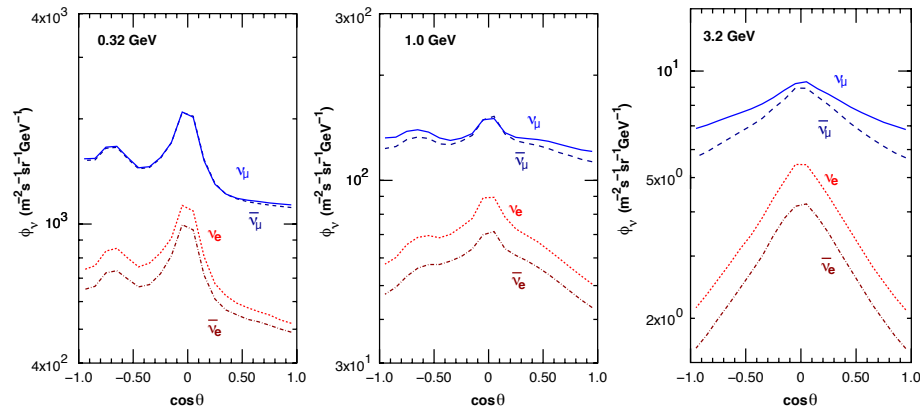


Figure 4.5: Expected zenith angle distributions of the atmospheric neutrino flux at SK by the Honda flux for the neutrino energies of 0.32 GeV (left), 1.0 GeV (middle) and 3.2 GeV (right). Taken from [66].

direction are due to a longer travel length of cosmic ray particles coming horizontally. Since there is the geomagnetic field, a large up-down asymmetry can be seen in the lowest energy plot. The direction-averaged atmospheric neutrino flux at SK by the Honda flux is shown in Figure 4.6 with other flux models such as the FLUKA [73] and the Bartol [74]. For this proton decay analysis, the neutrinos with the order 1 GeV energy can be the dominant background.

4.2.2 Neutrino Interactions

The interactions of neutrinos with the water are simulated by NEUT [59]. In the atmospheric neutrino MC, the interactions of neutrinos with hydrogen and oxygen nuclei are only simulated while neglecting the interaction of neutrinos with electrons since the cross section for neutrino-electron interactions is three orders of magnitude smaller than that for neutrino-nuclei interactions.

As described in the following sentences, there are roughly three categories for both Charged Current (CC) and Neutral Current (NC) interactions; (Quasi-)Elastic (QE) scattering, resonant (RES) productions and Deep Inelastic Scattering (DIS). Figure 4.7 shows the distributions of the CC ν_μ and $\bar{\nu}_\mu$ cross sections per nucleon as a function of neutrino energy in NEUT with the experimental data [75].

The particle type of neutrinos generated in the atmosphere are only ν_e and ν_μ . However, ν_τ can be arrived in SK through neutrino oscillations. The decay of produced τ is complex and is simulated by TAUOLA [76].

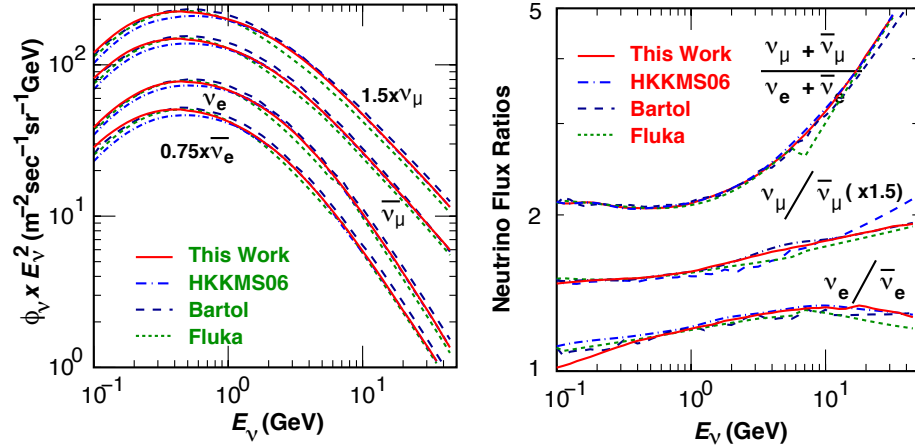


Figure 4.6: Direction-averaged atmospheric neutrino flux at SK by the Honda flux. The absolute flux is on the left and the the flux ratio is on the right. Taken from [66].

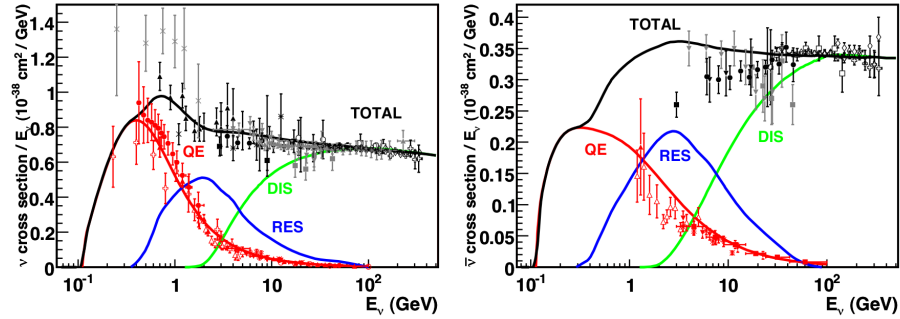


Figure 4.7: Cross sections per nucleon divided by neutrino energy as a function of neutrino energy for CC ν_μ (left) and $\bar{\nu}_\mu$ (right). Taken from [77].

Elastic and Quasi-Elastic Scattering

In NC elastic scattering, a neutrino just scatters off a nucleon without creating any particles. On the other hand, a neutrino is converted into a corresponding charged lepton in CC Quasi-Elastic (CCQE) scattering.

$$\nu + N \rightarrow l + N' \quad (4.3)$$

Here, N and N' are the initial and final nucleons. This interaction is the dominant process up to around 1 GeV. For free protons, the CCQE cross sections are simulated based on the Llewellyn-Smith model [78]. The modification model provided by Smith and Moniz [79] is used for a nucleon in ^{16}O (a relativistic Fermi gas model). The differential cross section of the model is a function of the square of the four-momentum transfer. The axial vector mass contained in a form factor of this model is set at 1.21 GeV based on the measurements of K2K [80] and MiniBooNE [81].

In the simple CCQE interaction described above, we assume that a neutrino interacts only with a single nucleon. However, the nucleons which are not the target nucleon may affect the interaction process, and such effect is suggested by MiniBooNE result [81]. This is known as the Meson Exchange Current (MEC) model [82]. Recently, NEUT has been modified to include the MEC effect which treats the interaction of a neutrino with a pair of two nucleons only for CCQE interactions as follows.

$$\nu + NN' \rightarrow l + N''N''' \quad (4.4)$$

Resonant Productions

By the delta resonance through neutrino interactions, a single meson or photon is produced as follows,

$$\nu + N \rightarrow l + N' + (\pi, \gamma, K, \eta). \quad (4.5)$$

In the previous version of NEUT used in the previous $p \rightarrow e^+\pi^0$ analysis [1], this is simulated based on the Rein and Sehgal model [83]. This model has been tuned using form factors from Graczyk *et al.* [84] in NEUT used in this thesis. The parameters in form factors of the modified model are obtained from the Argonne National Laboratory and Brookhaven National Laboratory bubble chamber experiments [85]. In this $p \rightarrow e^+\pi^0$ analysis, $\nu_e\text{CC}1\pi^0$ ($\nu_e\text{CC}1\pi^0$) become the dominant background as described in Chapter 7. By adopting this better model, the momentum transfer of W bosons is decreased and the outgoing lepton momentum becomes larger compared to the previous model. Thus, the total momentum of the $\nu_e\text{CC}1\pi^0$ events goes higher. Figure 4.8 shows the true outgoing electron momentum and true total momentum of $\nu_e\text{CC}1\pi^0$ events within a neutrino energy from 1 GeV to 3 GeV for the previous and current MC. As a result, the background for $p \rightarrow e^+\pi^0$ is reduced.

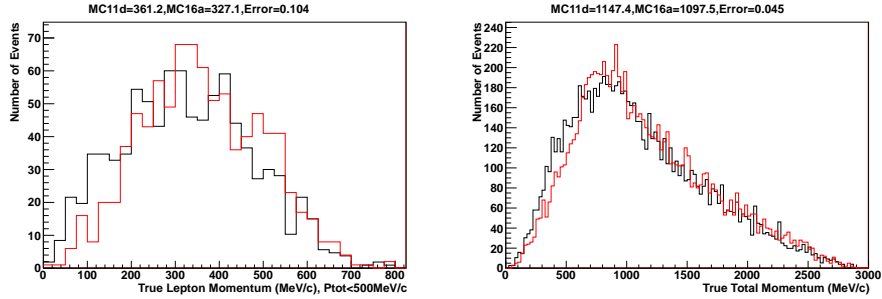


Figure 4.8: True outgoing electron momentum (left) and true total momentum (right) of $\nu_e CC1\pi^0$ events within a neutrino energy from 1 GeV to 3 GeV for the previous (black) and current MC (red). In the left figure, the events with the total momentum of less than 500 MeV/c are displayed.

Coherent pion production is a process in which a neutrino interacts with the entire oxygen nucleus and produces a forward-going pion as follows,

$$\nu + {}^{16}\text{O} \rightarrow l + {}^{16}\text{O} + \pi. \quad (4.6)$$

The Rein and Sehgal model [86] is used in NEUT for the coherent pion production.

Deep Inelastic Scattering

In a higher energy region above around 10 GeV, DIS becomes the dominant process. Such a high energy neutrino can interact with a constituent quark in the target nucleus and often produce multiple hadrons as follows,

$$\nu + N \rightarrow l + N' + \text{hadrons}. \quad (4.7)$$

This process is simulated based on the GRV98 parton distribution functions [87] and the corrections by Bodek and Yang [88]. The produced hadrons are only considered as pions in the region of $W < 2$ GeV, and its multiplicity is determined by the bubble chamber experiments [89, 90]. In the region of $W > 2$ GeV, heavier mesons (K and η) are also considered as the hadron production, which are simulated by PYHIA/JETSET [91].

4.3 Detector

Particles escaped from the nucleus in concern are simulated by a GEANT3 [92]-based detector simulation, called SKDETSIM. Particle interactions with water, particle decays and Cherenkov photon production are simulated by GEANT. For the hadronic interaction, GCALOR [93] and the NEUT pion cascade model are used for the interaction with the pions above and below 500 MeV/c, respectively.

The Cherenkov photon propagation in water is simulated by a custom code which includes Rayleigh/Mie scattering and the absorption of photons by H_2O and is tuned by the calibration results. For photons with short wavelength λ (≤ 450 nm), Rayleigh scattering is the dominant effect caused by small particles ($r \ll \lambda$, where r is the radius of a particle), which has the λ^{-4} dependence and scatters photons symmetrically in the forward and backward directions. The absorption of photons by H_2O is dominant for long wavelength (≥ 450 nm). Mie scattering is caused by large particles ($r \gg \lambda$) and makes a sharp peak in the forward region. The reflectivity of both the PMTs and black sheets is modeled and tuned by using the calibration results.

The PMT responses in both the time and charge and the electronics are also simulated based on the calibration measurements.

The output data structure of SKDETSIM is the same as that of the observed data. Thus, we can analyze both the data and MC events in the same way. In this thesis, 30,000 events of the $p \rightarrow e^+\pi^0$ MC generated randomly in the ID and the 3000 (500) years atmospheric neutrino MC for SK-IV (SK-I to -III) are used.

Chapter 5

Data Set

In this analysis, we use fully contained (FC) events whose vertices and all visible particles are contained inside the ID, in order to reconstruct the invariant mass and momentum of protons precisely. Most of FC events consist of atmospheric neutrino events. There are two other types in atmospheric neutrino events; partially contained (PC) and upward-going muon (UPMU). PC events are the events whose vertices are contained inside the ID, but any of the charged particles go outside. UPMU events are the high energy muons generated by upward-going neutrinos interacted with the rock surrounded the detector.

In order to prepare the FC data set, we need to remove background events caused by cosmic ray muons, radioactivities, solar and atmospheric neutrinos and so on. Through the following five reduction steps, we can reject background events except FC atmospheric neutrinos. Figure 5.1 shows the schematic drawing for various event types in SK. The reduction criteria are common for the data, atmospheric neutrino MC and proton decay MC.

5.1 First Reduction

The event trigger is fired at a rate of 10^6 times a day, most of which are low energy events coming from radioactive background and cosmic ray muon events. Those low energy background events can be largely rejected by applying the following criteria.

1. $PE_{300} \geq 200$ (≥ 100 for SK-II)
2. $NHITA_{800} \leq 50$ (≤ 55 for SK-IV) or OD trigger is off

where PE_{300} is the maximum number of total photoelectrons (p.e.s) observed with ID in a sliding 300 ns time window and $NHITA_{800}$ is the number of hit OD PMTs within a time window [-400 ns, +400 ns]. In the first cut, the cut threshold roughly corresponds to 22 MeV/c electrons. Therefore, most of radioactive background, low energy Michel electron from cosmic ray muons and solar neutrinos are rejected. Since the PMT density of SK-II is half that of

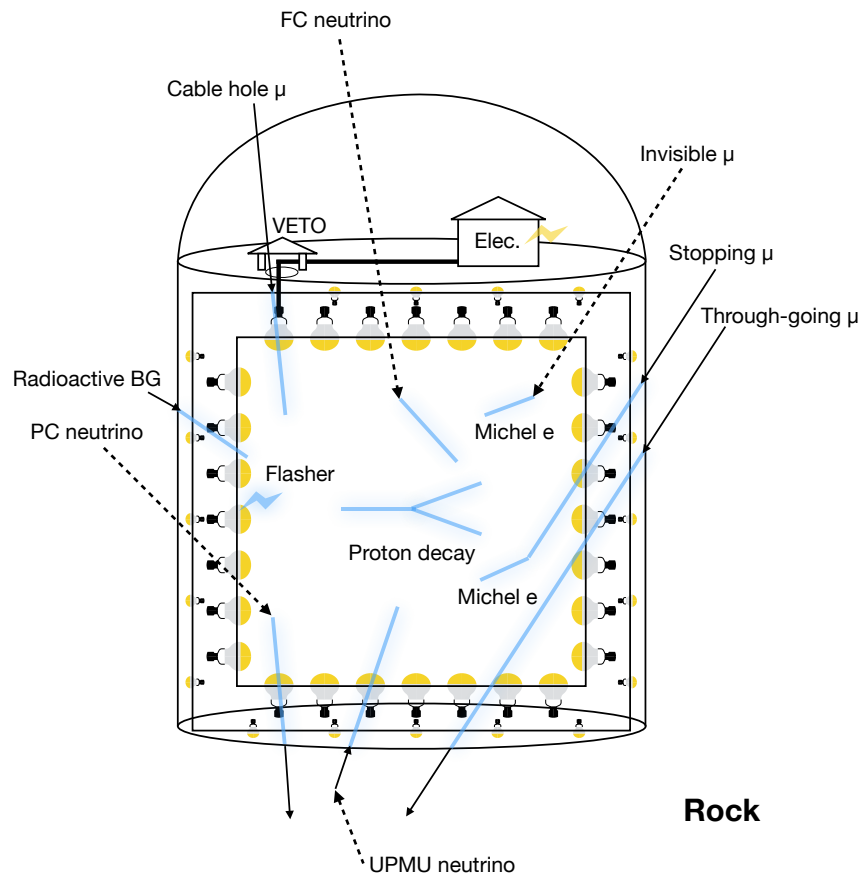


Figure 5.1: Schematic drawing for various event types in SK. Blue shows the emission of Cherenkov light.

the other detector periods, the half threshold is applied for SK-II. The second cut rejects not only cosmic ray muons, but also PC and UPMU events. The threshold in the second cut for SK-IV is adjusted to correct the changes in the OD electronics boards and the PMT gains. After the first reduction, the event rate is decreased to the order of 10^3 events/day.

5.2 Second Reduction

A more stringent rejection is performed in the second reduction compared to the first one. The events passed through the following criteria proceed to the third reduction.

1. $PE_{\max}/PE_{300} \leq 0.5$
2. $NHITA_{800} \leq 25$ (≤ 30 for SK-IV)
or $PE_{\text{tot}} \geq 100,000$ ($\geq 50,000$ for SK-II)

where PE_{\max} is the highest observed p.e.s among all hit ID PMTs and PE_{tot} is the sum of the observed p.e.s in the ID inside the time window. The first cut can reject electrical noise events caused by a single PMT which has a large hit. More rejection in OD activated events is done by the second cut while accepting very high energy FC events which have light leakage into the OD side. After the second reduction, the event rate decreases to the order of 100 events/day.

5.3 Third Reduction

The third reduction removes specific background events such as; hard muons, through-going muons, stopping-muons, cable hole muons, coincidence muons, flasher and low energy events. After the third reduction, the event rate decreases to around 40 events/day.

Hard Muon Cut

Cosmic ray muons which have an energy of ≥ 1 TeV, “hard” muons, would be rejected by the following cut;

- $NTHITA_{500} \geq 40$

where $NTHITA_{500}$ is the number of OD observed p.e.s in a sliding 500 ns time window.

Through-Going Muon Cut

Through-going muons which satisfy the following all criteria are rejected.

- $PE_{\max} > 231$
- Number of hit ID PMTs ≥ 1000

- $\text{NHITA}_{\text{in}} > 10$ or $\text{NHITA}_{\text{out}} > 10$
- Goodness of the through-going muon fit > 0.75

where NHITA_{in} ($\text{NHITA}_{\text{out}}$) is the number of hit OD PMTs in the muon entrance (exit) hit cluster. The goodness of a through-going muon event is evaluated by using the observed hit time, its resolution and the expected hit time calculated by the muon entering time and its track information.

Stopping Muon Cut

Similar to through-going muon cut, stopping muon events are rejected by the following cut;

- $\text{NHITA}_{\text{in}} \geq 10$ when the goodness of the stopping-muon fit ≥ 0
and only for SK-I, $\text{NHITA}_{\text{in}} \geq 5$ when the goodness of the stopping-muon fit ≥ 0.5

Cable Hole Muon Cut

Twelve cable holes for PMT's signal and high voltage cables are located on the top of the tank. No OD PMTs were installed under four holes out of twelve. These holes admit cosmic ray muons to enter the detector without OD activity. To reject those "cable hole muons," four veto counters (2.0 m \times 2.5 m plastic scintillation counters) were installed on each hole. The reduction criteria are as follows;

- One veto counter hit
and a distance from the reconstructed vertex to the cable holes in both the x and y direction is ≤ 4 m

Coincidence Muon Cut

Cosmic ray muons sometimes enter the detector just after a SLE trigger by coincidence. The following cuts reject these events.

- Number of hit OD PMTs in a fixed time window between +300 ns and +800 ns ≥ 20
and number of ID observed p.e.s in a fixed time window between +300 ns and +800 ns > 5000 p.e.s (2500 p.e.s for SK-II)

Flasher Event Cut

Light emission from a PMT itself occurs sometimes due to an electrical discharge, which may look a FC-like event. This is called "flasher" event. Usually the hit timing distribution of flasher events is longer than that of particle induced events. Flasher events which emit light for a longer time can be rejected by the following cuts;

- $N_{\text{MIN}_{100}} \geq 20$ (15 for SK-I)
or, only for SK-I, $N_{\text{MIN}_{100}} \geq 10$ if the number of hit ID PMTs ≤ 800
- Goodness of the time-of-flight fitter ≤ 0.4

where $N_{\text{MIN}_{100}}$ is the minimum number of hit ID PMTs in a sliding 100 ns time window between +200 ns and +700 ns. Since the TOF vertex fit for a flasher event will not work well, the second term is applied for the reduction.

Low Energy Event Cut

The remaining low energy events such as the radioactive background and electrical noise are subtracted by;

- $N_{\text{HIT}_{50}} < 50$ (25 for SK-II)

where $N_{\text{HIT}_{50}}$ is the number of time-of-flight corrected ID hits in a sliding 50 ns time window. This threshold corresponds to the visible energy of about 9 MeV.

5.4 Fourth Reduction

Flasher events are further rejected by the fourth reduction using a likelihood method. It is empirically known that flasher PMTs repeatedly emit light in a particular way and leave similar hit patterns. A typical flasher event is displayed in Figure 5.2. The flasher likelihood consists of three parameters evaluated between two events; a correlation factor r using the charge patterns, a parameter d_{KS} comparing the time distribution of the charge by a Kolmogorov-Smirnov test and a parameter which indicates whether the PMT with the highest p.e. is consistent between two events or not. Dividing the ID wall into 1450 patches of $2 \text{ m} \times 2 \text{ m}$ square, the correlation factor r is calculated by;

$$r = \frac{1}{N} \sum_i^N \frac{(Q_{\text{A},i} - \langle Q_{\text{A}} \rangle)(Q_{\text{B},i} - \langle Q_{\text{B}} \rangle)}{\sigma_{\text{A}}\sigma_{\text{B}}} \quad (5.1)$$

where N is the number of patches, $Q_{\text{A(B)},i}$ is the total observed p.e.s in the i -th patches for the event A (B), $\langle Q_{\text{A(B)}} \rangle$ and $\sigma_{\text{A(B)}}$ are the averaged observed p.e.s and their RMS. The likelihood cut value is determined by comparing the atmospheric neutrino MC and a hand selected real flasher sample. Both two events are rejected as flasher when their likelihood value is higher than the cut value. The fourth reduction removes a few events/day.

5.5 Fifth Reduction

The fifth reduction rejects the remaining cosmic ray muons and flasher events, electronic noise and calibration related events. The fifth reduction removes a few events/day.

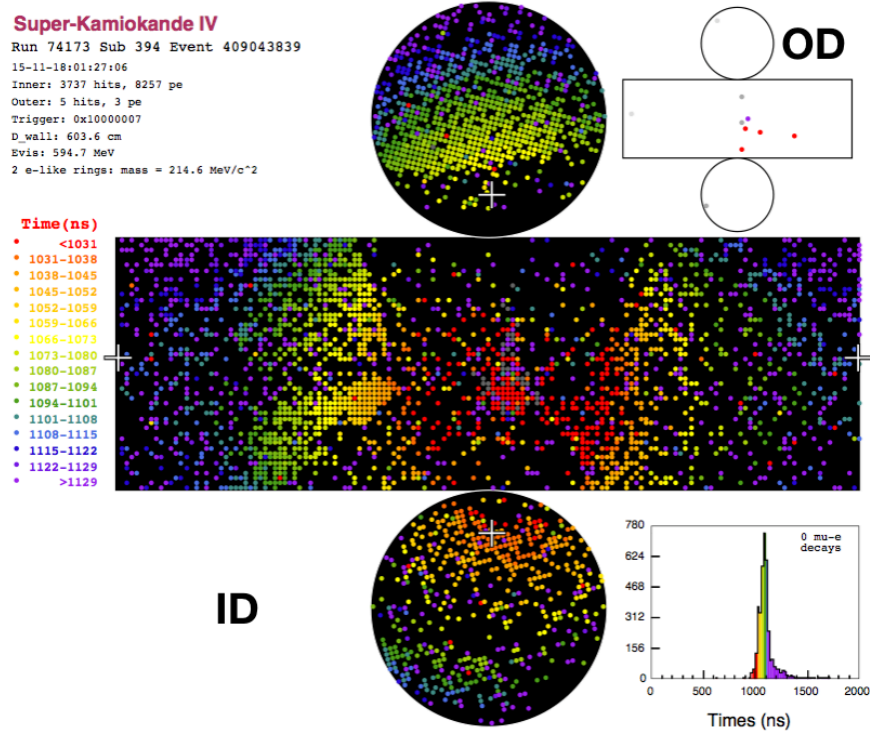


Figure 5.2: Typical flasher event display in SK-IV. The color indicates the hit timing (red: early hit, blue: late hit). A PMT located in the center of the tank suddenly flashed light. This type of the hit pattern hardly occurs by proton decay and atmospheric neutrino events.

Stopping Muon Cut

The improved reduction criterion is used for stopping muon events.

- $\text{NHITA}'_{\text{in}} \geq 10$

or,

- Goodness of the stopping muon fit ≥ 0.5 and $\text{NHITA}'_{\text{in}} \geq 5$

where $\text{NHITA}'_{\text{in}}$ is the number of hit OD PMTs in the muon entrance (exit) hit cluster without an OD timing correction.

Cable Hole Muon Cut

Considering the case of no veto counter hit, but cosmic ray muons enter the detector through the cable holes, tighter cuts based on the reconstruction parameters are necessary. The following criteria are used only for SK-IV.

- Goodness of stopping muon fit ≥ 0.4
and $\text{PE}_{\text{tot}} > 4000$
and $\cos(z)$ of muon's direction < -0.6
and the distance between the muon entering point and the nearest cable hole < 250 cm
- $\text{NHITA}_{\text{APfit}} \geq 4$

where $\text{NHITA}_{\text{APfit}}$ is the number of hit OD PMTs within 8 m from the muon entering point fitted by an event reconstruction algorithm, APfit (see Chapter 6), in a sliding 200 ns time window from -400 ns to $+400$ ns.

Coincidence Muon Cut

In addition to the coincidence muon cut in the third reduction, a tighter cut is applied as follows.

- $\text{PE}_{500} < 300$ p.e.s (150 p.e.s for SK-II) and $\text{PE}_{\text{late}} \geq 20$ p.e.s

where PE_{500} is the total number of observed ID p.e.s in a fixed time window between -100 ns and $+400$ ns and PE_{late} is the maximum number of hit OD PMTs in a sliding 200 ns time window from $+400$ ns to $+1600$ ns.

Invisible Muon Cut

Cosmic ray muons below the Cherenkov threshold, “invisible” muons, can enter the ID without PMT hits and decay into Michel electrons. These Michel electrons can emit light inside the ID, then it looks like FC event. The invisible muon events which satisfy the following criteria are rejected;

- $\text{PE}_{\text{tot}} < 1000$ p.e.s (500 p.e.s for SK-II)

- $\text{NHITAC}_{\text{early}} \geq 5$
- $\text{NHITAC}_{\text{early}} + \text{NHITAC}_{500} \geq 10$ (if $\text{DIST}_{\text{clust}} < 500$ cm)

where $\text{NHITAC}_{\text{early}}$ is the maximum number of hit OD PMTs in a sliding 200 ns time window from -8900 ns to -100 ns, NHITAC_{500} is the number of hit OD PMTs in a fixed time window between -100 ns and $+400$ ns and $\text{DIST}_{\text{clust}}$ is a distance between two OD hit clusters used for the $\text{NHITAC}_{\text{early}}$ and the NHITAC_{500} .

Long-Tail Flasher Event

A tighter cut for the flasher events than the third reduction is conducted as follows;

- $\text{NMIN}_{100} \geq 6$ and the goodness of the TOF fitter < 0.4

or,

- $\text{NMIN}_{100} < 6$
and the goodness of the TOF fitter < 0.3 for SK-II to SK-IV only

Electronics Related Event

The electronic noise from the high voltage systems or electronics boards can create a lot of fake hits. The following criterion removes the electronic noise events.

- $N_0 \geq 250$ (125 for SK-II) and $N_0 - N_1 \geq 100$ (50 for SK-II)

where N_0 (N_1) is the number of hit ID PMTs with a less (greater) than a single p.e.

Dead Electronics Hut

Due to some trouble, it could happen the electronics huts turn to be off. In order to check whether the hut is active or not, the following criterion is necessary.

- All electronics huts have at least one OD hits.

Wrong OD Timing

In the phase of SK-I to SK-III, the OD timing was occasionally out of the synchronization with the ID timing. This problem caused large early timing clusters in the OD or the abnormal number of sub-events. Thus, the following criteria are applied for SK-I to SK-III only.

- $\text{PE}_{\text{tot}} \geq 1000$ (500 for SK-II)
and $\text{NHITAC}_{\text{early}} \geq 20$ and the number of sub-events is 7.

Calibration Related Event Cut

Some events for the calibration by a laser or a xenon lamp can be contaminated in the data set due to some trouble. But, using the information from the monitored PMTs for the calibration sources, it is possible to remove those events as follows.

- Number of reference PMT hits for the laser and the xenon lamp is zero.

5.6 Final FC Data Set

Finally, the FC data set for this analysis is obtained after applying the following criteria.

- $D_{\text{wall}} > 1.5$ m for fitQun (2.0 m for APfit)
- NHITAC < 16 (< 10 for SK-II)
- $E_{\text{vis}} > 30$ MeV

where D_{wall} is the distance from the wall and the reconstructed vertex, NHITAC is the number of hit OD PMTs in the largest charge cluster and E_{vis} is the visible energy which is defined as the total energy of all reconstruction rings assuming all of them are originated by electrons. FitQun is a newly developed event reconstruction algorithm and has better performances than APfit as described in Chapter 6.

In addition to the automated FC reduction, a real time check in the data quality is conducted by human eyes for the events after the third reduction. The scanners check the hit charge and timing distribution and the hit pattern for both the ID and OD using an event display tool, judge whether the reduction algorithm works properly or not and be aware of something unusual (for instance, Appendix A).

The final event rate is about 8 events/day. The reduction efficiencies of each reduction step for the data, atmospheric neutrino MC and $p \rightarrow e^+ \pi^0$ MC in SK-IV are shown in Table 5.1.

Table 5.1: Reduction efficiencies of each reduction step for the data (from Sep. 2008 to Aug. 2016, 2650.4 live days), atmospheric neutrino MC and $p \rightarrow e^+\pi^0$ MC in SK-IV. The true- $D_{\text{wall}} > 2$ m cut is used to the calculation of the rates for MC. Here, the fiducial volume cut in the final reduction is $D_{\text{wall}} > 2$ m.

Reduction	Data	Atm.- ν MC	$p \rightarrow e^+\pi^0$ MC
1st	1771.31 day ⁻¹ (4694674 events)	99.99%	99.98%
2nd	274.40 day ⁻¹ (727266 events)	99.99%	99.93%
3rd	39.55 day ⁻¹ (104830 events)	99.83%	99.72%
4th	37.19 day ⁻¹ (98575 events)	98.87%	98.19%
5th	34.46 day ⁻¹ (91336 events)	98.83%	97.94%
Final	8.08 day ⁻¹ (21410 events)	98.07%	97.94%

Chapter 6

Event Reconstruction

The event reconstruction algorithm (fitter) works to determine the event properties such as the vertex, number of Cherenkov rings, particle type and momentum. There are two different fitters; one is an existing fitter (APfit) used since the beginning of SK, the other one is a newly developed fitter based on the maximum likelihood method (fitQun).

In this Chapter, we first describe the reconstruction scheme of both fitters and then discuss their performance. After that, the fiducial volume and energy scale for fitQun are discussed. The same algorithm is applied to both the fully-contained data and MC. FiTQun is applied only for SK-IV while APfit is applied for SK-I to SK-IV.

6.1 Overview of Two Algorithms

The conventional event reconstruction algorithm, APfit, was developed in late 1990's and contributed to the discovery of atmospheric neutrino oscillation and the K2K and T2K experiments. APfit is a step-by-step fitter by using the time and charge information of hit PMTs. Thanks to the remarkable evolution of CPU power, we can reconstruct events more precisely. The improved event reconstruction algorithm, fitQun, is a maximum likelihood fitter which uses not only hit T&Q information but also the information of non-hit (“unhit”) PMTs. Using simultaneous fitting method and more information, the precision of reconstruction of fitQun is much better than that of APfit. FiTQun is able to fit the vertex ring-by-ring, number of rings up to six and particle identification under the three particle hypotheses (e , μ , charged- π). On the other hand, APfit can fit the single-vertex, number of rings up to five and particle identification under the two particle hypotheses (e , μ).

Based on the reconstruction method used in the MiniBooNE experiment [94], fitQun was initially developed by the T2K collaboration for the SK-IV detector as a far detector of T2K. For SK analyses, we have improved fitQun not only for SK-IV but also the other detector periods. We have validated fitQun for SK-IV

Table 6.1: Characteristics of fitQun and APfit.

	fitQun	APfit
Type	Maximum Likelihood Fitter	Step-by-Step Fitter
Vertex	Multi-Vertices	Single-Vertex
Ring Counting	6-rings (max.)	5-rings (max.)
Particle Identification	e, μ , charged- π	e, μ
Availability (2016)	SK-IV	SK-I to SK-IV

analysis, but we need more tuning of fitQun including the detector simulation for the other SK phases (see Appendix C). Therefore, we use fitQun for the data analysis in SK-IV. Table 6.1 shows the characteristics of fitQun and APfit. The process speed of the fitQun (APfit) multi-ring fit in our computer system is about 8.8 min (1.3 min) per events for the atmospheric neutrino MC events preselected as the background events of $p \rightarrow e^+\pi^0$ described in Appendix D.

6.2 APfit

In this section, we review the reconstruction scheme of APfit. The detail information can be found in [95]. The event reconstruction of APfit is done as following steps.

1. Vertex fitting
2. Ring counting
3. Particle identification
4. Momentum determination
5. Michel electron search

For single-ring events determined in the second step, a more precise vertex fit is done by using the Cherenkov ring pattern depending on the particle type. However, it is not available for multi-ring events and thus not used in this analysis.

6.2.1 Vertex Fitting

The first step of the reconstruction is to define the vertex position. There are three processes: first, “point-fit” roughly finds the vertex, then a search for the edge of the most energetic Cherenkov ring and its direction is performed using that vertex. Finally, “TDC-fit” redetermines the vertex taking into account the finite particle track length and the scattered light.

Point-fit is performed assuming that Cherenkov light is emitted from a single point. For a test vertex \mathbf{x} , the time-of-flight (TOF) subtracted hit timing distribution is calculated. That distribution becomes narrower when \mathbf{x} comes close to the true vertex. By maximizing the following goodness function, the point-fit vertex can be derived.

$$\text{Goodness} = \frac{1}{N} \sum_i \exp\left(-\frac{(t_i(\mathbf{x}) - t_0)^2}{2(1.5\sigma)^2}\right) \quad (6.1)$$

where N is the number of hit PMTs, t_i is the TOF subtracted timing of the i -th PMT, t_0 is the interaction time maximizing the goodness, the factor 1.5 is chosen to optimize the fitting performance and σ is the PMT timing resolution of 2.5 ns.

The next step is to search the ring edge and the direction of the most energetic Cherenkov ring. The observed charge distribution depending on the Cherenkov angle θ , $\text{PE}(\theta)$, can be calculated using the point-fit vertex and assuming a test direction, which is shown in Figure 6.1. Then, the ring edge θ_{edge} under that assumption can be found where the following conditions are satisfied.

$$\frac{d^2\text{PE}(\theta)}{d^2\theta} = 0 \quad (6.2)$$

By maximizing the following estimator $Q(\theta_{\text{edge}})$, the edge and the direction of the most energetic Cherenkov ring are determined.

$$Q(\theta_{\text{edge}}) = \frac{\int_0^{\theta_{\text{edge}}} \text{PE}(\theta) d\theta}{\sin \theta_{\text{edge}}} \left(\left[\frac{d\text{PE}(\theta)}{d\theta} \right]_{\theta=\theta_{\text{edge}}} \right)^2 \exp\left(-\frac{(\theta_{\text{edge}} - \theta_{\text{exp}})^2}{2\sigma_\theta^2}\right) \quad (6.3)$$

where θ_{exp} and σ_θ are the expected Cherenkov angle using the total charge inside the cone and its resolution, respectively.

Finally, TDC-fit adjusts the vertex more precisely taking into account the finite particle track length and the scattered light. The initial track length is estimated from the total charge and an assumption of 3 MeV/cm energy deposits. The timing residual for PMTs inside the cone is calculated assuming the Cherenkov light is emitted along the track with the same angle. For PMTs outside the cone, the timing residual is calculated assuming the Cherenkov light is emitted at the vertex considering the scattering parameters. The final vertex of the most energetic ring is determined by maximizing an estimator.

6.2.2 Ring Counting

The next step is to search for additional Cherenkov rings. Candidate rings are found by a shape extraction algorithm known as the Hough transform. Figure 6.2 shows an illustration of this idea. For each hit PMT, virtual circles (dashed line) centered on each PMT position are drawn with 42° half angle. The direction of the intersection of those virtual rings is used as the direction of the additional ring. Then, the candidate ring are judged whether it is a fake

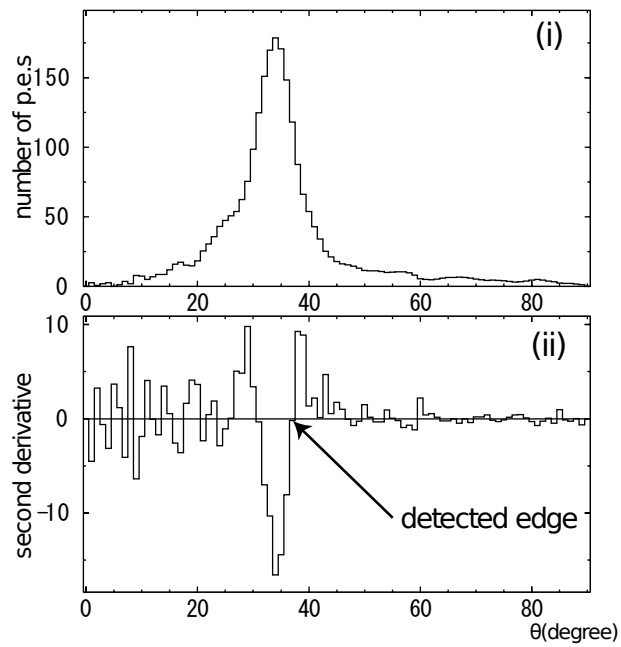


Figure 6.1: An observed charge distribution depending on the Cherenkov angle (top) and its second derivative (bottom). Taken from [96].

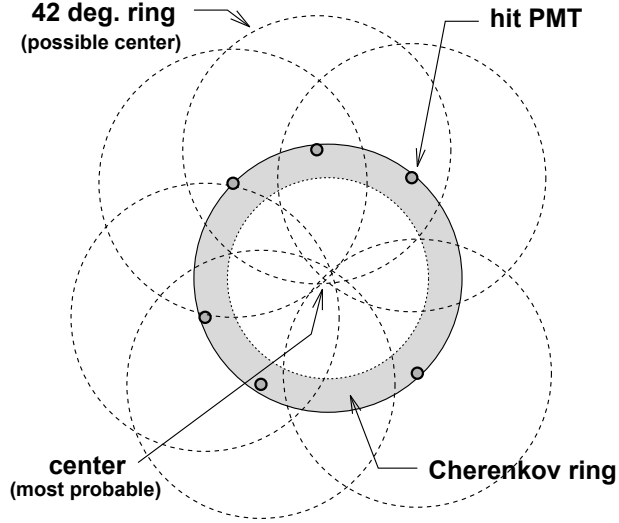


Figure 6.2: Illustration of the ring finding principle. Taken from [96].

ring or not by a log likelihood method. The likelihood consists of the observed and expected charge. This ring counting continues up to five rings by default. Figure 6.3 shows the ring counting likelihood distribution for the FC sub-GeV (visible energy < 1.33 GeV) sample of the data and the atmospheric neutrino MC.

6.2.3 Particle Identification

After the ring counting, the particle type of each ring is estimated by the particle identification (PID) process. Electrons or gamma-rays create fuzzy Cherenkov rings by electromagnetic showering (e -like rings). On the other hand, Cherenkov rings which have sharp ring edges are created by muons or charged-pions (μ -like rings). Moreover, the Cherenkov angle of e -like rings are almost constant at 42° , but that of μ -like rings can vary depending on their momenta and energy losses. PID can classify the particle type into e -like or μ -like by using these differences in the ring patterns and the angles.

PID likelihoods are built with two particle type hypotheses for each ring and used for PID. The likelihood consists of the observed and expected charge. The expected charge is evaluated from the SK MC simulations and given as follows.

$$q_{\text{exp},i}(e) = \alpha_e Q_{\text{exp}}(p_e, \theta_i) \left(\frac{R}{r_i} \right)^{3/2} e^{-r_i/L} f(\Theta_i) + q_{\text{scat},i} \quad (6.4)$$

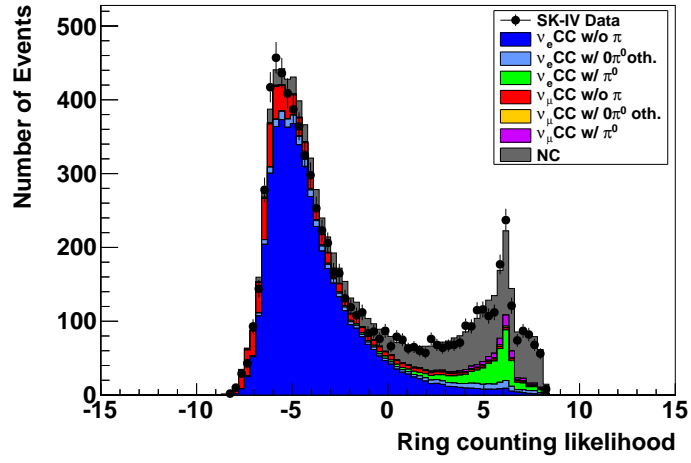


Figure 6.3: Ring counting likelihood distribution for the FC sub-GeV sample of the data (black points) and the atmospheric neutrino MC (stacked histograms) in SK-IV. The events whose reconstructed vertices are within the region 2 m inside from the nearest wall without tagged Michel electrons are selected. The events in the positive (negative) side are identified as multi- (single-) ring events.

$$q_{\text{exp},i}(\mu) = \left(\frac{\alpha_\mu \sin^2 \theta_{x_i}}{r_i \left(\sin \theta_{x_i} + r_i \left[\frac{d\theta}{dx} \right]_{x=x_i} \right)} + q_{\text{knock},i} \right) e^{-r_i/L} f(\Theta_i) + q_{\text{scat},i} \quad (6.5)$$

where

α_e, α_μ : normalization factor

$Q_{\text{exp}}(p_e, \theta_i)$: expected charge distribution depending on the electron momentum and the angle θ_i for the i -th PMT

R : virtual sphere radius (16.9 m)

r_i : distance from the vertex to the i -th PMT

L : light attenuation length in water

$f(\Theta_i)$: angular acceptance as a function of the photon injection angle Θ_i for the i -th PMT

$q_{\text{scat},i}$: expected charge due to scattering light for the i -th PMT

θ_{x_i} : Cherenkov angle of a muon track length at x

$q_{\text{knock},i}$: expected charge due to knock-on electrons for the i -th PMT

Figure 6.4 shows the PID likelihood distributions for the FC sub-GeV single-ring and multi-ring sample of the data and the atmospheric neutrino MC.

6.2.4 Momentum Determination

The momentum of each particle is evaluated by the observed charge inside the Cherenkov cone with a half angle of 70° . The observed charge of the i -th PMT for the n -th ring is separated based on the expected charge distributions from each ring, described as follows;

$$q_{\text{obs},i,n} = q_{\text{obs},i} \frac{q_{\text{exp},i,n}}{\sum_{n'} q_{\text{exp},i,n'}}. \quad (6.6)$$

By correcting the light attenuation and angular acceptance of the PMTs, the total charge for each ring (RTOT) is calculated as follows;

$$RTOT = \frac{G_{\text{MC}}}{G_{\text{Data}}} \left[\alpha \sum_{\theta_{i,n} < 70^\circ, -50 \text{ ns} < t_i < 250 \text{ ns}} \left(q_{\text{obs},i,n} e^{r_i/L} \frac{\cos \Theta_i}{f(\Theta_i)} \right) - \sum_{\theta_i < 70^\circ} S_i \right] \quad (6.7)$$

where

$G_{\text{MC}}, G_{\text{Data}}$: relative PMT gain parameter for the data and the MC simulation

α : normalization factor

$\theta_{i,n}$: angle between the i -th PMT and the n -th ring direction

t_i : TOF subtracted hit timing of the i -th PMT

S_i : expected charge of the i -th PMT due to scattering light.

RTOT is converted to the corresponding momentum depends on the PID of the ring (e -like or μ -like) using conversion tables obtained from MC.

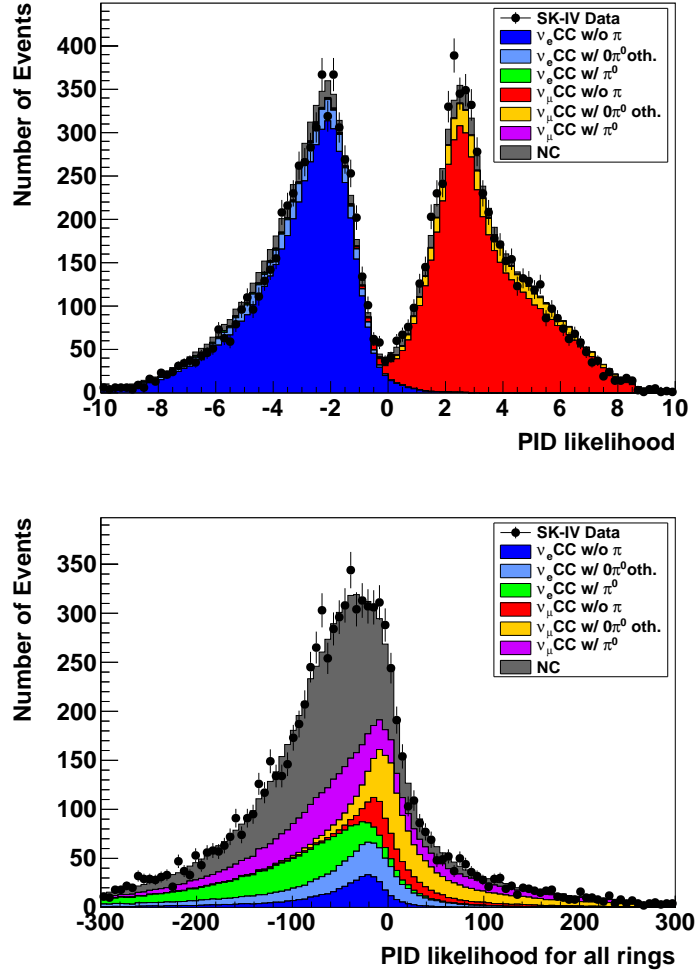


Figure 6.4: PID likelihood distributions for the FC sub-GeV single-ring (top) and multi-ring (bottom) sample of the data (black points) and the atmospheric neutrino MC (stacked histograms) in SK-IV. Here, the events whose reconstructed vertices are within the region 2 m inside from the nearest wall are selected. The events in the positive (negative) side are identified as muon- (electron-) like events.

6.2.5 Michel Electron Tagging

Michel electrons are an indicator of the existence of a muon. The tagging of Michel electrons is conducted based on the number of hits in a cluster, the total charge and the goodness of the vertex fit. Due to an impedance mismatch seen in the ATM boards, the time interval between 800 ns and 1,200 ns from the primary event timing is excluded from the tagging for SK-I to SK-III. But, that time interval is available for SK-IV since the mismatch was solved in the QBEE boards. Therefore, the tagging efficiency for SK-IV is higher than the other detector periods. The tagging efficiency of Michel electrons is 80% for μ^+ and 63% for μ^- for SK-I to SK-III, 96% for μ^+ and 80% for μ^- for SK-IV.

6.3 fitQun

First of all, we discuss the likelihood function since fitQun is kind of maximum likelihood fitter. Then, the reconstruction procedure of fitQun is shown as the following steps.

1. Vertex pre-fitter
2. Hit clustering
3. Single-ring fitter
4. Multi-ring fitter

The document [97] can provide much more information about fitQun.

6.3.1 Likelihood Function

The event reconstruction is conducted by maximizing the following likelihood function,

$$L(\mathbf{x}) = \prod_j^{\text{unhit}} P_j(\text{unhit}|\mathbf{x}) \prod_i^{\text{hit}} \{1 - P_i(\text{unhit}|\mathbf{x})\} f_q(q_i|\mathbf{x}) f_t(t_i|\mathbf{x}). \quad (6.8)$$

where \mathbf{x} is a track parameter set of { vertex position (x, y, z) , time (t) , zenith angle (θ) , azimuth angle (ϕ) , momentum (p) }, $P(\text{unhit}|\mathbf{x})$ ($1 - P(\text{unhit}|\mathbf{x})$) indicates the unhit (hit) probability, $f_q(q_i|\mathbf{x})$ and $f_t(t_i|\mathbf{x})$ are the probability density functions (PDFs) of the observed charge and time, respectively. The hit (unhit) probability function is multiplied for all hit (unhit) PMTs. This likelihood function can be simplified by introducing a predicted charge (μ) instead of \mathbf{x} .

$$L(\mathbf{x}) = \prod_j^{\text{unhit}} P_j(\text{unhit}|\mu_j) \prod_i^{\text{hit}} \{1 - P_i(\text{unhit}|\mu_i)\} f_q(q_i|\mu_i) f_t(t_i|\mathbf{x}). \quad (6.9)$$

Then, the unhit probability function and charge PDF become independent of the Cherenkov photon emission profile, these are determined by the characteristics of PMTs and its readout electronics. The time likelihood also uses the predicted charge as described below. For the likelihood calculation, the predicted charge for each PMT for a given track parameter set is evaluated at first, and the likelihood is then evaluated based on the predicted charge and the observed charge and time information.

Predicted Charge

For a given single particle hypothesis \boldsymbol{x} , the predicted charge of each PMT is estimated for the direct (μ^{dir}) and indirect light (μ^{sct}), separately. In the case of a multi-particle hypothesis, the predicted charge is independently calculated for the n -th particle hypothesis and summed for all particle hypotheses as follows.

$$\mu_i = \sum_n (\mu_{i,n}^{\text{dir}} + \mu_{i,n}^{\text{sct}}) + \mu^{\text{dark}} \quad (6.10)$$

where μ^{dark} indicates the contribution from the PMT dark rate taken from SKDETSIM (5.7195 kHz for SK-IV) for a time window which is described in Section 6.3.3. For a single particle hypothesis, μ^{dir} and μ^{sct} are given as an integral along the particle track length s from its initial position;

$$\mu^{\text{dir}} = \Phi(p) \int ds g(p, s, \cos \theta) \Omega(R) T(R) \epsilon(\eta) \quad (6.11)$$

and

$$\mu^{\text{sct}} = \Phi(p) \int ds \frac{1}{4\pi} \rho(p, s) \Omega(R) T(R) \epsilon(\eta) A(s) \quad (6.12)$$

where the variables θ , R , η indicate the relative orientation of the particle and the PMT which are all function of s as shown in Figure 6.5. $\Phi(p)$ is a normalization factor which is proportional to the average total number of photons for the particle with initial momentum p . In the following sentences, we describe the following factors: the Cherenkov emission profile g , the PMT solid angle factor Ω , the light transmission factor T , the PMT angular acceptance ϵ , the photo emission fraction ρ and the light scattering factor A .

First of all, we need to know how much Cherenkov photons are emitted along the particle track s . The Cherenkov emission profile $g(p, s, \cos \theta)$ is the number of emitted photons per unit track length per unit solid angle at angle θ with respect to the particle direction for the particle with initial momentum p . The normalization of g is given as;

$$\int g(p, s, \cos \theta) ds d\Omega = 1. \quad (6.13)$$

Figure 6.6 and 6.7 show the Cherenkov profiles for electrons and muons which are generated by injecting a single particle with various momenta in SKDETSIM.

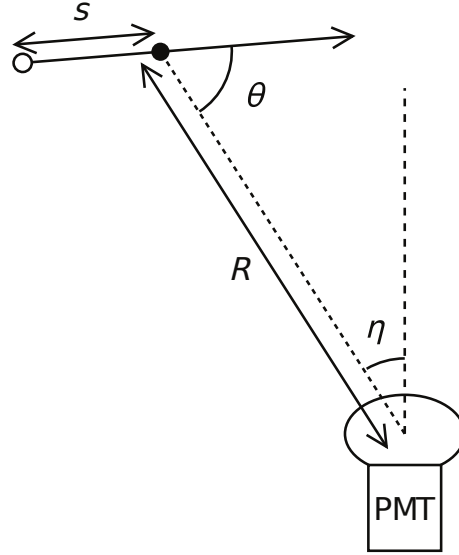


Figure 6.5: Schematic diagram of the relation between the variables for the predicted charge. The vertex position of the particle is shown as the white dot. Taken from [97].

The photon emission angles for electrons are almost constant and have the broad distributions, whereas that for muons are depending on the momentum and have the sharper distribution. These differences enable us to distinguish the particle type.

Next, we need to know how Cherenkov photons are received by the PMT. For that purpose, the solid angle $\Omega(R)$ for the PMT is roughly evaluated as follows.

$$\Omega(R) = \frac{\pi a^2}{R^2 + a^2} \quad (6.14)$$

where a is the radius of the ID PMT (0.254 m). This formula is valid at distance $R > 1$ m. While traveling the distance from the emitting point to the PMT, photons can be absorbed or scattered in water. Such effects are considered by the light transmission factor $T(R)$.

$$T(R) = \exp(-R/L^{\text{att}}) \quad (6.15)$$

where L^{att} is the light attenuation length in water used in SKDETSIM (74.9646 m for SK-IV). The PMT angular acceptance $\epsilon(\eta)$ should be taken into account. Figure 6.8 shows the angular acceptance as a function of the angle η between the PMT normal and the direction of the particle position viewed from the PMT, which is obtained from SKDETSIM. The fitted polynomial function is used in

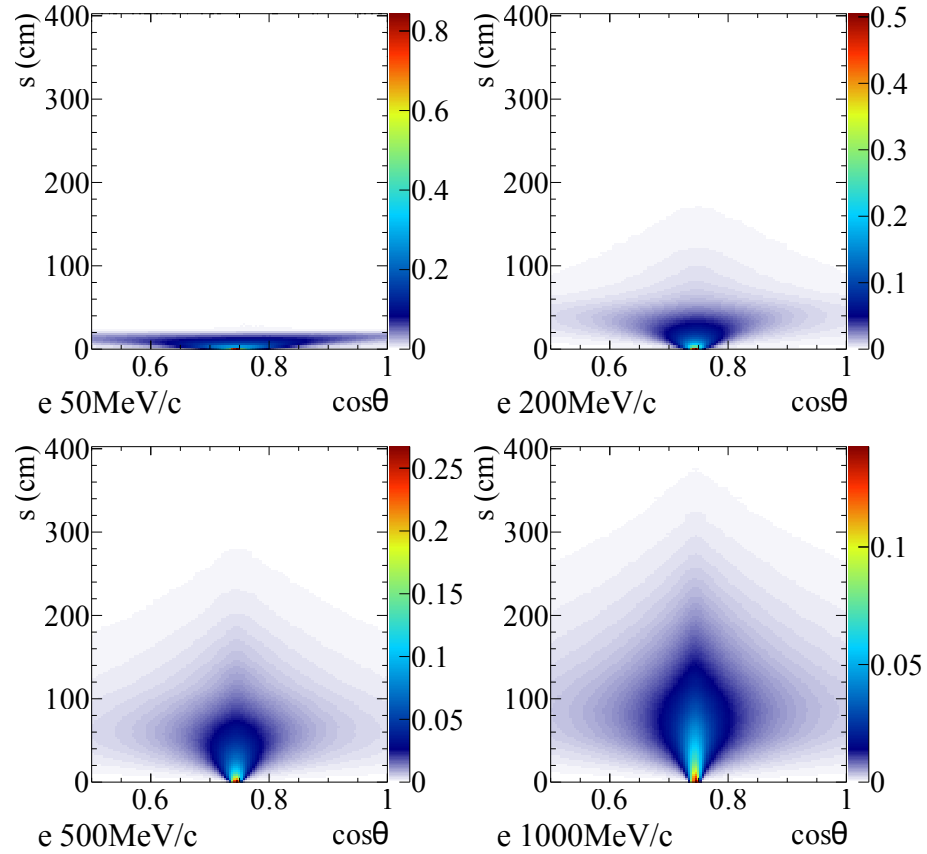


Figure 6.6: Cherenkov emission profiles for electrons at various initial momenta. In all the figures, the photon emission angles have board distributions and are peaked at around $\cos\theta = 0.75$ which corresponds to the Cherenkov angle for a particle with $\beta = 1$ in water. Taken from [97].

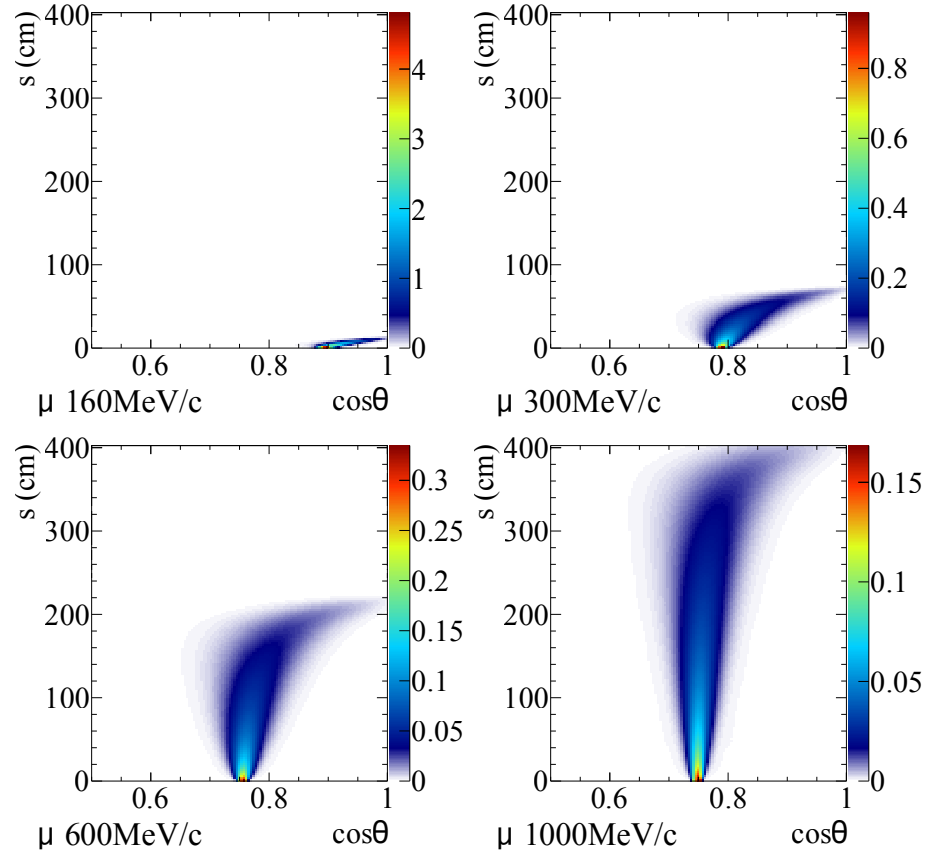


Figure 6.7: Cherenkov emission profiles for muons at various initial momenta. In all the figures, the photon emission angles have shaper distributions and stronger dependence on momentum compared to electrons. Taken from [97].

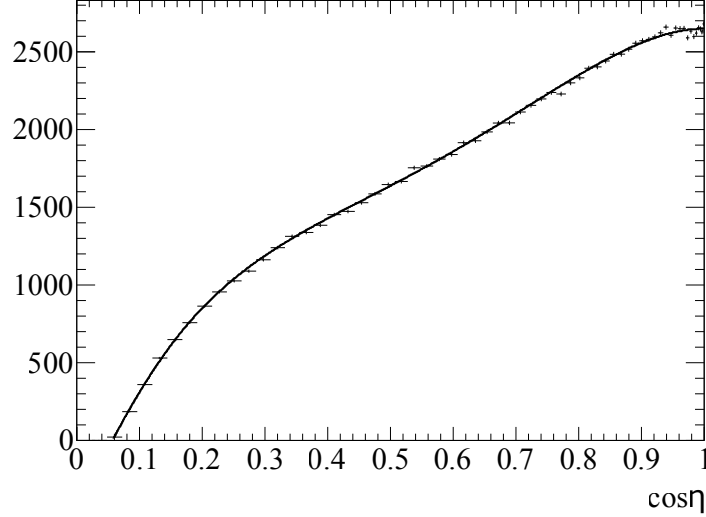


Figure 6.8: PMT angular acceptance as a function of $\cos \eta$ obtained from SKDETSIM. The vertical axis is in arbitrary unit. The solid line shows a fitted polynomial function, and it is normalized to be 1 at $\eta = 0$. Taken from [97].

the predicted charge calculation and its normalization condition is $\epsilon(\eta = 0) = 1$.

Finally, the indirect light caused by light scattering and reflection by detector components should be considered. This contribution is taken into account in $A(s)$ as,

$$A(s) = A(x_{\text{PMT}}, z_{\text{VTX}}, R_{\text{VTX}}, \varphi, \theta, \phi) \equiv \frac{d\mu^{\text{sct}}}{d\mu^{\text{iso,dir}}}. \quad (6.16)$$

$\mu^{\text{iso,dir}}$ is the predicted charge from isotropic light source along with the same particle track and total light intensity as μ^{dir} , which is obtained by removing $A(s)$ from Equation 6.12 and defining $\rho(p, s)$ as follows.

$$\rho(p, s) \equiv \int g(p, s, \cos \theta) d\Omega \quad (6.17)$$

In the indirect light evaluation, we assume that the Cherenkov angle does not depend on momentum and is fixed at the value of $\beta = 1$. By taking the ratio in Equation 6.16, the momentum dependence is factored out and then $A(s)$ becomes purely a function of geometrical variables between the particle track and the PMT in concern. Since the detector is cylindrical, $A(s)$ can be described by six-parameters as shown in Figure 6.9. In order to obtain $A(s)$, we randomly generate 3 MeV/c electrons within the detector while multiple scattering is

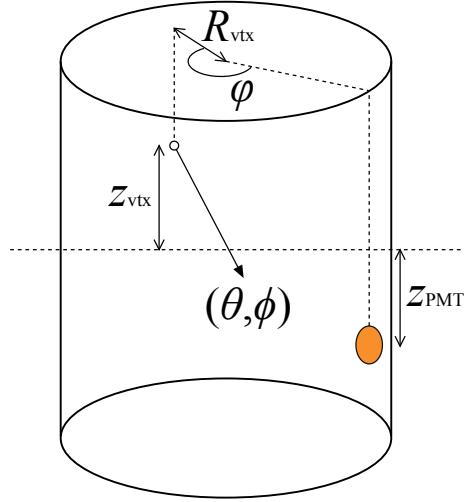


Figure 6.9: Schematic diagram of the relation between the variables for the scattering table in case of the PMTs on the barrel. For the PMTs on the top or bottom wall, x_{PMT} in Equation 6.16 is replaced to the PMT's distance R_{PMT} from the vertical axis at the center of the tank. The vertex position of the particle is shown as the white dot. Taken from [97].

turned off. Such electrons can be regarded as point light sources with $\beta = 1$. Then, six-dimensional histograms for both μ^{dir} and $\mu^{\text{iso,dir}}$ are made by counting the direct and indirect light arriving at the PMTs, respectively. At each bin in the six dimensional parameter space, the numerator $d\mu^{\text{sc}}t$ is obtained from the histogram for the indirect light, while the denominator $d\mu^{\text{iso,dir}}$ is calculated by averaging the histogram for the direct light over the particle direction. The ratio is linearly interpolated in terms of the six parameters. The scattering table $A(s)$ is thus obtained.

The integral along the particle track for the predicted charge takes too much time to calculate it. In order to avoid such a problem, we employ an approximation of the predicted charge. The photon acceptance factor $J(s)$ is defined as follows.

$$J(s) \equiv \Omega(R)T(R)\epsilon(\eta) \approx j_0 + j_1s + j_2s^2 \quad (6.18)$$

As shown in Figure 6.10, $J(s)$ is well approximated as the parabola function. The coefficients j_0 , j_1 and j_2 are determined by evaluating $J(s)$ at three points along the particle track; the initial particle position, the position at which 90 % of Cherenkov light is emitted, and their mid-position. Then, the formulation of the predicted charge for the direct light (Equation 6.11) becomes simpler after

the approximation.

$$\mu^{\text{dir}} = \Phi(p) \int ds g(s) J(s) \approx \Phi(p) (I_0 j_0 + I_1 j_1 + I_2 j_2) \quad (6.19)$$

where

$$I_n \equiv \int ds g(s) s^n. \quad (6.20)$$

I_n is obtained as a function of three parameters; p , R and θ . After integrating Equation 6.20 at discrete those three parameter bins, I_n is fitted as a function of p at each R , θ bin for smoothing the likelihood surface. Finally, I_n is linearly interpolated in terms of R and θ . In a similar manner to the predicted charge of the direct light, an approximation is introduced for that of the indirect light as follows.

$$J(s)A(s) \approx k_0 + k_1 s + k_2 s^2. \quad (6.21)$$

The predicted charge for the indirect light in Equation 6.12 reduces as follows.

$$\mu^{\text{sct}} = \Phi(p) \int ds \frac{1}{4\pi} \rho(s) J(s) A(s) = \Phi(p) \frac{1}{4\pi} (k_0 + K_1 k_1 + K_2 k_2), \quad (6.22)$$

where

$$K_n \equiv \int ds \rho(s) s^n. \quad (6.23)$$

Because K_n is a function of p only, it is fitted as a function of p for smoothing the likelihood surface. The coefficients k_n are determined in the same way as j_n .

Unhit Probability

Photoelectron counting by PMTs obeys a Poisson distribution with mean μ calculated as the predicted charge. Thus, the probability of no photoelectron is given as $e^{-\mu}$. Due to the threshold of the PMT signal, there are possibilities that a photoelectron does not surpass the threshold and make a hit. Correcting up to the third order of μ for such threshold effect, the unhit probability is estimated as;

$$P(\text{unhit}|\mu) = (1 + a_1 \mu + a_2 \mu^2 + a_3 \mu^3) e^{-\mu} \quad (6.24)$$

where the coefficients a_n are obtained from SKDETSIM. Figure 6.11 shows a good agreement between Equation 6.24 and the true values taken from SKDETSIM.

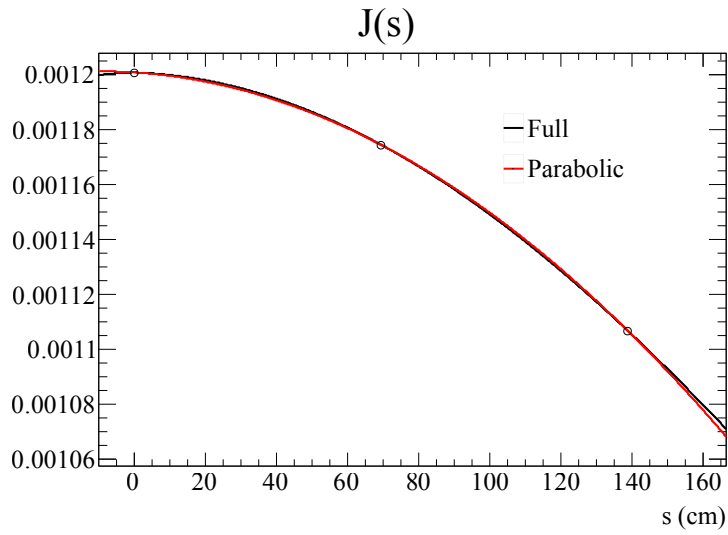


Figure 6.10: Photon acceptance factors as a function of s for the initial conditions $R = 500$ cm, $\theta = 90^\circ$, $\eta = 0^\circ$. The black and red lines correspond to $J(s)$ and the parabola function ($j_0 + j_1s + j_2s^2$), respectively. The coefficients j_n are determined by evaluating $J(s)$ at the three points indicated by the circles. $J(s)$ can be well-reproduced by the parabola function. Taken from [97].

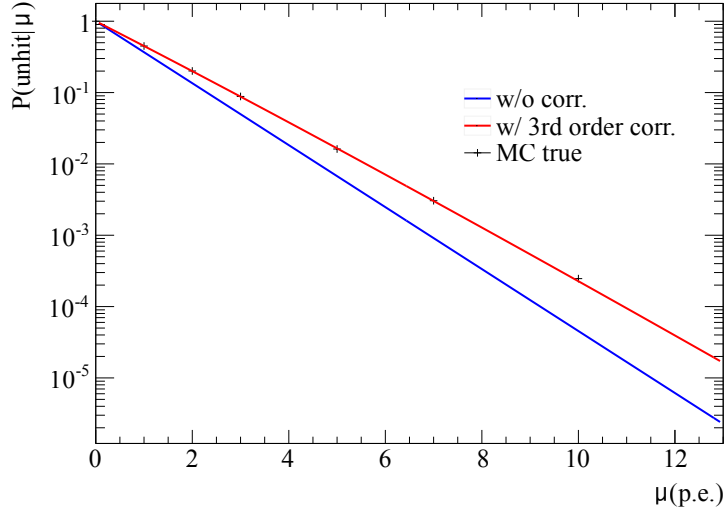


Figure 6.11: Unhit probabilities as a function of the predicted charge. The dots indicate the values taken from SKDETSIM. The red and blue lines are for with and without the 3rd order correction of the PMT threshold effect, respectively. The corrected function reproduces the MC true values. Taken from [97].

Charge Likelihood

The charge likelihood $f_q(q|\mu)$ is the probability to observe the charge q of the PMT when its predicted charge is μ . In order to obtain $f_q(q|\mu)$, normalized observed charge distributions are prepared by generating photoelectrons obeying a Poisson distribution with discrete values of μ at the PMTs in SKDETSIM as shown in Figure 6.12. Then, those distributions are fitted by a polynomial as a function of μ at each fixed value of q . The final polynomial is obtained after a linear interpolation of the fit parameters in terms of the observed charge q .

Time Likelihood

The time likelihood $f_t(t_i|\mathbf{x})$ depends on the event hypothesis \mathbf{x} and the position of the PMT. However, it is impractical to completely consider such complex dependencies. In order to approximate $f_t(t_i|\mathbf{x})$, we assume all Cherenkov photons are emitted at the midpoint of the particle track, and then the time likelihood can be expressed by the residual hit time given as,

$$t_i^{\text{res}} = t_i - t - s_{\text{mid}}/c - |\mathbf{R}_{\text{PMT}}^i - \mathbf{x} - s_{\text{mid}}\mathbf{d}|/(c/n) \quad (6.25)$$

where t_i , $\mathbf{R}_{\text{PMT}}^i$ are the raw hit time and position of the i -th PMT, \mathbf{x} , t are the vertex position and time, \mathbf{d} is the particle direction and s_{mid} is the half of the

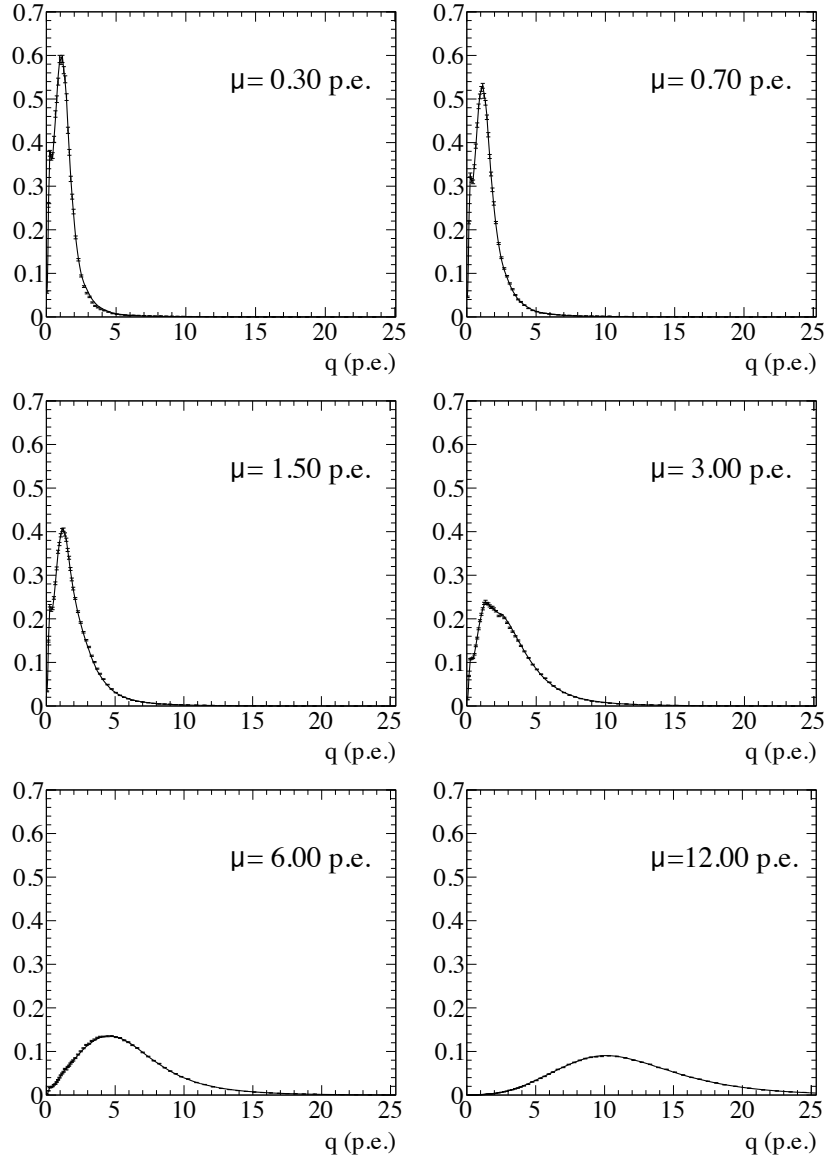


Figure 6.12: Normalized charge likelihoods as a function of observed charge at various predicted charges. The dots are taken from SKDETSIM and are well-fitted by the fitted function indicated by the solid line. Taken from [97].

particle track length. By using t_i^{res} , time likelihoods for the direct and indirect light are calculated, and the final likelihood is obtained by merging those two likelihoods as described below.

For the direct light, we impose the assumption that the time likelihood $f_t^{\text{dir}}(t^{\text{res}})$ follows a Gaussian and its parameters depend only on μ^{dir} and p . The width of the residual time distribution decreases when arriving photons increase since a hit is recorded by the first photon arriving at a PMT. That width becomes wider for a long track event since the assumption in Equation 6.25 becomes less accurate. In order to obtain the t^{res} distribution, particles are generated at various fixed momenta in SKDETSIM. At each momentum, the two dimensional histogram of $t^{\text{res}} - \log \mu^{\text{dir}}$ is filled for every hit caused by a direct photon. Then, the mean and σ of the t^{res} distribution are obtained by fitting a Gaussian at each $\log \mu^{\text{dir}}$. After smoothing those two parameters in terms of $\log \mu^{\text{dir}}$ and p , the final $f_t^{\text{dir}}(t^{\text{res}})$ is obtained. Figure 6.13 and 6.14 show the $f_t^{\text{dir}}(t^{\text{res}})$ distributions for electrons and muons, respectively.

In contrast to the direct light time likelihood, we do not assume any dependence of μ^{sct} and p for the indirect light time likelihood, and it is defined as an empirical function given by,

$$f_t^{\text{sct}}(t_i^{\text{res}}) = 1 / \left(\sqrt{\frac{\pi}{2}} \sigma + 2\gamma \right) \times \begin{cases} \exp(\tau^2/2\sigma^2) & (\tau < 0) \\ (\tau/\gamma + 1) \exp(-\tau/\gamma) & (\tau > 0) \end{cases}, \quad (6.26)$$

where $\tau = t_i^{\text{res}} - 5$ ns, $\sigma = 8$ ns and $\gamma = 25$ ns. In order to reproduce the effect of reflected light, this function has a long tail on the right side.

In order to obtain the total time likelihood for a single particle hypothesis, the direct and indirect light time likelihoods should be merged assuming that a hit is produced by an indirect photon if there is no direct photon, which is given as,

$$f_t(t_i^{\text{res}}) = \omega f_t^{\text{dir}}(t_i^{\text{res}}) + (1 - \omega) f_t^{\text{sct}}(t_i^{\text{res}}), \quad (6.27)$$

where

$$\omega \equiv \frac{1 - e^{-\mu_i^{\text{dir}}}}{1 - e^{-\mu_i^{\text{dir}}} e^{-\mu_i^{\text{sct}}}}. \quad (6.28)$$

For a multi-particle hypothesis, it is possible to extend Equation 6.27. At first, t_i^{res} 's of each particle hypothesis are calculated separately. Then, these particles are ordered by t_i^{res} . The total time likelihood for a multi-particle hypothesis is defined as follows.

$$\begin{aligned} f_t(t_i^{\text{res}}) &= \frac{1}{1 - \prod_{j=1}^{\text{all}} e^{-(\mu_{i,j}^{\text{dir}} + \mu_{i,j}^{\text{sct}})}} \\ &\times \sum_{j=1}^{\text{all}} \left[\left(\prod_{k=1}^{j-1} e^{-\mu_{i,k}^{\text{dir}}} \right) (1 - e^{-\mu_{i,j}^{\text{dir}}}) f_{t,j}^{\text{dir}}(t_i^{\text{res}}) \right. \\ &\left. + \left(\prod_{k=1}^{\text{all}} e^{-\mu_{i,k}^{\text{dir}}} \right) \left(\prod_{k=1}^{j-1} e^{-\mu_{i,k}^{\text{sct}}} \right) (1 - e^{-\mu_{i,j}^{\text{sct}}}) f_{t,j}^{\text{sct}}(t_i^{\text{res}}) \right] \end{aligned} \quad (6.29)$$

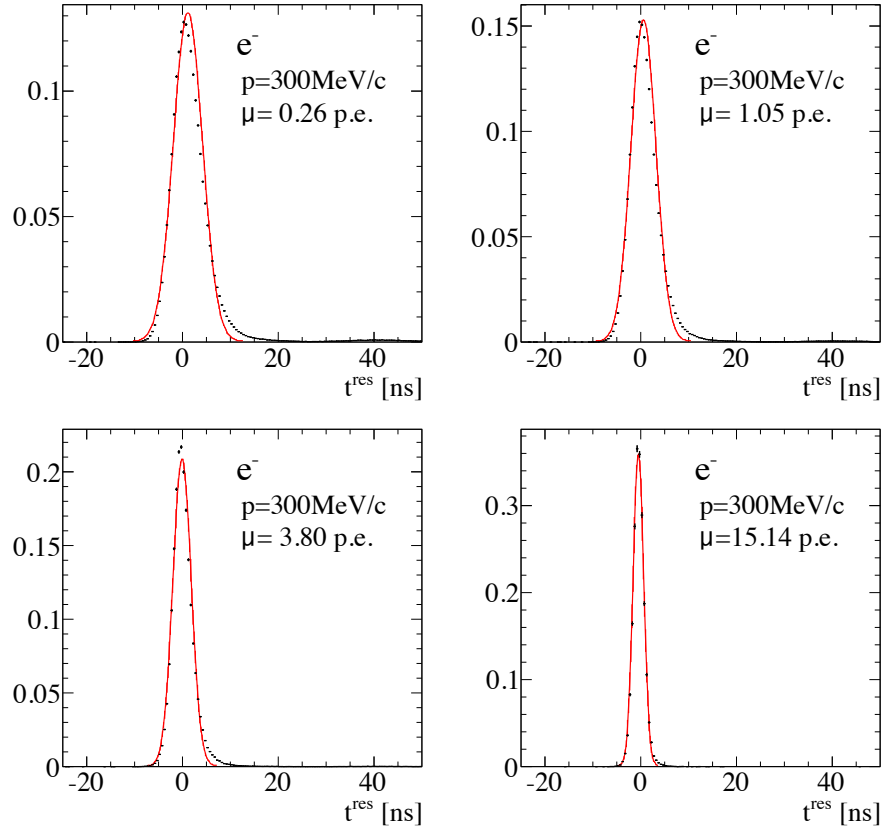


Figure 6.13: Normalized direct light time likelihoods for 300 MeV/c electrons as a function of the residual time at various predicted charges for the direct light. The dots are taken from SKDETSIM. The red curves are the Gaussian function parameterized by μ^{dir} and p . Taken from [97].

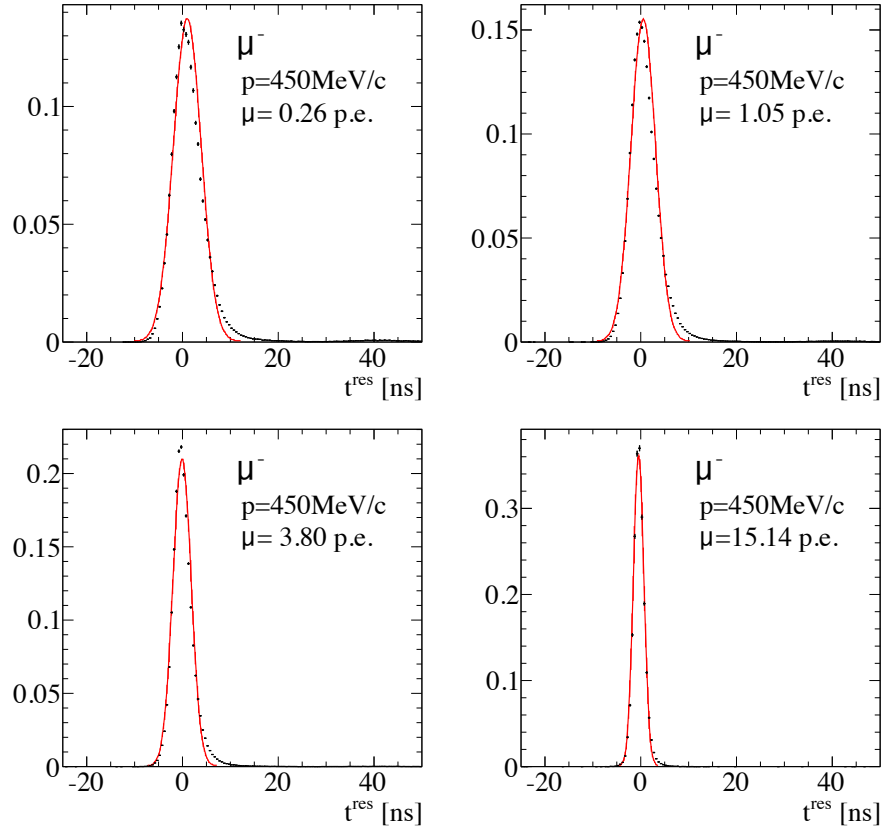


Figure 6.14: Normalized direct light time likelihoods for 450 MeV/c muons as a function of the residual time at various predicted charges for the direct light. The dots are taken from SKDETSIM. The red curves are the Gaussian function parameterized by μ^{dir} and p . Taken from [97].

6.3.2 Vertex Pre-fitter

The minimization of $-\ln L(\mathbf{x})$ starts with a single vertex position as an initial seed in order to avoid stack at a local minimum. For that purpose, the vertex pre-fitter is firstly performed in the likelihood calculation by assuming a point light source, which is estimated by maximizing the following goodness function.

$$G(\mathbf{x}, t) = \sum_i^{\text{hit}} \exp(-(T_{\text{res}}^i/\sigma)^2/2), \quad (6.30)$$

where

$$T_{\text{res}}^i = t_i - t - |\mathbf{R}_{\text{PMT}}^i - \mathbf{x}|/(c/n). \quad (6.31)$$

T_{res}^i is the residual hit time of the i -th PMT. A coarse grid scan in the space of $\{\mathbf{x}, t\}$ is iteratively done for the goodness while shrinking the grid size and σ . After the grid scan, the final seed vertex is obtained by minimizing of $-G(\mathbf{x}, t)$ with $\sigma = 4$ ns.

6.3.3 Hit Clustering

Since the time window for an event is order $10 \mu\text{s}$ around an event trigger, there might be multiple hit clusters. For example, a Michel electron produced by a muon as a primary event are counted as “subevent” since their time interval is enough long, typically $2 \mu\text{s}$. The hit clustering algorithm is thus performed before going to the maximum likelihood reconstruction.

First, the goodness $G(\mathbf{x}, t)$ discussed in Equation (6.30) is evaluated every 8 ns step with an optimized σ ($=6.3$ ns) while fixing the vertex position given by the vertex pre-fitter. The evaluation is started at ~ 300 ns before the trigger using all hits in the time window between -200 ns and $15,000$ ns around the trigger. An example of the goodness distribution as a function of t for an event with a parent muon and a Michel electron shown in Figure 6.15. The goodness peak is identified by using a goodness threshold curve function. Two peaks in Figure 6.15 are consistent with true particle times.

After the peaks are searched, a time window is set around each peak, containing the hits belong to the peak. The hits outside the time window are considered as unhit in the likelihood calculation. The residual time is re-evaluated for the peak time, and then the time window is defined as $-180 \text{ ns} < T_{\text{res}}^i < 800 \text{ ns}$. If time windows are overlapped, they are merged into a single window.

Finally, the vertex pre-fitter and the peak search are conducted again for a precise peak finding. The final time windows are fixed for each remaining peak, and the maximum likelihood reconstruction is done in each of them. Peak detection efficiencies of Michel electrons from sub-GeV stopping muons for the data and MC are $88.41 \pm 0.08\%$ and $87.81 \pm 0.15\%$, respectively.

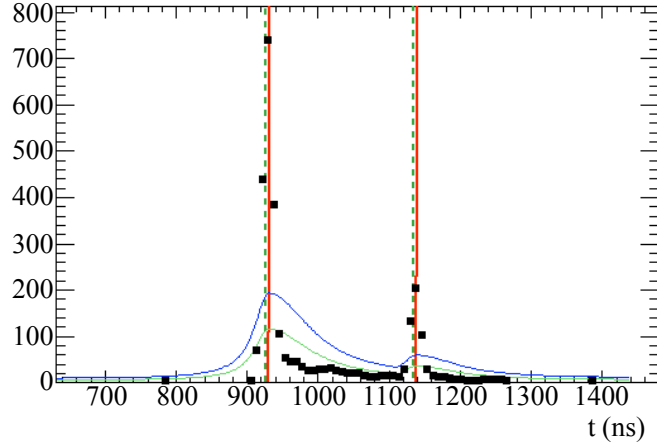


Figure 6.15: Goodness distribution as a function of hit time for an event with a parent muon and a Michel electron. The dots show the scanned goodness points. The blue and green curves are the goodness threshold functions which are used to determine the event time indicated by the red lines. The green dotted lines are for the true time for each particle. Taken from [97].

6.3.4 Single-Ring Fitter

For each subevent described in Section 6.3.3, the single-ring fitter is performed by maximizing the likelihood under a single particle hypothesis. There are three particle hypotheses which fitQun can handle: e , μ and π^+ . The single-ring fitter for e and μ hypotheses reconstructs seven parameters $\{\mathbf{x}, t, \theta, \phi, p\}$. In addition to these parameters, the energy loss parameter E_{loss} is fitted for π^+ hypothesis.

For the subevent which has multiple event peaks in the time window described above, the single-ring fitters are performed on each peak using all the hits related to each peak without overlapping. The hits for the peak after the primary one are selected in a range of $-30 \text{ ns} < T_{\text{res}}^i < 60 \text{ ns}$ where T_{res}^i is the residual time calculated for the peak. The single-ring fitters are performed using those hits while the other hits are regarded as unhits. For the primary peak, the hits which are not selected by the other peaks are used to the fit.

First of all, the single electron fitter is conducted. As for the initial values of the vertex $\{\mathbf{x}, t\}$ to the fit, the results of the vertex pre-fitter are used. While fixing the vertex and the momentum estimated by the total observed charge, the initial value of the direction $\{\theta, \phi\}$ is set by scanning the likelihood at 400 points of the direction which are equally spaced on the unit sphere. The initial value of the momentum p is determined by another likelihood scanning fixing the other parameters. Using these initial seven values and electron hypothesis, the single electron track parameters are then simultaneously fitted by minimizing $-\ln L$.

Next, the single muon fitter is performed. By using the fitted track parameters of the single electron fitter except the momentum, the initial value of the momentum is obtained by a likelihood scan. After that, the simultaneous minimization of $-\ln L$ is done assuming muon hypothesis.

The last single-ring fitter is for the π^+ hypothesis. Since the mass of π^+ s is similar to that of muons, π^+ s usually have similar Cherenkov emission profiles of muons. However, a π^+ can interact hadronically with the nuclei in water, and then change its direction or be absorbed. In such a case, a π^+ produces two rings; the ring before the hadron interaction is called the “upstream-track” ring and the other ring after that is called the “downstream-track” ring. The single π^+ fitter reconstructs this upstream-track ring using the single muon fit result as a seed. The predicted charge of the upstream-track is obtained by subtracting the predicted charge of the downstream-track from the predicted charge of an imaginary full track without any hadron interaction. Here, the additional fit parameter E_{loss} is introduced which is defined as the kinetic energy deposit in the upstream-track. Using E_{loss} , the vertex of the downstream-track is calculated by assuming constant kinetic energy loss per unit track length. For the time likelihood, the residual time in Equation 6.25 is estimated using the midpoint of the upstream-track. All eight parameters of the upstream-track are simultaneously fitted by minimizing of $-\ln L$.

By taking the ratio of resulting log likelihoods, the particle type of the sing-ring can be identified. Figure 6.16 shows $\ln(L_e/L_\mu)$ as a function of the reconstructed momentum for the single electron fit in the FC true-fiducial ν_e and ν_μ CCQE in the atmospheric neutrino MC. Both $\ln(L_e/L_\mu)$ for ν_e and ν_μ have the opposite dependence on the momentum. Therefore, electron events are separated by the following cut which is decided by taking into account the misidentification rate for both electrons and muons.

$$\ln(L_e/L_\mu) > -10. \quad (6.32)$$

Although we do not distinguish π^+ and μ in this analysis, it is worth to look at $\ln(L_{\pi^+}/L_\mu)$ as a function of E_{loss} in the T2K accelerator neutrino MC as shown in Figure 6.17. The separation is not clear compared to $\ln(L_e/L_\mu)$, but some fraction of π^+ events can be distinguished from muons by making a threshold line. In the left figure, $\ln(L_{\pi^+}/L_\mu)$ is distributed near zero, which means that muons are fitted almost equally well by the μ and π^+ hypotheses. Since both μ and π^+ have similar Cherenkov emission profiles, muon rings are fitted well by the upstream-track π^+ hypothesis while increasing E_{loss} to the point where the momentum at the assumed upstream-track point drops below the Cherenkov threshold.

Examples of the data-MC agreement related to the PID likelihood for the FC sub-GeV single-ring and multi-ring sample in SK-IV are shown in Figure 6.18. Our atmospheric neutrino MC agrees well with the data regarding PID performance. The mis-PID rate in single-ring events is evaluated by using the stopping muon sample described in Section 6.6. As shown in Figure 6.19, the mis-PID rates for both muons and electrons in the data (MC) are $0.10 \pm 0.03\%$ ($0.15 \pm 0.03\%$) and $0.61 \pm 0.08\%$ ($0.48 \pm 0.04\%$), respectively.

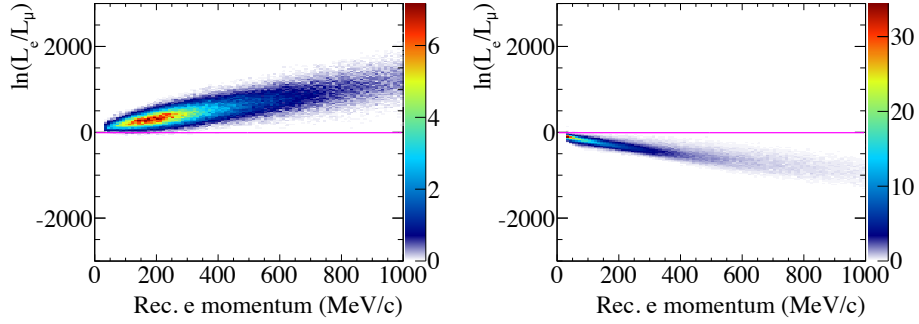


Figure 6.16: Log likelihood ratio $\ln(L_e/L_\mu)$ as a function of the reconstructed momentum of the sing-ring electron fit for the FC true-fiducial ν_e (ν_μ) CCQE in the atmospheric neutrino MC on the left (right) figure. The magenta lines are the cut criteria for the e/μ separation. Taken from [97].

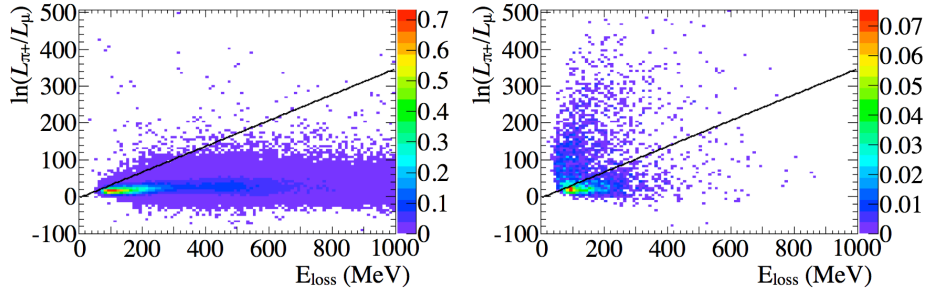


Figure 6.17: Log likelihood ratio $\ln(L_{\pi^+}/L_\mu)$ as a function of the energy loss for the FC true-fiducial ν_μ CCQE (NC π^+) in the T2K accelerator neutrino MC on the left (right) figure. The black lines are the cut criteria for the μ/π^+ separation. Taken from [97].

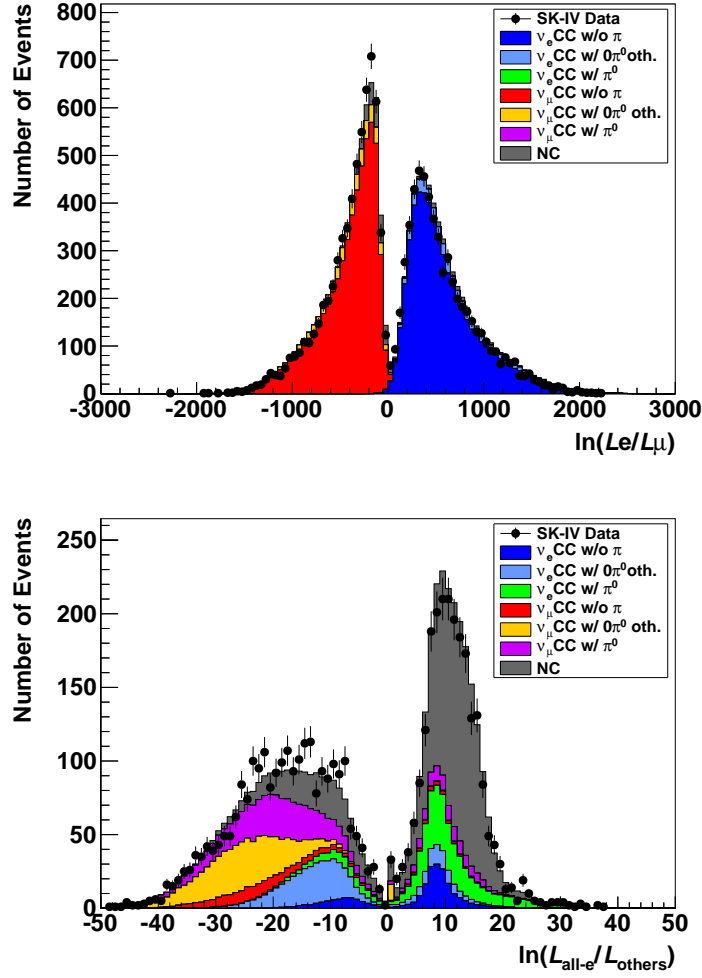


Figure 6.18: PID likelihood distributions for the FC sub-GeV single-ring (top) and multi-ring (bottom) sample of the data (black points) and the atmospheric neutrino MC (stacked histograms) in SK-IV. Here, the events whose reconstructed vertices are within the region 1.5 m inside from the nearest wall are selected. In the top figure, the events in the above (below) -10 are identified as electron- (muon-) like events. The horizontal axis in the bottom figure is for the likelihood ratio between an all e-like hypothesis and the best fit among other hypotheses for two or three ring events.

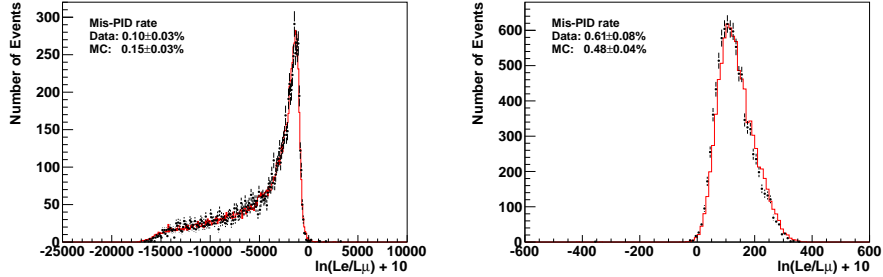


Figure 6.19: Distributions of the log likelihood ratio $\ln(L_e/L_\mu) + 10$ for both muons (left) and electrons (right) in the stopping muon sample of the data (black points) and the MC (red histogram).

6.3.5 Multi-Ring Fitter

The reconstruction of multi-particle events is crucial for proton decay and atmospheric neutrino analyses. `FitQun` searches up to six rings only in the first subevent since subsequent subevents usually do not contain multi-particles.

The ring counting of `fitQun` is conducted in a brute force way as shown in Figure 6.20. Electrons and gamma-rays are reconstructed as the electron ring, and muons and π^+ s are reconstructed as the upstream-track π^+ ring since they can be fitted by the π^+ hypothesis. In this figure, the single electron fit result is used as the first ring and the brute force ring search is done, but this search is also repeated for the single upstream-track π^+ fit. First of all, the direction of an additional second ring is roughly evaluated by scanning the likelihood at 400 points of the direction, assuming the same vertex of the single-ring fit result and the second ring momentum is assumed to be 50 MeV/c. Then, the second ring momentum is fitted by minimizing $-\ln L$ while all the other parameters are fixed. After that, the direction and the momentum of the second ring are simultaneously fitted fixing all the other parameters. When there are additional rings in an event, the momentum of the single ring fit tends to be overestimated due to the existence of the charge from the other rings. Therefore, the simultaneous fit of the momenta of the two rings is performed while all the other parameters are fixed. Finally, all the parameters of the two rings including the common vertex are then fitted simultaneously. In the case of the π^+ ring, E_{loss} is also fitted simultaneously with the other parameters.

In order to check whether the new ring is true ring or fake ring, the log likelihood ratio of the single-ring fit to the better of the two-ring fit, $\ln(L_{2\text{Rex}}/L_{1\text{Re}})$ is evaluated. Figure 6.21 shows the square root of $\ln(L_{2\text{Rex}}/L_{1\text{Re}})$ distribution for FC sub-GeV atmospheric neutrino MC events with no Michel electrons. True single electron events such as ν_e CC events are concentrated to a lower region while multi-ring events such as NC events have higher values. The new ring which passed the following criterion is identified as the true ring.

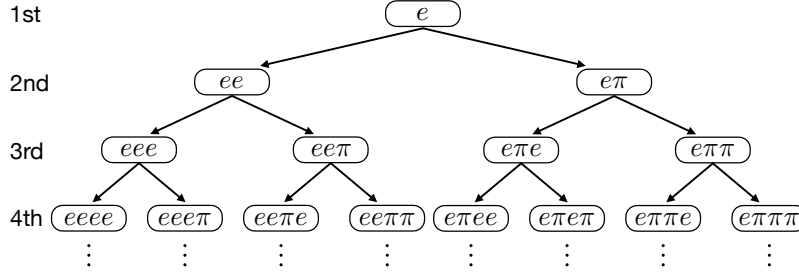


Figure 6.20: Schematic diagram of the ring finding in the multi-ring fitter. The fifth and the sixth ring are assumed to be electrons. In this diagram, the first ring is assuming an electron ring. The same procedure is repeated for the case of assuming π^+ as the first ring.

- $\ln(L_{2R}/L_{1R}) > 87.5$, if the second ring is the electron-ring.

or,

- $\ln(L_{2R}/L_{1R}) > 140$, if the second ring is the π^+ -ring.

For the $(n + 1)$ -th ring, the criterion becomes as,

- $\ln(L_{(n+1)R}/L_{nR}) > 70$.

Following the second ring search, additional ring search is repeated until either a fake ring is found or up to six rings in a similar manner. But, in order to save computation time, the fifth and the sixth ring are fitted by the electron hypothesis only, and the simultaneous fit of all rings is conducted only for the momentum of them after the two-ring fit. Figure 6.21 also shows the square root of $\ln(L_{3R_{\text{reex}}}/L_{2R_{\text{ee}}})$ distribution for FC sub-GeV atmospheric neutrino MC events with no Michel electrons. It can be seen that both ν_e CC with π^0 events and NC events are dominant interaction modes above the threshold. The multi-ring hypothesis with the smallest $-\ln L$ is used in a further precise fit as the “seeding multi-ring hypothesis”.

Once the seeding multi-ring hypothesis is obtained, the rings in that hypothesis are reordered by the visible energy. For the most energetic ring, if the angle between the ring and a lower energy ring is smaller than 20° , they are merged into a single ring by adding the visible energy. This angle threshold is decided to reduce an over ring-counting seen in $p \rightarrow e^+\pi^0$ analysis at the development stage as shown in Figure 6.22. Figure 6.23 shows the number of rings distributions for free proton events in the $p \rightarrow e^+\pi^0$ analysis before and after the ring correction change. After the ring merge procedure, the most energetic ring is fitted including the vertex by three particle hypotheses (e , μ , π^+) while the other rings are fixed. Then, the ring type of the most energetic ring is

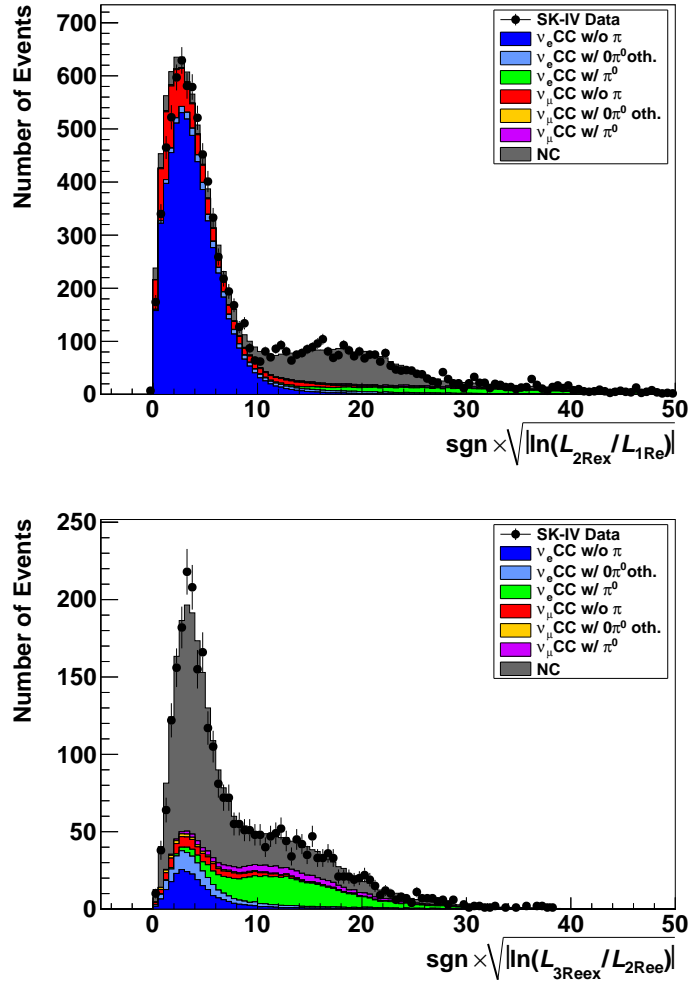


Figure 6.21: Square root of $\ln(L_{2\text{Rex}}/L_{1\text{Re}})$ (top) and $\ln(L_{3\text{Reex}}/L_{2\text{Ree}})$ (bottom) distributions for the FC sub-GeV sample without tagged Michel electrons. The dots show the SK-IV data. Stacked histograms are the atmospheric neutrino MC, which are categorized by final states. The events whose reconstructed vertices are within the region 1.5 m inside from the nearest wall are selected.

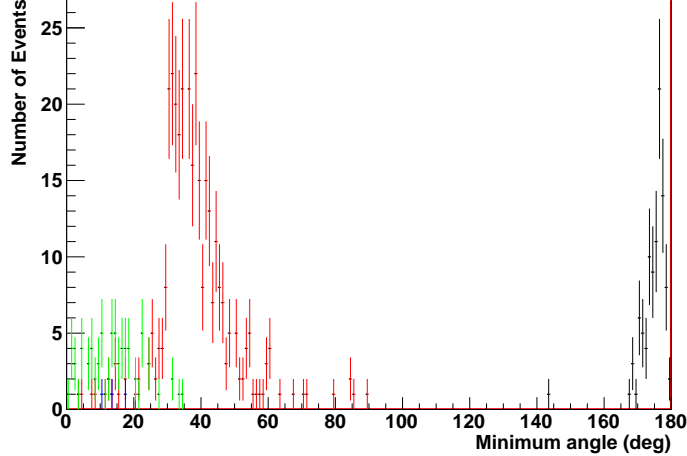


Figure 6.22: Minimum opening angle between each ring only for free proton events in the $p \rightarrow e^+\pi^0$ MC. The black, red, green and blue histograms correspond to 2, 3, 4 and 5-ring events, respectively. By introducing the opening angle cut at 20° , we can merge the fake rings.

determined whether it is a showering (e and γ) or a non-showering (μ and π^+) ring. If the following criterion is satisfied for the ring, then it is marked as a shower ring and the original hypothesis is replaced by the selected hypothesis.

$$\ln(L_e/L_{\pi^+}) > -10. \quad (6.33)$$

The simultaneous fit and particle identification procedures as above are sequentially performed for all the remaining rings in the descending order of the visible energy.

In the multi-ring fitter, the e/π^+ separation is only used. However, in the case of the ring is judged as a non-showering ring, the ring is always assumed to be a muon if it is the most energetic ring, whereas it is always assumed to be a π^+ if it is a lower energy ring. Because ν_μ CC events usually have a muon as the most energetic ring and NC events rarely have a π^+ as the most energetic ring.

The final fit result obtained as above is used in this analysis.

6.4 Performance in MC Simulation: APfit vs. fitQun

In this section, the SK-IV MC based performances of both APfit and fitQun are shown. Here, we use the FC true-fiducial CCQE single electron and muon

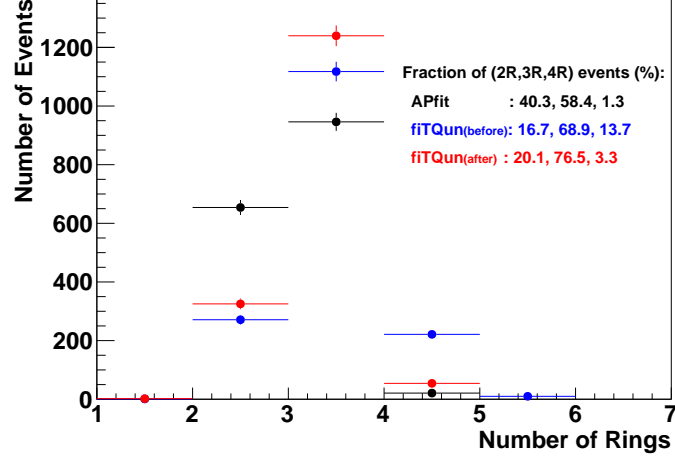


Figure 6.23: Number of rings distributions for free proton events in the $p \rightarrow e^+\pi^0$ MC. The black histogram shows the APfit result and the blue (red) histogram shows the fitQun result before (after) the ring correction change.

events in the atmospheric neutrino MC for Figure 6.24-6.29. The fiducial volume for APfit is defined as the region 2 m inside from the wall while we show the fitQun performance in two different fiducial volume definitions; 1.5 m and 2 m.

Figure 6.24 shows the distributions of the distance between the reconstructed and true vertices. The vertex resolutions defined at 1σ deviation position for single electron (muon) events are; 20.1 (19.3) cm for the best single ring fit of fitQun and 29.4 (22.7) cm for APfit. The momentum dependencies of the vertex resolution are shown in Figure 6.25.

The angle between the reconstructed and true directions, and their momentum dependencies are also shown in Figure 6.26 and 6.27. For single electron and muon events, the direction resolutions defined at an 1σ deviation angle are 2.81° (2.91°) and 1.73° (1.75°) for the best single ring fit of fitQun (APfit).

In order to evaluate the momentum resolution, the fractional difference between the reconstructed and true momenta is fitted by a Gaussian at each true momentum bin, and taking the sigma of the fitted Gaussian as the resolution. Figure 6.28 shows the momentum resolution as a function of the true momentum.

For the particle identification, the misidentification rates as a function of the true momentum are shown in Figure 6.29. Compared to APfit, the best single ring fit of fitQun has smaller misidentification rates and they are below 1%.

As discussed in Chapter 7, the most dominant background for $p \rightarrow e^+\pi^0$ is ν_e CC events accompanied with a single π^0 in final state (ν_e CC $1\pi^0$). As an example of the ring counting and PID performance, Figure 6.30 shows the

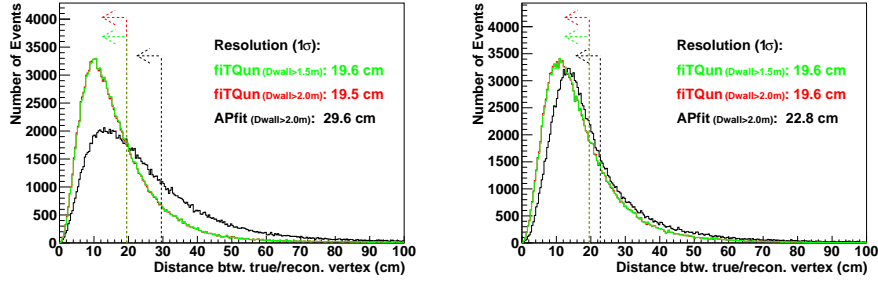


Figure 6.24: Distributions of the distance between the true and reconstructed vertex of FC true-fiducial CCQE single electron (left) and muon (right) events in the atmospheric neutrino MC. The green (red) histogram is for the best single ring fit of fitQun with the $D_{\text{wall}} > 1.5$ (2.0) m cut and black histogram is for APfit with the $D_{\text{wall}} > 2.0$ m cut. The dotted lines show the vertex resolution which is defined as 1σ deviation point.

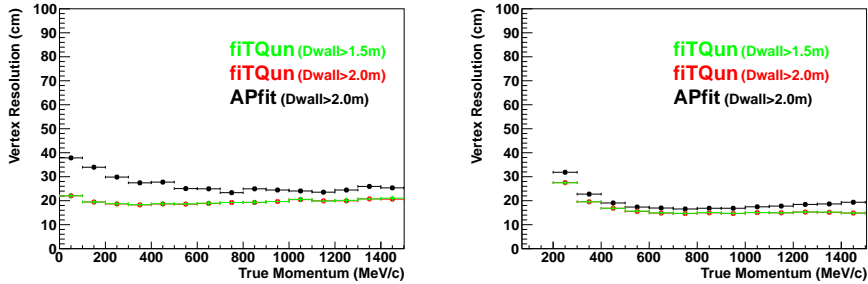


Figure 6.25: Vertex resolution as a function of true momentum of FC true-fiducial CCQE single electron (left) and muon (right) events in the atmospheric neutrino MC. The green (red) points are for the best single ring fit of fitQun with the $D_{\text{wall}} > 1.5$ (2.0) m cut and black points are for APfit with the $D_{\text{wall}} > 2.0$ m cut.

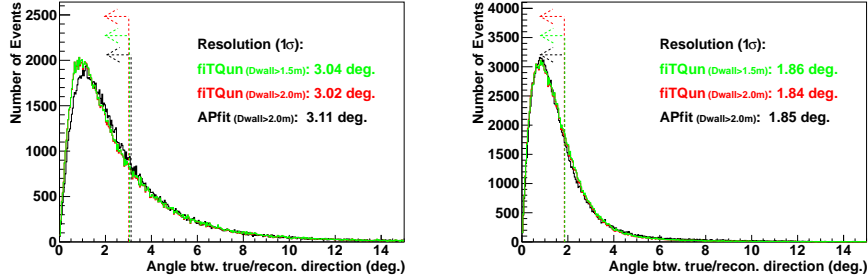


Figure 6.26: Distributions of the angle between the true and reconstructed direction of FC true-fiducial CCQE single electron (left) and muon (right) events in the atmospheric neutrino MC. The green (red) histogram is for the best single ring fit of fitTQun with the $D_{\text{wall}} > 1.5$ (2.0) m cut and the black histogram is for APfit with the $D_{\text{wall}} > 2.0$ m cut. The dotted lines show the direction resolution which is defined as 1σ deviation point.

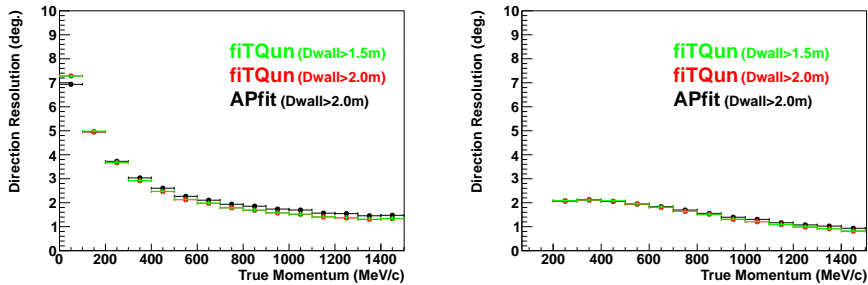


Figure 6.27: Direction resolution as a function of true momentum of FC true-fiducial CCQE single electron (left) and muon (right) events in the atmospheric neutrino MC. The green (red) points are for the best single ring fit of fitTQun with the $D_{\text{wall}} > 1.5$ (2.0) m cut and the black points are for APfit with the $D_{\text{wall}} > 2.0$ m cut.

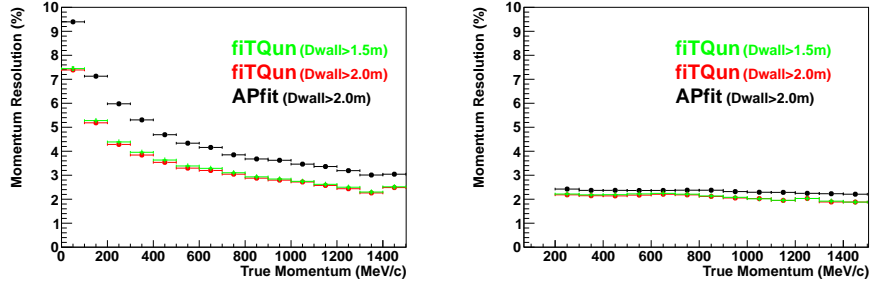


Figure 6.28: Momentum resolution as a function of true momentum for FC true-fiducial CCQE single electron (left) and muon (right) events in the atmospheric neutrino MC. The green (red) points are for the best single ring fit of fitQun with the $D_{\text{wall}} > 1.5$ (2.0) m cut and the black points are for APfit with the $D_{\text{wall}} > 2.0$ m cut.

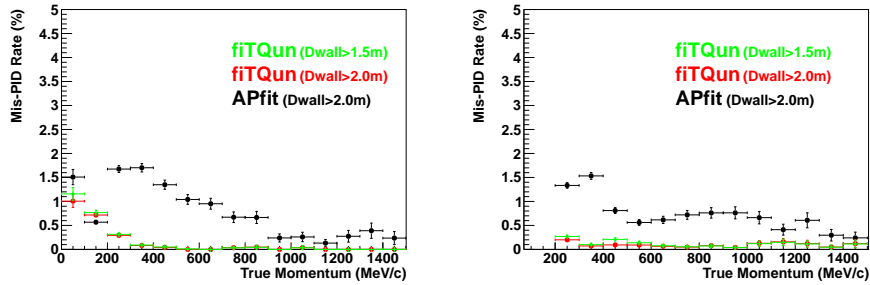


Figure 6.29: Mis-PID rate as a function of true momentum for FC true-fiducial CCQE single electron (left) and muon (right) events in the atmospheric neutrino MC. The green (red) points are for the best single ring fit of fitQun with the $D_{\text{wall}} > 1.5$ (2.0) m cut and the black points are for APfit with the $D_{\text{wall}} > 2.0$ m cut.

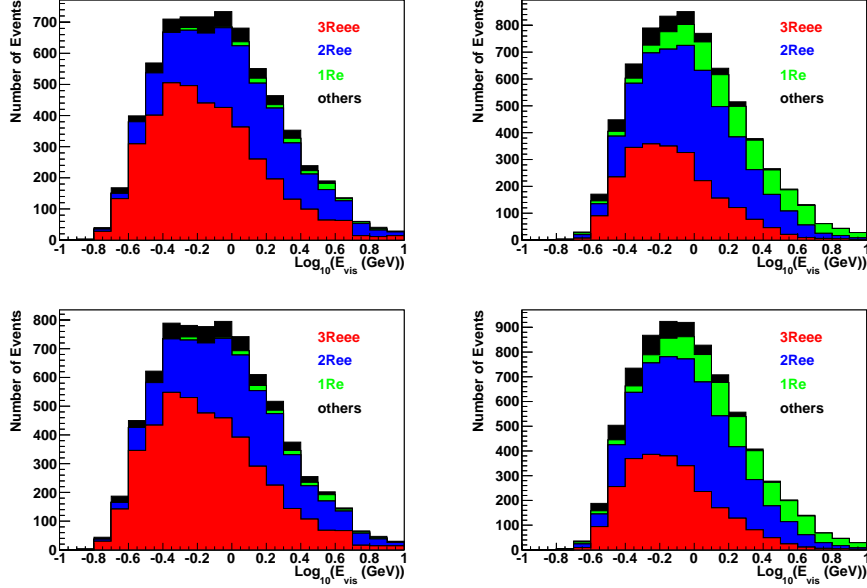


Figure 6.30: Event categories of ν_e CC single- π events with a single π^0 and no visible π^\pm in final state in the FC atmospheric neutrino MC for the best multi-ring fit of fitQun (left) and APfit (right). The top figures are for the events with the $D_{\text{wall}} > 2$ m cut. The bottom figures are for the events with the $D_{\text{wall}} > 1.5$ m cut. The horizontal axes are the log of the visible energy in GeV. The colors correspond to three e-like ring events (red), two e-like ring events (blue), single e-like ring events (green) and the other events (black), respectively.

event categories of true $\nu_e \text{CC} 1\pi^0$ events in the FC atmospheric neutrino MC. It can be seen that the fraction of three e-like ring events of the best multi-ring fit of fitQun is higher than APfit. For example, in the 1 GeV bin, the fraction of three (two) e-like ring events of fitQun ($D_{\text{wall}} > 1.5$ m) is 52.8% (38.5%) while that of APfit ($D_{\text{wall}} > 2.0$ m) is 28.7% (53.4%). Since there should be three shower rings in this neutrino mode, the fitQun ring counting gives more correct information. Figure 6.31 shows the distance between the true vertex and reconstructed vertex and the π^0 invariant mass distributions in the $\nu_e \text{CC} 1\pi^0$ sample. In the document [97], there is more discussion about other neutrino modes. As a result, it can generally be said that fitQun has a higher multi-ring fit performance than APfit.

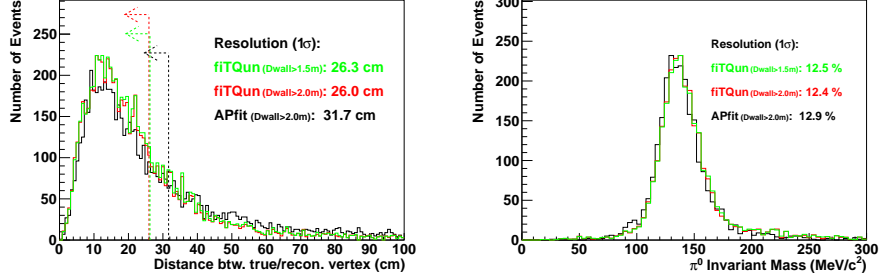


Figure 6.31: Distributions of the distance between the true and reconstructed vertex (left) and the π^0 invariant mass (right) for ν_e CC single- π events with a single π^0 and no visible π^\pm in final state in the FC atmospheric neutrino MC. The green (red) histogram is for the best multi-ring fit of fitTQun with the $D_{\text{wall}} > 1.5$ (2.0) m cut and the black histogram is for APfit with the $D_{\text{wall}} > 2.0$ m cut. The dotted lines show the vertex resolution which is defined as 1σ deviation point.

6.5 Fiducial Volume

Since fitTQun is a new fitter and has better performance compared to APfit, it is worth revisiting the definition of the fiducial volume (FV). In all the previous proton decay analyses using APfit, FV was defined as the region where the vertex distance from the nearest wall D_{wall} is greater than 2 m, which corresponds to the mass of 22.5 kton. As described in Section 7.1, fitTQun has a same level signal efficiency for $p \rightarrow e^+\pi^0$ even if the $D_{\text{wall}} > 1.5$ m cut is used, compared to that of APfit with the $D_{\text{wall}} > 2$ m cut. The fiducial volume is expanded to 24.7 kton by using the $D_{\text{wall}} > 1.5$ m cut. In order to confirm that the $D_{\text{wall}} > 1.5$ m cut is safe for fitTQun, the reconstructed vertices of several samples for both the data and MC are checked.

As for the first check, the reconstructed entering point of the stopping muon events is shown in Figure 6.32. Two peaks in the figure corresponds to the ID wall positions from the center of the tank (top wall: 1810 cm, barrel wall: 1690 cm). The peak position differences between the data and the MC for both the z and R directions are about 1 cm and their errors are $0.07 \pm 0.01\%$.

Next, D_{wall} of Michel electrons are shown in Figure 6.33. The agreement between the data and the MC at the $D_{\text{wall}} = 1.5$ m bin is consistent. From these results, we can say that the vertex of single ring events is properly reconstructed by fitTQun.

In addition to the above, the atmospheric neutrino events which have multi-rings are checked, since we use multi-ring events in this analysis. Figure 6.34 shows the reconstructed vertices of the multi-ring atmospheric neutrino events for both the z and R directions. For fitTQun, the reconstructed vertex of the most energetic ring is adopted for the determination of the vertex of the event.

The data distribution shapes are similar to the MC, and there are no strange peaks in the whole region. Thus, we can use the events which are in the $D_{\text{wall}} > 1.5$ m region.

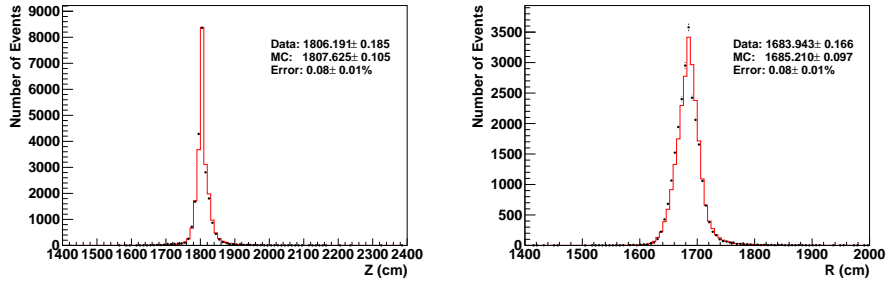


Figure 6.32: Vertex distributions of the stopping muon events of fitQun in the z and R directions for the data (black points) and the MC (red). Both of the errors of the mean value are $0.08 \pm 0.01\%$.

6.6 Energy Scale

The precise momentum determination of the data is necessary for the proton decay analysis described Chapter 7, since the total momentum and invariant mass are conclusive parameters. It is ideal to have a control data sample of the proton decay with various final states, and the energy scale is then evaluated by comparing it with the simulation. However, taking such a data is not realistic. Four well-known control samples are instead used for the energy scale: high/low energy stopping muon, Michel electron and neutral pion sample.

In this section, the absolute energy scale error, the time variation and the detector uniformity are evaluated. We discuss only about fitQun for the SK-IV detector period. The data period used for the calibration of SKDETSIM, which is April 2009, is selected for the absolute error estimation. Since the water attenuation length L^{att} is changing in time as described in Section 3.13, time dependent L^{att} corrections are applied to both APfit and fitQun.

6.6.1 High Energy Stopping Muon Sample

The high energy stopping muon events are used to check the energy scale in a range of 1 GeV to 10 GeV by taking ratios of the reconstructed momentum of muons to their track lengths (p/range), namely the energy loss dE/dx since this is approximately constant. The range is obtained from the muon entering position and the Michel electron vertex. It is expected to be independent on the momentum reconstruction, since the muon entering position is defined as the ID wall position estimated by the direction and the Michel electron vertex can be

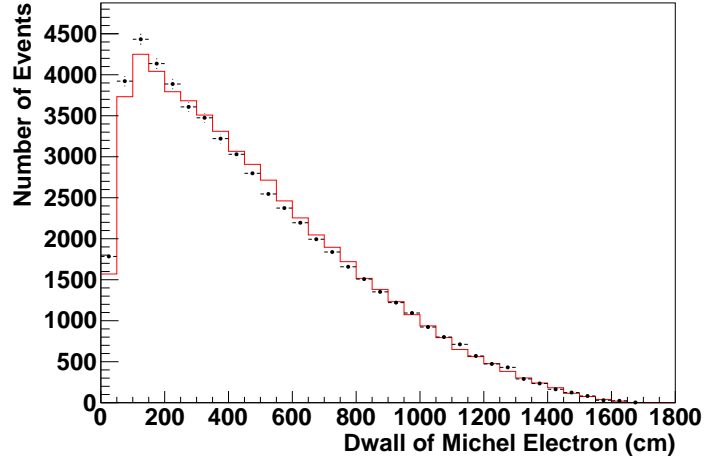


Figure 6.33: D_{wall} of Michel electron vertices of fitQun for the data (black points) and the MC (red).

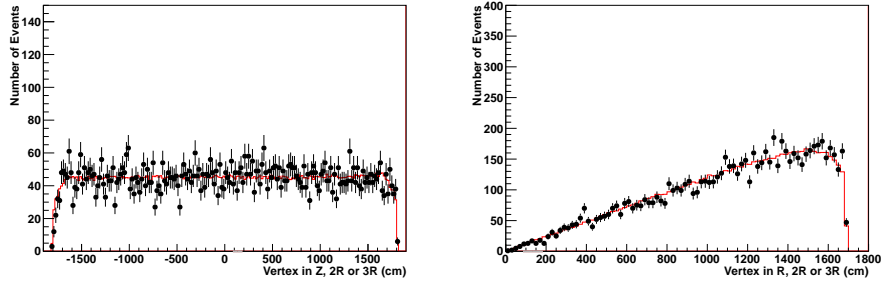


Figure 6.34: Vertex distributions of the multi-ring (2 or 3-ring) atmospheric neutrino events of fitQun in the z and R directions for the data (black points) and the MC (red).

well-reconstructed mainly by the hit time. Therefore, p/range depends almost only on the momentum. The high energy stopping muon events are selected by the following criteria:

- Total observed charge $< 70,000$ p.e.s
- Muon entering position is on the top ($z_{\text{ent}} > 15$ m and $R_{\text{ent}} < 15$ m) or barrel ($R_{\text{ent}} < 15$ m, -15 m $< z_{\text{ent}} < 15$ m) wall
- Number of Michel electrons = 1
- Decay time is within a range between $1.5 \mu\text{s}$ and $10 \mu\text{s}$
- Michel electron vertex is inside the fiducial volume

where z_{ent} and R_{ent} are the muon entering position in the vertical and radius axes. Figure 6.35 shows p/range distributions of the data and the MC between the range of 5 m and 35 m with 5 m bin for fitQun with $D_{\text{wall}} = 1.5$ m. The errors are evaluated at each bin by comparing the peak position of a fitted Gaussian of both the data and MC. All the errors are less than 1%.

6.6.2 Low Energy Stopping Muon Sample

The momentum of the stopping muons can be estimated by the Cherenkov angle θ as the following formula, since the angle largely depends on the momentum especially the low energy region below around 500 MeV/c as shown in Figure 6.36.

$$p(\theta) = \frac{m_{\mu}}{\sqrt{n^2 \cos^2(\theta) - 1}} \quad (6.34)$$

where m_{μ} is the mass of muons. However, no variable related to the Cherenkov angle is available in fitQun. Thus, the event selection is done mainly based on APfit parameters as follow.

- Total observed charge is within a range between 500 p.e.s and 5000 p.e.s
- $z_{\text{ent}} > 17.2$ m
- Direction of the entering muon in the z -direction < -0.87
- Goodness of the stopping muon fit > 0.6
- Number of Michel electrons = 1
- Decay time $\geq 1.2 \mu\text{s}$

The ratios of the reconstructed momenta $p(\text{p.e.})$ to $p(\theta)$ at several $p(\text{p.e.})$ bins are used for the error estimation. Figure 6.37 shows $p(\text{p.e.})/p(\theta)$ distributions for fitQun with $D_{\text{wall}} = 1.5$ m. The maximum error is $(-1.905 \pm 0.402)\%$.

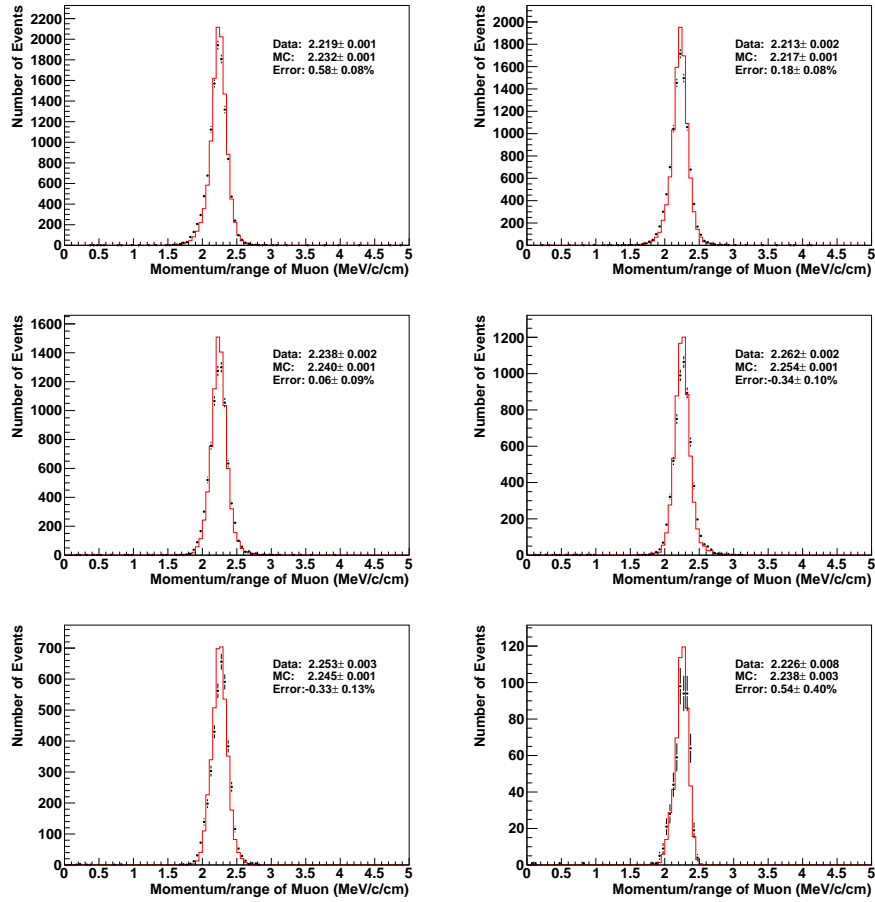


Figure 6.35: Momentum over the range of the stopping muon events with various ranges for the data (black points) and the MC (red). From the top left plot to the bottom right plot, the ranges are defined as 5-10 m, 10-15 m, 15-20 m, 20-25 m, 25-30 m and 30-35 m, respectively.

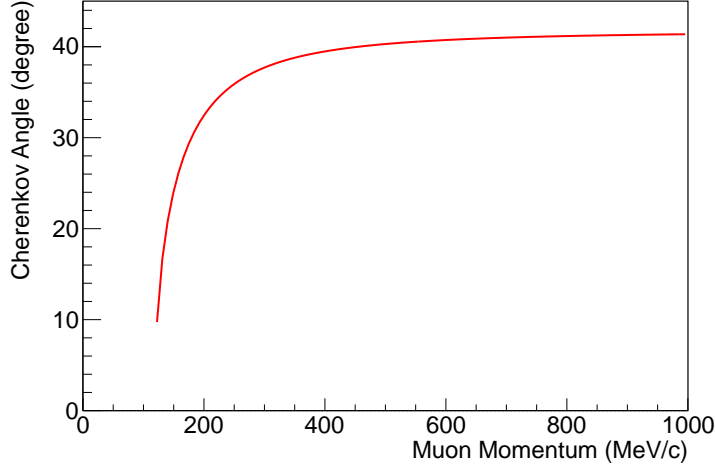


Figure 6.36: Cherenkov angle of muons as a function of their momentum ($\cos \theta = \sqrt{1 + m_\mu^2/p^2/n}$).

6.6.3 Michel Electron Energy Spectrum

The energy spectrum of Michel electrons emitted from the stopping muons is well-known and useful for the energy scale check. Figure 6.38 shows the reconstructed momentum of Michel electrons selected by the same criteria as the high energy stopping muons. The error is calculated by comparing the mean value of the spectrum for both the data and MC, and then is obtained as $(-1.80 \pm 0.16)\%$ for fitQun with $D_{\text{wall}} = 1.5$ m.

6.6.4 Neutral Pion Mass

Neutral current neutrino events often generate neutral pions, and their invariant mass M_{π^0} can be reconstructed by using two showering rings as follows;

$$M_{\pi^0} = \sqrt{2p_1p_2(1 - \cos \Theta)}, \quad (6.35)$$

where p_1 and p_2 are each reconstructed momentum and Θ is the opening angle between the two rings. In order to evaluate the invariant mass of π^0 , FC events of the data and the atmospheric neutrino MC are used. The selection criteria are as follows:

- Vertex in the fiducial volume
- Number of rings = 2
- All rings are identified as showering ring

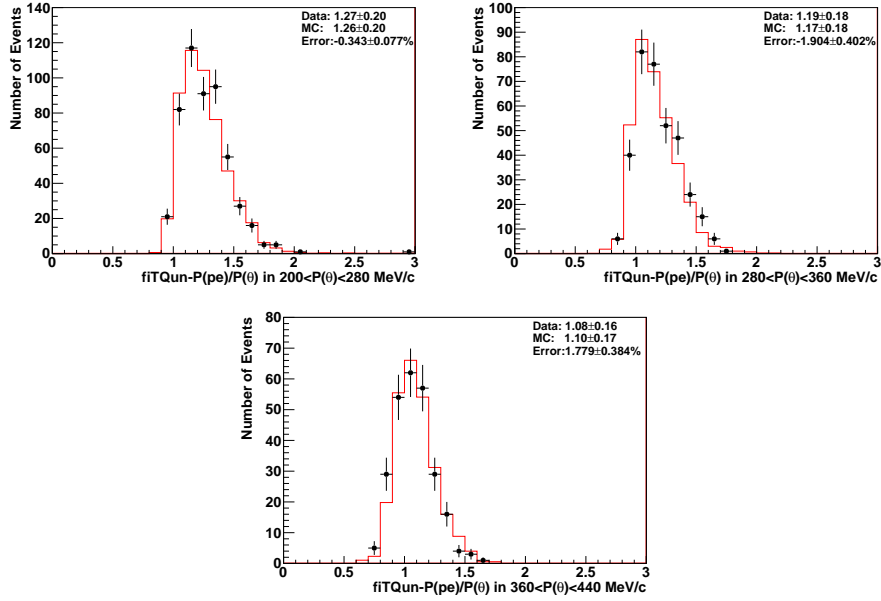


Figure 6.37: Distributions of $p(\text{p.e.})/p(\theta)$ at each $p(\theta)$ bin for the data (black points) and the MC (red). From the top left plot to the bottom plot, the $p(\theta)$ corresponds to 200-280 MeV/c, 280-360 MeV/c and 360-440 MeV/c, respectively.

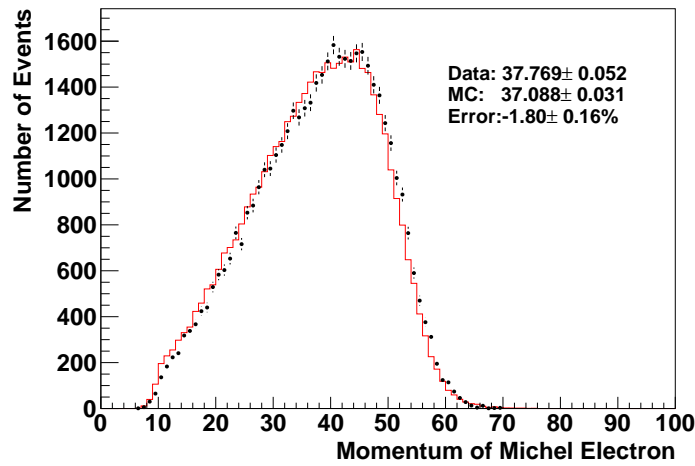


Figure 6.38: Momentum of Michel electrons for the data (black points) and the MC (red).

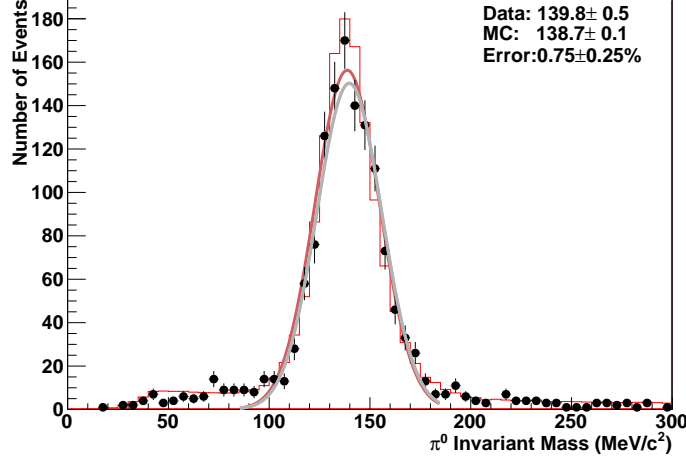


Figure 6.39: Invariant mass of neutral pions for the data (black points) and the MC (red). The solid lines show the Gaussian fitting lines.

- Number of Michel electrons = 0

For fitQun with $D_{\text{wall}} = 1.5$ m, the distributions of the invariant π^0 mass for the data and the MC are shown in Figure 6.39. The Gaussian fitted peak positions are compared to both the data and MC, and the error is obtained as $(0.75 \pm 0.25)\%$.

6.6.5 Energy Scale Error

The final absolute energy scale error of fitQun is defined as the most deviated error in all the errors described as above. Figure 6.40 shows the summarized errors, and then the absolute energy scale error is to be -1.90% . In addition to this, the time variation of the energy scale should be considered. For that purpose, the p/range and the momentum of Michel electrons are monitored in time as shown in Figure 6.41. The p/range has been almost stable ($(-0.02 \pm 0.01)\%$ per year), whereas the Michel electron momentum has been changing by $(0.21 \pm 0.03)\%$ per year. This change is considered as due to the increasing the PMT hit rate as shown in Appendix B. The time variation errors are defined as the maximum value of the ratios of the RMS to the mean, which is 0.88% (0.28% for the p/range , 0.88% for the momentum of Michel electrons). Then, the final energy scale error is estimated as the square root of the final absolute and time variation energy scale error, which is 2.1% for fitQun with $D_{\text{wall}} = 1.5$ m (2.1% for APfit with $D_{\text{wall}} = 2.0$ m).

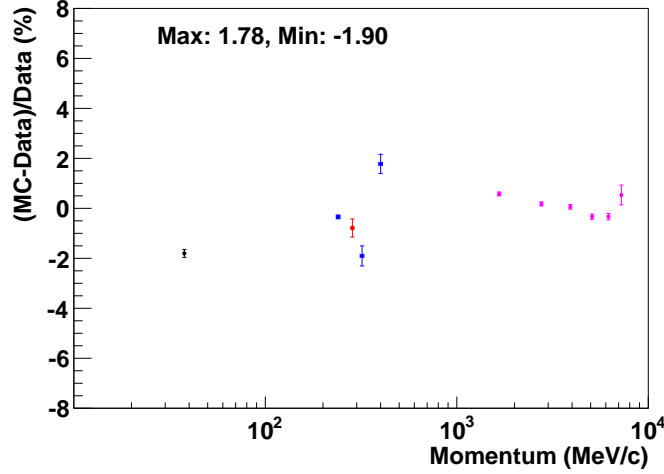


Figure 6.40: Absolute energy scale errors for fitQun with $D_{\text{wall}} = 1.5$ m. The horizontal axis is the estimated momentum. The black and red points show the errors related to Michel electrons and neutral pions, respectively. The blue and purple points show the errors related to the low and high energy stopping muons, respectively. The final absolute energy scale error is -1.90%.

6.6.6 Uniformity of Energy Scale Error

The detector uniformity of the energy scale is important especially for reconstructing the total momentum in proton decay analysis. In order to check the uniformity, Michel electrons are the good control sample since their vertices and momenta are uniformly distributed in the detector and in all the directions, respectively. Michel electrons are selected by the following criteria.

- Total observed charge $> 1,000$ p.e.s
- $N_{50} > 60$
- Goodness of the stopping muon fit > 0.5
- Number of Michel electrons = 1
- Decay time $> 1.2 \mu\text{s}$
- Michel electron vertex is inside the fiducial volume
- $|\cos \Theta_{\mu e}| < 0.25$

Here, $\Theta_{\mu e}$ is the angle between parent muons and Michel electrons. The last criterion is to select the Michel electron whose direction is perpendicular to the

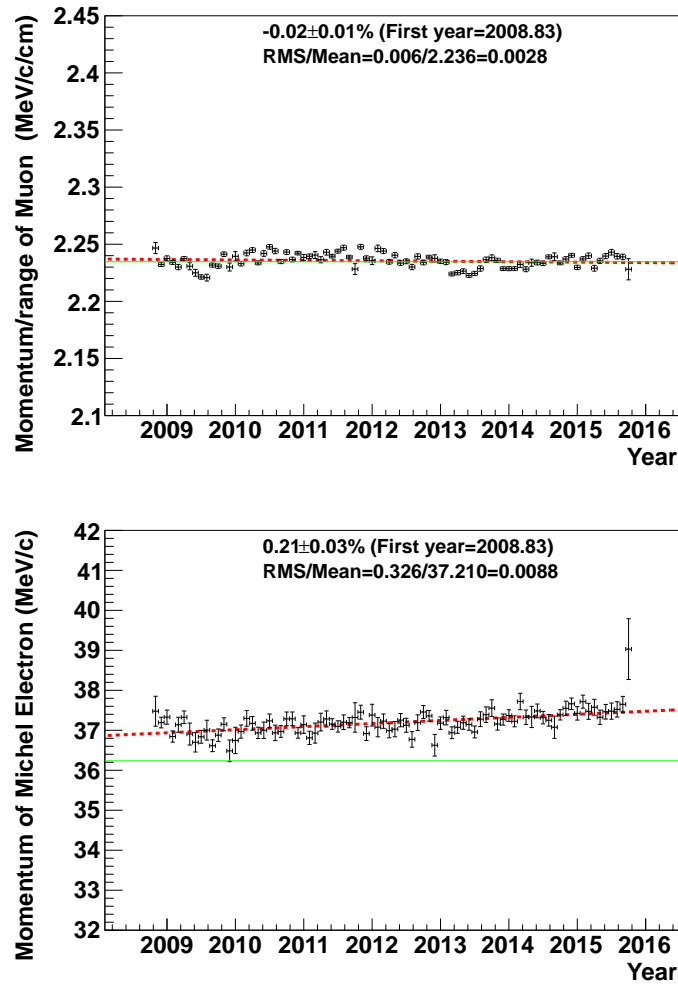


Figure 6.41: Time variation plots of the p/range (top) and the momentum of Michel electron (bottom) for ftQun with $D_{\text{wall}} = 1.5$ m. The red dotted lines are linear fit functions. The green lines are the value of the MC.

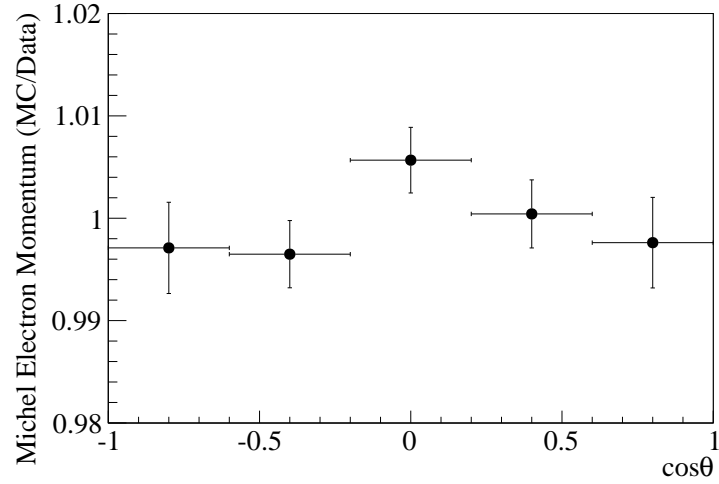


Figure 6.42: Averaged momentum of Michel electrons for the MC normalized by the data as a function of $\cos\theta$. The most deviated error in all the $\cos\theta$ bin is 0.57%.

parent muon direction in order to avoid the muon polarization effect. Figure 6.42 shows the averaged momentum of Michel electrons for the MC normalized by the data as a function of $\cos\theta$. In this thesis, the uniformity error is defined as 3σ in the vertical axis, which is 1.0% for fitQun with $D_{\text{wall}} = 1.5$ m (0.9% for APfit with $D_{\text{wall}} = 2.0$ m).

Chapter 7

Data Analysis

Searches for $p \rightarrow e^+\pi^0$ in SK-IV are performed by both APfit and fitQun. First, the selection criteria are defined by using some reconstruction parameters. Then, the systematic errors of the signal efficiency and the background rate are estimated. For the background rate estimation, each atmospheric neutrino MC events are reweighed by considering the solar activity and the two flavor neutrino oscillation effect ($\nu_\mu \leftrightarrow \nu_\tau$ with $\Delta m^2 = 2.5 \times 10^{-3} \text{ eV}^2$ and $\sin^2 2\theta = 1.0$). Before opening the data, we confirm the MC agreement with the data in the outside the signal region sample. Finally, we discuss the result and set the partial lifetime limit of protons by combining the result of SK-IV and the APfit results of SK-I to SK-III.

7.1 Selection Criteria

In this decay mode, a positron and a neutral pion are emitted back-to-back in the rest frame of a proton. The neutral pion decays promptly ($\sim 10^{-16}$ sec) into two γ -rays and these two create two e -like rings by the electromagnetic shower process after traveling about 40 cm in water. A typical signal MC event which has three e -like rings is shown in Figure 7.1. The $p \rightarrow e^+\pi^0$ signal is selected from the fully contained (FC) sample by following criteria for both APfit and fitQun:

1. Distance from the wall to the reconstructed vertex > 150 (200) cm for fitQun (APfit)
2. 2 or 3 rings
3. All rings should be identified as e -like
4. No Michel electron
5. $85 \text{ MeV}/c^2 < \pi^0 \text{ mass} < 185 \text{ MeV}/c^2$ for 3-ring events

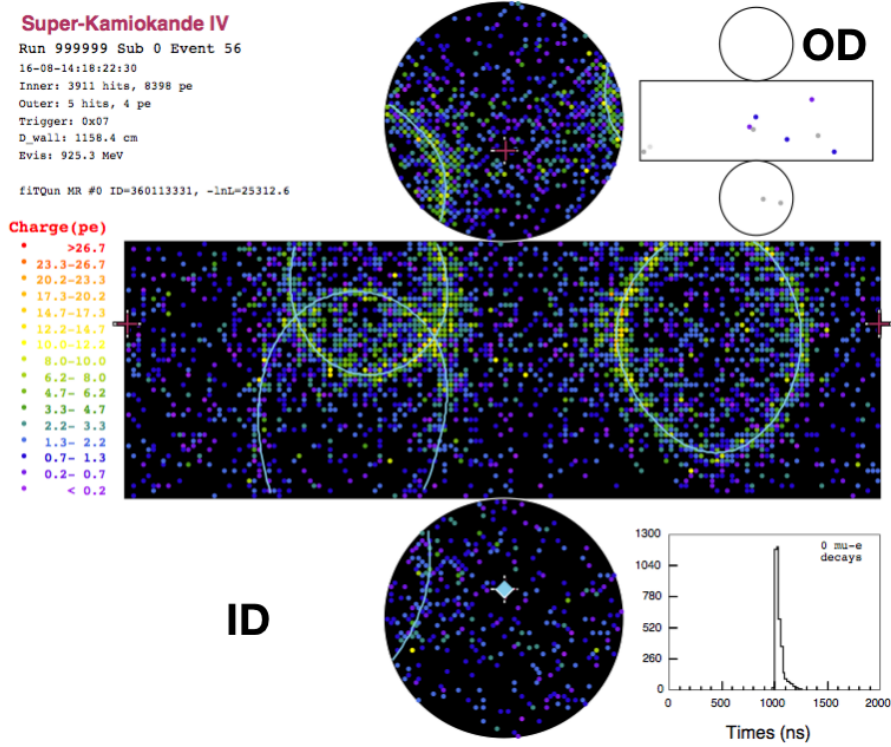


Figure 7.1: Typical $p \rightarrow e^+\pi^0$ MC event display in SK-IV. A free proton decayed at around the tank center. It emitted a positron on the right and a neutral pion on the left. As a result of the pion decay, three e -like rings are observed. Each dot corresponds to a PMT and the color shows the amount of the observed charge. Solid lines represent the fitQun reconstruction rings. FiTQun found all the 3 e -like ring correctly.

6. $830 (800) \text{ MeV}/c^2 < \text{total invariant mass} < 1050 \text{ MeV}/c^2$ and total momentum $< 250 \text{ MeV}/c$ for fitQun (APfit)
7. No tagged neutrons for SK-IV

As described in Section 6.5, thanks to the better reconstruction of fitQun, the definition of the fiducial volume (FV) for fitQun is expanded from that of APfit. Figure 7.2 shows the signal efficiencies in each bin of the distance from the wall to the true vertex after applying the selection criteria 2-7. For fitQun, the reconstructed vertex of the most energetic ring is adopted for the determination of the vertex of the event. The efficiencies for fitQun around near the wall region are higher than that of APfit. The FV for fitQun is selected as 1.5 m inside the wall where its efficiency (= (Number of final events)/(Number

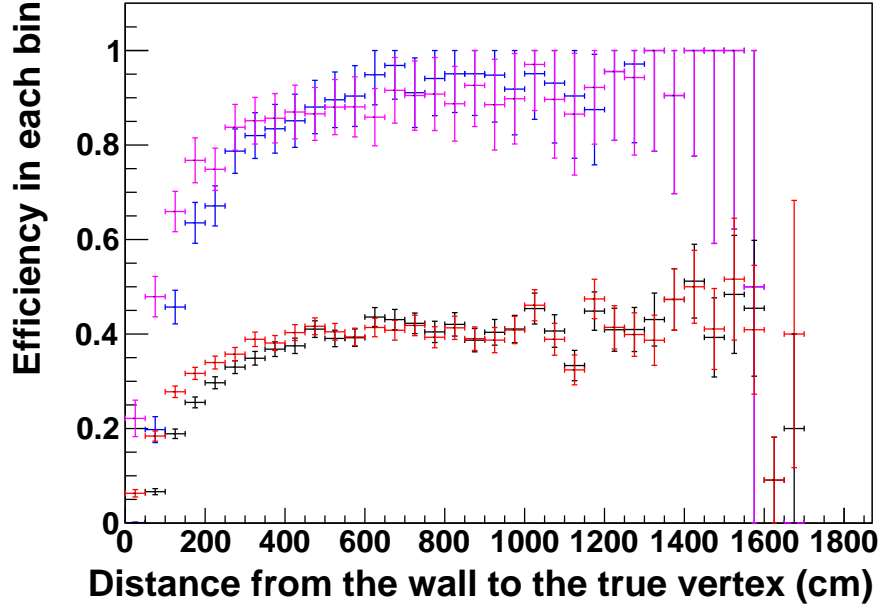


Figure 7.2: Signal efficiencies in each bin of the distance from the wall to the true vertex after applying the selection criteria 2-7. Black (blue) and red (purple) points show the efficiencies in all (free) protons for APfit and fitQun, respectively.

of FC true-FV events)) for all protons becomes similar to that of APfit while the FV for APfit is defined as 2 m inside the wall.

Since the decaying π^0 has a momentum of 459.43 MeV/c, the two γ -rays are Lorentz-boosted. Then, in the laboratory frame, one of them can take a very low momentum which can not be reconstructed. Taking into account such an effect, we choose the 2- or 3-ring events by the number of rings cut. These selected rings should be e -like ring. The number of rings distributions after FCFV cut are shown in Figure 7.3. The fraction of 2-ring event and 3-ring event for free protons are 18.0% (37.9%) and 77.5% (60.5%) for fitQun (APfit), respectively. Figure 7.4 shows the fraction of the number of all e -like ring events and not-all e -like ring events.

No muons appear in $p \rightarrow e^+\pi^0$. So, the selection criterion 3 requires that the number of Michel electrons is zero (Fig. 7.5).

The mass of π^0 must be reconstructed for the case of 3-rings event. Figure 7.6 shows the distributions of the reconstructed π^0 mass by using two of the three rings and the selection region between 85 to 185 MeV/c. The Gaussian fitted π^0 mass peak and sigma are 138.0 (135.8) MeV/ c^2 and 18.6 (20.1) MeV/ c^2 for

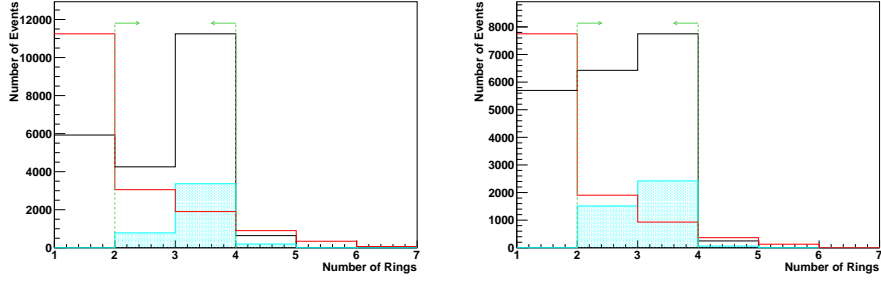


Figure 7.3: Number of rings distributions of fitQun (left) and APfit (right) for the $p \rightarrow e^+\pi^0$ MC in SK-IV (black) and the atmospheric neutrino MC (red) after applying the selection criterion 1. The shaded histogram is for free proton decay events. The green lines and arrows show the selected region.

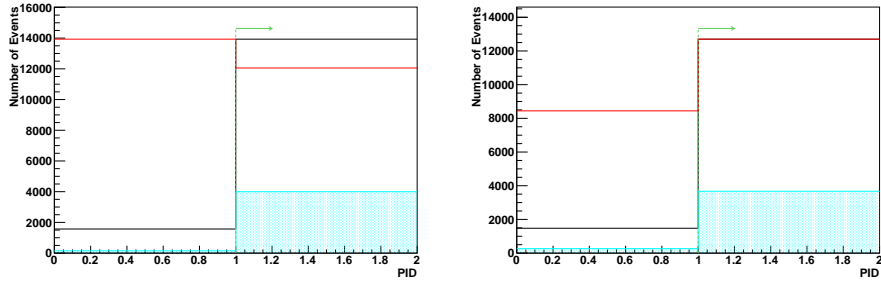


Figure 7.4: Distributions of a particle identification flag of fitQun (left) and APfit (right) for the $p \rightarrow e^+\pi^0$ MC in SK-IV (black) and the atmospheric neutrino MC (red) after applying the selection criteria 1-2. The shaded histogram is for free proton decay events. The green lines and arrows show the selected region. The first and second bin correspond to events which is not all e -like and all e -like, respectively.

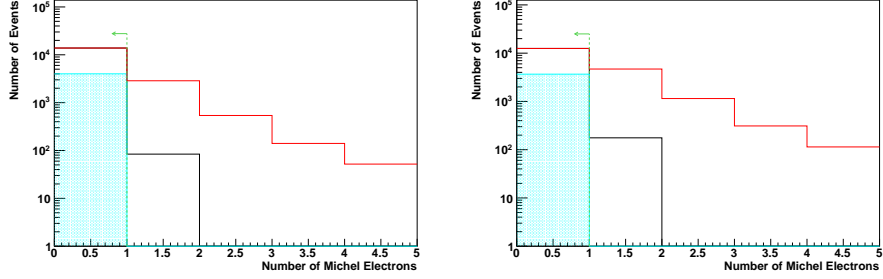


Figure 7.5: Number of Michel electrons distributions of fitQun (left) and APfit (right) for the $p \rightarrow e^+\pi^0$ MC in SK-IV (black) and the atmospheric neutrino MC (red) after applying the selection criteria 1-3. The shaded histogram is for free proton decay events. The green lines and arrows show the selected region.

fitQun (APfit), respectively.

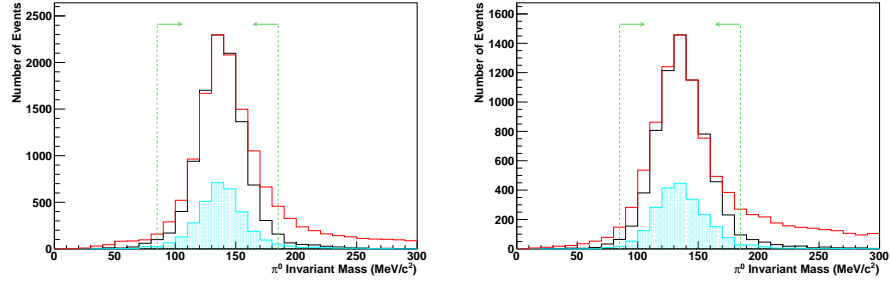


Figure 7.6: Distributions of π^0 mass of fitQun (left) and APfit (right) for the $p \rightarrow e^+\pi^0$ MC in SK-IV (black) and the atmospheric neutrino MC (red) after applying the selection criteria 1-4. The shaded histogram is for free proton decay events. The green lines and arrows show the selected region.

In order to check the reconstructed proton momentum and invariant mass, the total momentum P_{tot} , energy E_{tot} and invariant mass M_{tot} are calculated as follows;

$$P_{\text{tot}} = \left| \sum_{i=0}^{\text{all}} \vec{p}_i \right|, \quad (7.1)$$

$$E_{\text{tot}} = \sum_{i=0}^{\text{all}} |\vec{p}_i|, \quad (7.2)$$

$$M_{\text{tot}} = \sqrt{E_{\text{tot}}^2 - P_{\text{tot}}^2}, \quad (7.3)$$

Table 7.1: Performance for the determination of the total momentum and invariant mass for all and free protons in SK-IV. The total momentum resolutions are defined as 1σ deviation from the origin. The total invariant mass peak and width are obtained by Gaussian fitting.

		fitQun		APfit	
		all	free	all	free
P_{tot} (MeV/c)	σ	161	54	157	66
M_{tot} (MeV/c ²)	μ	929.5	941.7	909.2	921.4
	σ	32.6	27.6	34.7	30.2

where \vec{p}_i is the momentum of each ring. Figure 7.7 and 7.8 show the total momentum and invariant mass distributions, respectively. The total momentum resolutions defined as 1σ deviation from the origin and the Gaussian fitted total invariant mass peak and sigma are summarized in Table 7.1. Thanks to the better momentum fit of fitQun, the P_{tot} and M_{tot} distributions of fitQun are sharper than those of APfit for free protons. The difference of M_{tot} peaks between the distributions for all and free protons is due to the nuclear binding energy as discussed in Section 4.1. Since the observed charge inside the Cherenkov cone with a half angle of 70° is only used in the momentum determination of APfit (see Section 6.2.4) while fitQun uses all observed charge, the M_{tot} peak of fitQun is closer to the true proton invariant mass than that of APfit. In the M_{tot} distribution for the background, there are two peaks; the largest peak around 130 MeV/c² is the π^0 mass produced by the delta resonance neutrino interactions, the smaller peak around the origin is due to a mis-ring counting (CCQE interactions, mostly). The selection criterion 6 highly suppresses the background from the previous criterion by $0.14 \pm 0.01\%$ ($0.18 \pm 0.02\%$) for fitQun (APfit). Because most of the neutrino induced particles are emitted to the forward region, neutrino events are not isotropic and have higher total momenta and lower invariant mass.

[Two box analysis] In the previous study, the signal region is just a single box. However, in order to improve the sensitivity, we divide the signal region defined by the selection criterion 6 into two regions by total momentum: $P_{\text{tot}} < 100$ MeV/c (low- P_{tot} box) and $100 \leq P_{\text{tot}} < 250$ MeV/c (high- P_{tot} box). In the low- P_{tot} box, free proton decay events is concentrated while almost no atmospheric neutrino background events exist as shown in Figure 7.7. On the other hand, in the high- P_{tot} box, bound proton decay events are dominant while larger contamination from neutrino events can be seen. The low- P_{tot} box has much better sensitivity compared to the higher one. Therefore, we can achieve higher sensitivity by analyzing these two signal boxes separately if background becomes non-negligible in the high- P_{tot} box.

Neutrons often are produced by atmospheric neutrino interactions and captured by hydrogen after traveling a few micro seconds in water. Then 2.2 MeV

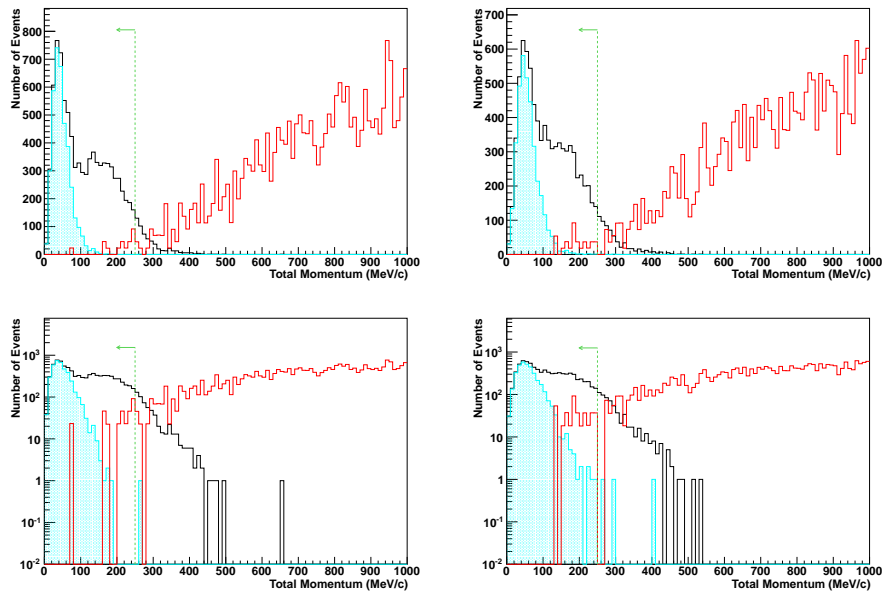


Figure 7.7: Distributions of the total momentum of fitQun (left) and APfit (right) in the linear (top) and log (bottom) scale for the $p \rightarrow e^+\pi^0$ MC in SK-IV (black) and the atmospheric neutrino MC (red) after applying the selection criteria 1-5 and the M_{tot} cut. The shaded histogram is for free proton decay events. The green lines and arrows show the selected region.

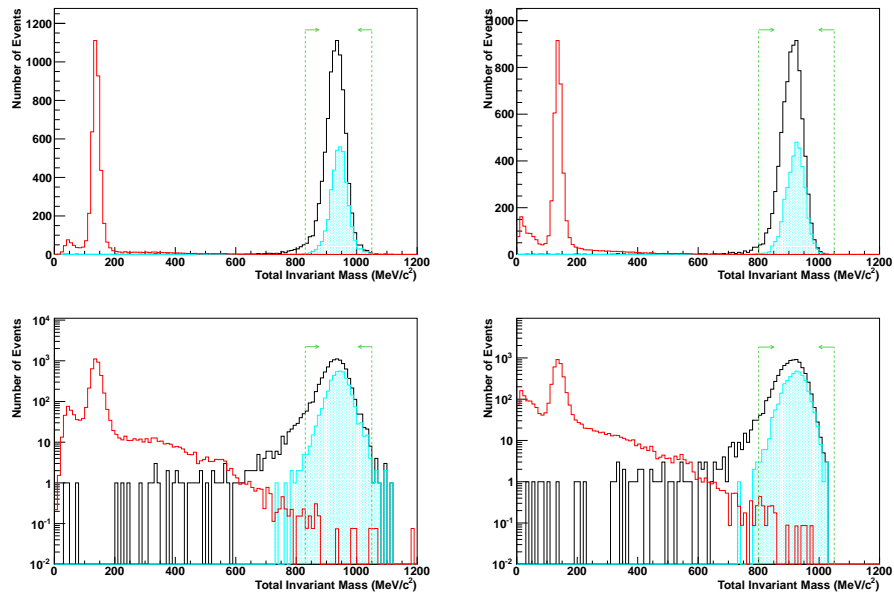


Figure 7.8: Total invariant mass distributions of fitQun (left) and APfit (right) in the linear (top) and log (bottom) scale for the $p \rightarrow e^+\pi^0$ MC in SK-IV (black) and for the atmospheric neutrino MC (red) after applying the selection criteria 1-5 and the P_{tot} cut. The shaded histogram is for free proton decay events. The green lines and arrows show the selected region.

γ -ray is finally emitted from the de-excitation of a nucleus. But, the probability of the neutron emission from the de-excitation of nucleus after proton decay in oxygen is small and no neutron emission from hydrogen. Therefore, the neutron tagging information is useful for proton decay analyses for further background rejection. The neutron tagging algorithm is available only in SK-IV thanks to the new electronics (QBEE) as described in [77]. It first searches for hit clusters as 2.2 MeV γ -ray candidates with ≥ 7 hits within a 10 ns sliding window after the prompt neutrino interaction. After that, 16 variables for a candidate event are calculated and inputted to a neural network to separate the signal from background. The neutron tagging efficiency is 20.5 ± 2.1 % while a mis-tagging rate is 1.8%. Thanks to this technique, the background rate for $p \rightarrow e^+ \pi^0$ is reduced by almost 50% while only a few percent is lost in the signal efficiency. Figure 7.9 shows the number of tagged neutrons distributions.

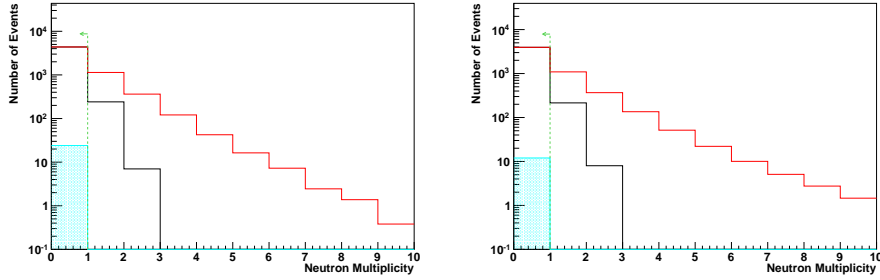


Figure 7.9: Number of tagged neutrons distributions of fiTQun (left) and APfit (right) for the $p \rightarrow e^+ \pi^0$ MC in SK-IV (black) and the atmospheric neutrino MC (red) after applying the selection criteria 1-5, excluding the signal region (criterion 6). The shaded histogram is for free proton decay events. The green lines and arrows show the selected region.

The signal efficiencies and background rates for $p \rightarrow e^+ \pi^0$ in SK-IV are summarized in Table 7.2. Figure 7.10 shows the signal efficiencies as a function of the selection criteria. The ratio between 2-ring and 3-ring events in the final signal MC events in the total P_{tot} box is roughly 2:8 (4:6) for fiTQun (APfit). In order to evaluate the background rate with a large statistics, we use the 3000 years atmospheric neutrino MC which is pre-selected for signal-like events as described in Appendix D. The effect on the signal efficiencies caused by this pre-selection is negligible small. Due to the tighter M_{tot} cut for fiTQun, the background rate of fiTQun is reduced by $(33.2 \pm 11.4)\%$ in the total P_{tot} box compared to that of APfit while keeping the same level of the signal efficiency. The expected background rate in the $800 < M_{\text{tot}} < 1050$ MeV/ c^2 and $P_{\text{tot}} < 250$ MeV region is consistent with the experimental result of $1.63^{+0.42}_{-0.33}(\text{stat})^{+0.45}_{-0.51}(\text{syst})$ events per Megaton-years obtained by the K2K's one kiloton water Cherenkov detector which measured beam neutrinos [98].

Table 7.2: Signal efficiencies and background rates in SK-IV (statistical errors only). ϵ_{all} , ϵ_{free} and ϵ_{bound} denotes the signal efficiencies for all, free and bound protons. As for the background, the 3000 years atmospheric neutrino MC which is pre-selected for signal-like events is used.

	fitQun		APfit	
	Low- P_{tot}	High- P_{tot}	Low- P_{tot}	High- P_{tot}
ϵ_{all} (%)	20.0 ± 0.3	18.1 ± 0.3	19.0 ± 0.3	19.0 ± 0.3
ϵ_{free} (%)	82.1 ± 1.4	3.3 ± 0.3	78.4 ± 1.4	7.7 ± 0.4
ϵ_{bound} (%)	4.7 ± 0.2	21.7 ± 0.3	4.2 ± 0.2	21.8 ± 0.4
BG (/Mt/yr)	0.028 ± 0.019	0.778 ± 0.102	0.030 ± 0.021	1.116 ± 0.132

The primary neutrino energy of the final background MC events is mostly distributed in a range of 1 GeV to 2 GeV as shown in Figure 7.11. The ratio between 2-ring and 3-ring events in the final background sample in the total P_{tot} box is roughly 3:7 for both APfit and fitQun. The breakdown of the neutrino interaction mode in the background is summarized in Table 7.3. There are no ν_{μ} CC events in both APfit and fitQun thanks to the good PID performance. The dominant mode of neutrino interactions is ν_e charged current with a single π^0 (ν_e CC1 π^0) interaction. A typical background ν_e CC1 π^0 event display is shown in Figure 7.12, which looks like the typical signal event (Figure 7.1). There are two background events in the low- P_{tot} box for both APfit and fitQun including one common event. The common event is induced by ν_e CC1 π^0 interaction leaving three visible e -like rings (three (two) rings are reconstructed by fitQun (APfit)) and one proton ring, but the momentum of the proton is near the Cherenkov threshold and thus this event mimics like a signal event. The fitQun-only event is a ν_e CC1 π^0 event with three visible e -like rings which are properly reconstructed by fitQun (APfit found only two rings) and seems an intrinsic background. The APfit-only event is induced by a NC single pion interaction with multi- π s in final state, in which APfit found three e -like rings and their reconstructed total mass and momentum are accidentally within the box. All background event displays overlaying with the true and reconstructed rings are checked and then we find out that there is no serious reconstruction failure in both APfit and fitQun.

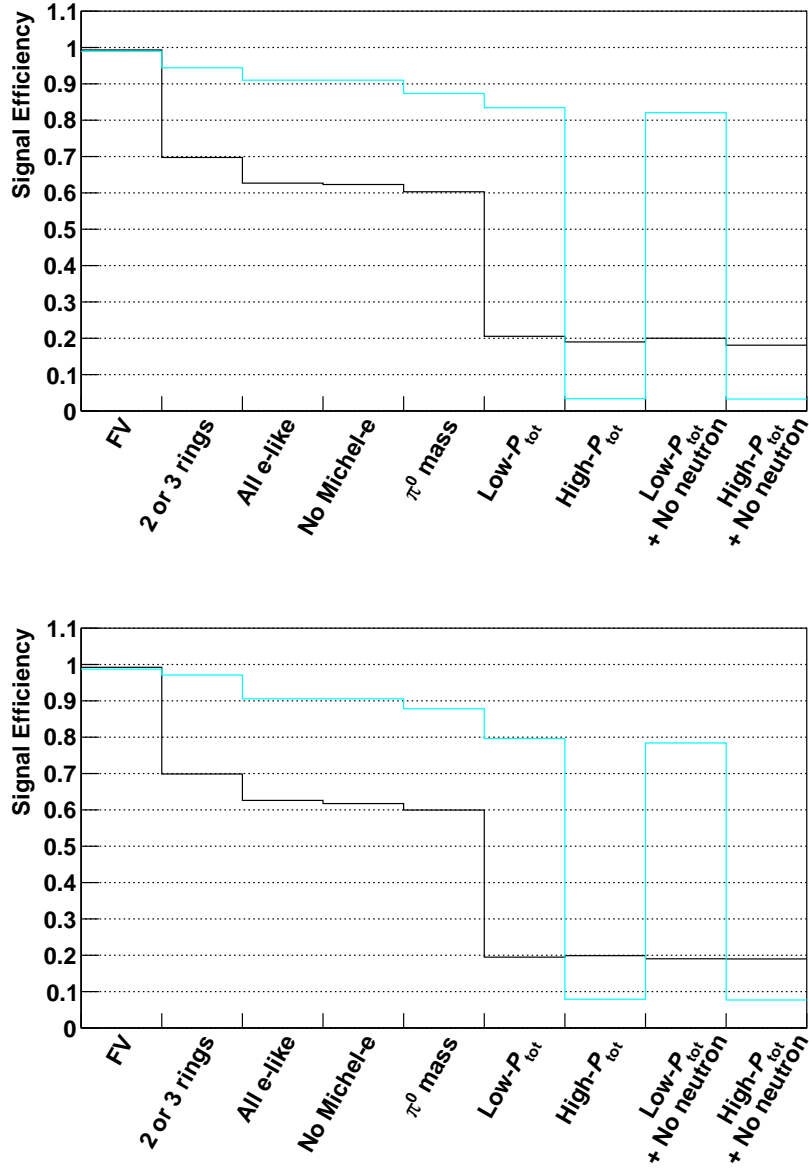


Figure 7.10: Signal efficiencies after each selection criterion for the $p \rightarrow e^+\pi^0$ MC in SK-IV. Top (bottom) figure is for fitQun (APfit). Black (blue) histogram is for all (free) proton decay. The signal efficiencies are normalized to the number of events after the FC true-FV cut.

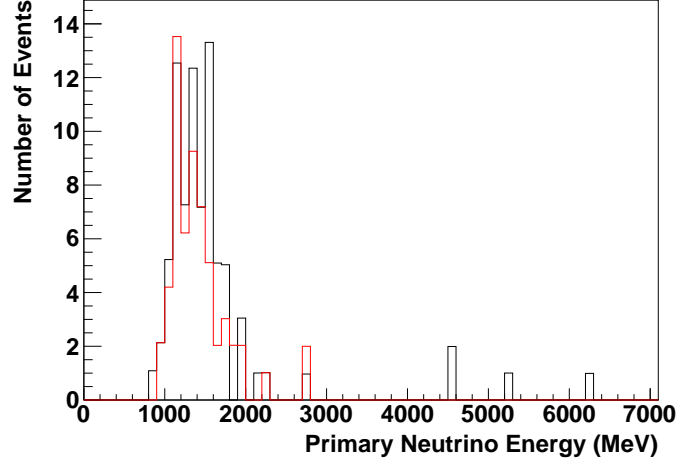


Figure 7.11: Primary neutrino energy distributions of the final events in the total P_{tot} box in the 3000 years atmospheric neutrino MC. Black (red) histogram is for APfit (fitQun).

Table 7.3: Breakdown of neutrino interaction modes for the final events in the total P_{tot} box in SK-IV (statistical errors only). The 3000 years atmospheric neutrino MC which is pre-selected for signal-like events is used. N_{ev} is the number of events without the reweighing factor. Numbers in parentheses are N_{ev} in the low- P_{tot} box.

Interaction	fitQun		APfit		Common
	Fraction (%)	N_{ev}	Fraction (%)	N_{ev}	N_{ev}
ν_e CC single- π	58.5 ± 9.9	35 (2)	60.3 ± 8.6	49 (1)	21 (1)
ν_e CCQE	18.4 ± 5.5	11	14.8 ± 4.3	12	6
ν_e CC coherent- π	5.0 ± 2.9	3	4.9 ± 2.5	4	2
ν_e CC single- η	5.0 ± 2.9	3	4.9 ± 2.5	4	1
ν_e CC multi- π	3.3 ± 2.4	2	3.7 ± 2.1	3	0
ν_e CC DIS	3.3 ± 2.4	2	0	0	0
NC single- π	1.7 ± 1.7	1	2.5 ± 1.7	2 (1)	0
NC single- γ	1.7 ± 1.7	1	0	0	0
NC multi- π	0	0	3.7 ± 2.1	3	0
NC DIS	0	0	2.5 ± 1.7	2	0

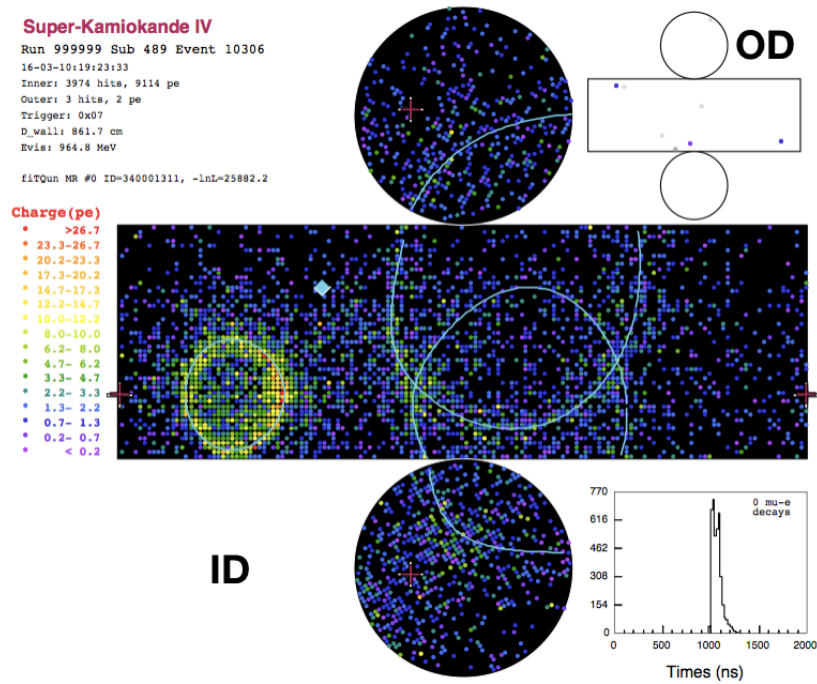


Figure 7.12: Typical background MC event display in SK-IV. The type of neutrino interaction of this event is $\nu_e CC1\pi^0$. The three solid blue lines are the fitQun reconstructed e -like rings. FitQun catches each edge of the Cherenkov ring properly.

7.2 Systematic Errors

In this section, the systematic error estimation of the fitQun based analysis in SK-IV is described, which is basically the same as that of the APfit based analysis. The systematic errors of the APfit based analysis for SK-I to SK-IV in the latest published paper [1] are used for the combined analysis discussed in section 7.5. Since the observation time is well defined and the detector is always full of water, the systematic error of the detector exposure is negligible. However, we assign the systematic error of 1% for the exposure for just in case.

Pion Final State Interaction

A neutral pion generated by proton decay or a neutrino interaction in oxygen can interact within that oxygen nucleus. By this nuclear effect, a pion can be scattered, exchange its charge or even be absorbed (final state interaction, FSI). It is also possible to interact with other nuclei in water after escaping the original nucleus (secondary interaction, SI). Those interactions are simulated by the NEUT pion cascade model as discussed in Section 4.1.

In order to evaluate this model uncertainty, the original model is weighted by the 6 parameters based on some pion scattering data. The detailed weighting method can be found in [61]. The parameters represent the interaction probabilities for quasi-elastic scattering and charge exchange in two energy regions (π momentum is less or greater than 500 MeV/c), inelastic scattering and absorption. The 24 weighted parameter sets are prepared and the number of events in the final sample is calculated for each set. For the pion final state interaction error, RMS/mean of those 24 values is used.

Correlated Decay

For proton decays in oxygen, it is expected that 10% of nucleons decay under the effect of other nucleons as described in Section 4.1. We conservatively assign a 100% source error for this effect because it is not well understood. The systematic error of this decay is calculated by taking the fractional difference between the following two numbers:

$$n_{\text{def}} = n_H + n_{16\text{O}_{\text{norm}}} + n_{16\text{O}_{\text{corr}}} \quad (7.4)$$

$$n_{\text{wei}} = n_H + \frac{N_{16\text{O}_{\text{norm}}} \mp \alpha N_{16\text{O}_{\text{corr}}}}{N_{16\text{O}_{\text{norm}}}} n_{16\text{O}_{\text{norm}}} + (1 \pm \alpha) n_{16\text{O}_{\text{corr}}} \quad (7.5)$$

Here, n (N) is the number of events in the final (FC true-FV) sample, H (16O_{norm} , 16O_{corr}) corresponds to proton decays in hydrogen (normal decay in 16O , correlated decay in 16O) respectively. α is the source error and it is set to be 1.

Fermi Motion

In the signal MC, the nucleon momentum is simulated by using the experimental spectrum function as described in Section 4.1. On the other hand, the Fermi gas model is used in the atmospheric neutrino MC. This model uncertainty is considered by taking the fractional difference between the number of final events under the spectral function (n_{def}) and that of the Fermi gas model (n_{Fermi}).

As shown in Figure 7.13, the proton momentum distribution for the Fermi gas model is evaluated by weighting the spectrum function and its maximum momentum is 225 MeV/c which is the Fermi surface momentum simulated in NEUT. n_{Fermi} is defined as,

$$n_{\text{Fermi}} = n_H + \sum_{i=1}^{11} \frac{n_{16\text{O},i}}{N_{16\text{O},i}} N_{16\text{OFermi},i} \quad (7.6)$$

where $N_{16\text{OFermi},i}$ is the number of events for the i -th momentum bin (the bin width = 25 MeV) in the FC true-FV sample under the weighted momentum distribution. $N_{16\text{OFermi},i}$ is normalized as follows.

$$\sum_{i=1}^{11} N_{16\text{O},i} = \sum_{i=1}^{11} N_{16\text{OFermi},i} \quad (7.7)$$

The Fermi motion error of the APfit high- P_{tot} box is lower than that of fitQun since the fraction of free proton events in the high- P_{tot} box is larger.

Fiducial Volume

The systematic error of the fiducial volume affects the number of events, directly. However, there is no control sample for the vertex reconstruction accuracy of two or three ring events. For single non-shower-ring events, we can estimate the vertex reconstruction accuracy by using the cosmic ray muon events since their entering points should be the ID wall position as shown in Figure 6.32. The MC-data differences of the entering muon peak positions are smaller than 2 cm. We can calculate the fiducial volume error based on this single non-shower-ring sample as 0.4% by shifting the fiducial volume boundary inward/outward with 2 cm.

Another method to evaluate the fiducial volume error is to use the FC sub-GeV multi-ring atmospheric neutrino MC and data whose event topologies are more similar to $p \rightarrow e^+\pi^0$ than that of single non-shower-ring events. Here, we check the overall vertex reconstruction accuracy in several volume regions; $D_{\text{wall}} > 50$ cm and 100 cm (and also 150 cm for APfit). Figure 7.14 shows the D_{wall} distributions and the MCs are normalized by area to the data. In each distribution, the number of events whose vertices are within the fiducial volume are calculated for both the data and MC, and an error is then estimated by comparing that value for both the data and MC. Finally, the fiducial volume error by this multi-ring sample is obtained as 0.6% (0.7% for APfit) by taking

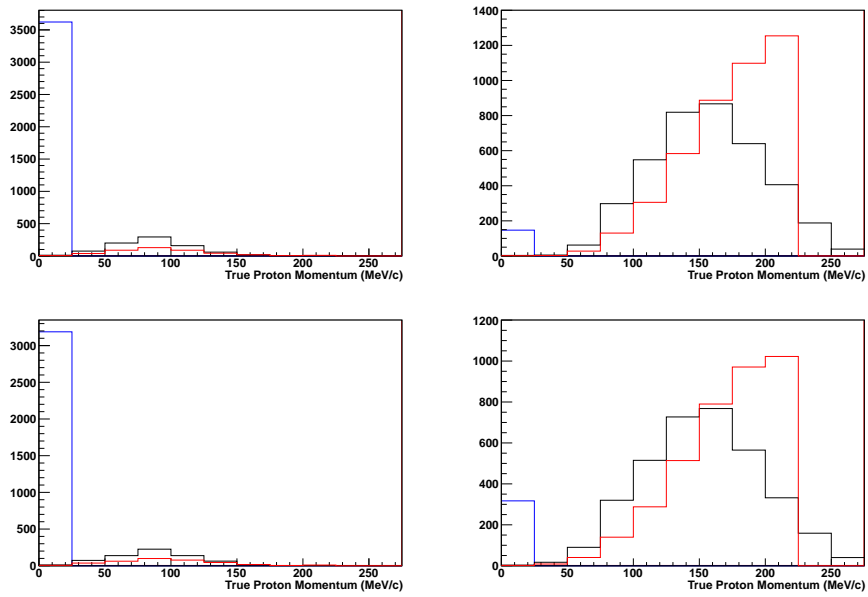


Figure 7.13: True proton momentum distributions of the final events for the low- P_{tot} (left) and the high- P_{tot} (right) box in the $p \rightarrow e^+\pi^0$ MC. The top (bottom) figures are for fitQun (APfit). The black (red) histograms show bound proton events under the experimental spectrum function (Fermi gas model) and the blue histograms show free proton events.

the average and RMS of those errors. We use this 0.6% error as the systematic error of the fiducial volume for both the low- P_{tot} and high- P_{tot} box.

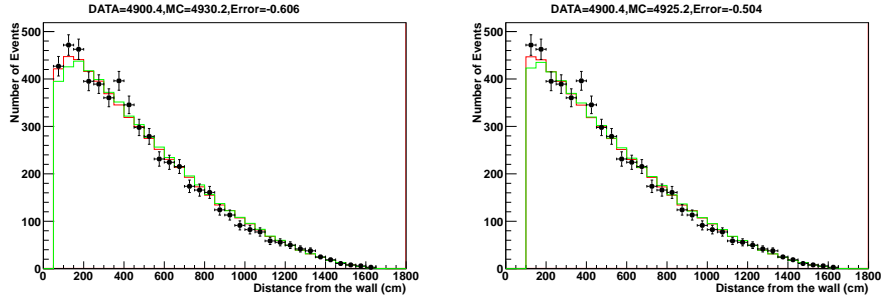


Figure 7.14: D_{wall} distributions of the FC sub-GeV multi-ring events for both the atmospheric neutrino MC (lines) and data (dots) for fitQun. The red (green) line shows the reconstructed (true) D_{wall} . The MCs are normalized by area to the data.

Detector Non-Uniformity

The detector non-uniformity causes the imbalance of the reconstructed momentum which is important to reconstruct protons. As described in Section 6.6, the detector non-uniformity error is assigned as 1.0% for fitQun (0.9% for APfit). The systematic error of the detector non-uniformity is evaluated by shifting the total momentum region upward/downward with a twice of the non-uniformity error and see how the final number varies. Here, we multiply the original non-uniformity error by two since most of $p \rightarrow e^+\pi^0$ events are observed by two opposite sides each other.

Energy Scale

The energy scale error directly affects the total momentum and the invariant mass selection, which is set to be 2.1% for fitQun (2.1% for APfit) as described in Section 6.6. The number of final events is compared by shifting the total momentum and invariant mass regions upward/downward with this energy scale error, and its fluctuation gives the systematic error of the energy scale.

PID and Ring Counting

The agreement of likelihood distributions between the data and the MC is important for both the PID and ring counting uncertainty. As an example of the good agreement of the PID likelihood distribution for single-ring events, the

mis-PID rates of both the data and MC for the stopping muon (its Michel electron) events are $0.10 \pm 0.03\%$ ($0.61 \pm 0.08\%$) and $0.15 \pm 0.03\%$ ($0.48 \pm 0.04\%$), respectively (see Figure 6.19).

For more realistic estimation, we use the FCFV sub-GeV multi-ring sample and FCFV sub-GeV e -like ring sample for the PID and ring counting, respectively. The systematic errors of the PID and ring counting likelihoods are evaluated by comparing each likelihood distribution of the atmospheric neutrino MC and the data. If there are some systematic differences between the data and the MC, the likelihood distribution would be wider/narrower and/or shifted upward/downward direction. Therefore, the likelihood distribution of the MC is shifted and scaled so that the disagreement with the data becomes minimal (a χ^2 test) as shown in Figure 7.15, and the fractional difference of events passed through the threshold between the tuned MC and the data is used as the systematic error. The systematic errors for the PID and ring counting likelihoods are obtained as 0.3% and 0.3%, respectively. We assign these errors for both the low- P_{tot} and high- P_{tot} box.

Neutrino Flux and Cross Section

The systematic errors of the neutrino flux and the cross section are evaluated by an event-by-event weighting method for each error based on atmospheric neutrino analyses in SK, which can be found in [99, 100].

For the neutrino flux error, the following error sources are considered in this analysis.

- Energy dependent normalization
- Neutrino flavor ratio
- $\bar{\nu}/\nu$ ratio
- Up/down asymmetry
- Horizontal/vertical ratio
- K/π production ratio
- Neutrino flight length

The dominant source error in the neutrino flux is the energy dependent normalization which includes the uncertainty of the production of π and K in a hadronic interaction model, hadronic interaction cross sections and atmospheric density profile. Those model uncertainties are evaluated in [65] by comparing the observed data with the calculation of the atmospheric muon flux as shown in Figure 7.16. Table 7.4 shows each neutrino flux error.

For the neutrino cross section, the following items are considered.

- M_A (axial vector mass) in quasi-elastic scattering and single-meson production

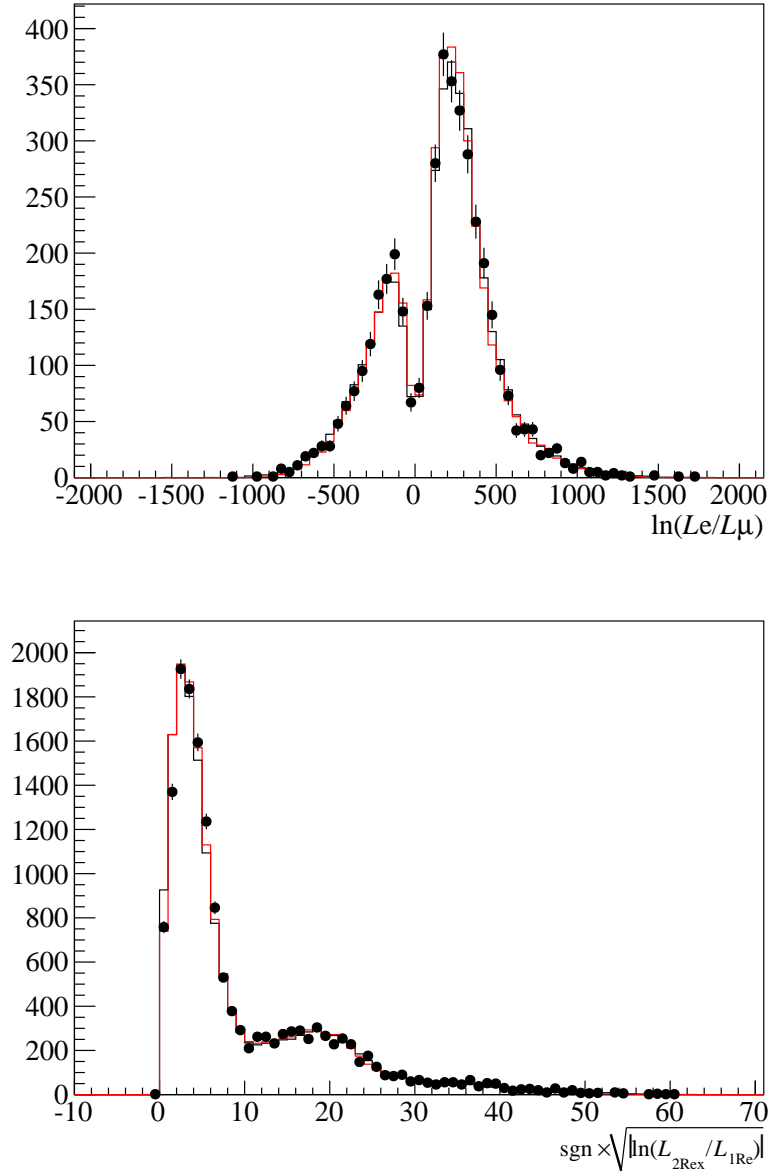


Figure 7.15: Distributions of the PID likelihood ratio $\ln(L_e/L_\mu)$ (top) and the ring counting likelihood ratio $\sqrt{|\ln(L_{2\text{ReX}}/L_{1\text{Re}})|}$ (bottom) in the FCFV sub-GeV sample for the data (black points), the nominal MC (black histogram) and the tuned MC (red histogram). In the top figure, the likelihood ratio of the most energetic ring is displayed.

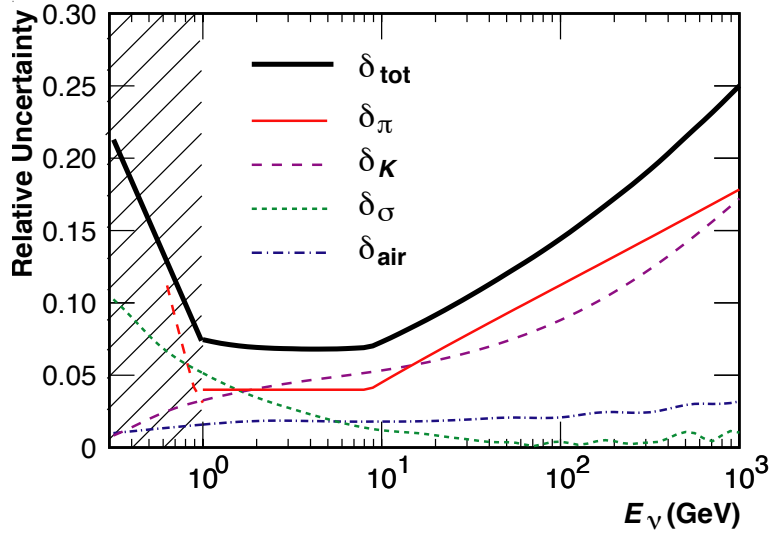


Figure 7.16: Uncertainties of the atmospheric neutrino flux as a function of neutrino energy. δ_π , δ_K , δ_σ , δ_{air} and δ_{tot} are the uncertainty of π and K production, hadronic interaction cross sections, atmospheric density profile and their sum. Taken from [65].

- Quasi-elastic scattering for bound nucleons (total cross section)
- Quasi-elastic scattering for bound nucleons ($\bar{\nu}/\nu$)
- Quasi-elastic scattering for bound nucleons (flavor ratio)
- Single(multi)-meson production (total cross section)
- Single(multi)-meson production (model dependence)
- Coherent pion production
- NC/CC ratio

The largest source error in the neutrino cross section is the single-meson production which is determined by comparing the form factor of the model [84] with the experimental data from bubble chamber experiments [85] as discussed in 4.2. Table 7.5 shows each neutrino cross section error.

Michel Electron

The systematic error of the Michel electron tagging is evaluated by comparing the number of tagged Michel electrons between the FCFV sub-GeV one μ -like ring sample of the atmospheric neutrino MC and the data. Figure 7.17 shows

Table 7.4: Systematic errors from uncertainties of the neutrino flux in SK-IV.

	fitQun	APfit
(Energy dependent)		
Normalization		
$(E_\nu < 1\text{GeV})$	7.9%	7.0%
$(E_\nu > 1\text{GeV})$	4.5%	4.0%
ν_μ/ν_e ratio		
$(E_\nu < 1\text{GeV})$	0.7%	0.6%
$(1 < E_\nu < 10\text{GeV})$	1.1%	0.8%
$(E_\nu > 10\text{GeV})$	<0.1%	<0.1%
$\bar{\nu}_e/\nu_e$ ratio		
$(E_\nu < 1\text{GeV})$	0.9%	0.8%
$(1 < E_\nu < 10\text{GeV})$	2.2%	1.6%
$(E_\nu > 10\text{GeV})$	<0.1%	<0.1%
$\bar{\nu}_\mu/\nu_\mu$ ratio		
$(E_\nu < 1\text{GeV})$	<0.1%	<0.1%
$(1 < E_\nu < 10\text{GeV})$	<0.1%	0.2%
$(E_\nu > 10\text{GeV})$	<0.1%	<0.1%
Up/down asymmetry	<0.1%	0.3%
Horizontal/vertical ratio	0.2%	<0.1%
K/ π production ratio	<0.1%	<0.1%
Neutrino flight length	<0.1%	<0.1%
Total	9.5%	8.3%

Table 7.5: Systematic errors from uncertainties of the neutrino cross sections in SK-IV.

	fitQun	APfit
M_A in QE and single-pion production	9.9%	7.5%
NC elastic and CCQE ratio	7.5%	6.2%
CCQE $\bar{\nu}/\nu$ ratio	0.9%	0.4%
CCQE μ/e ratio	0.1%	0.1%
Single-meson production	9.6%	9.4%
Single-pion production	14.5%	22.4%
DIS (model comparison)	2.5%	1.6%
DIS	0.4%	<0.1%
Coherent pion production	1.2%	1.5%
NC/CC ratio	0.7%	<0.1%
Total	21.6%	26.3%

the distributions of the number of Michel electrons. This systematic error for the signal efficiency is negligible small.

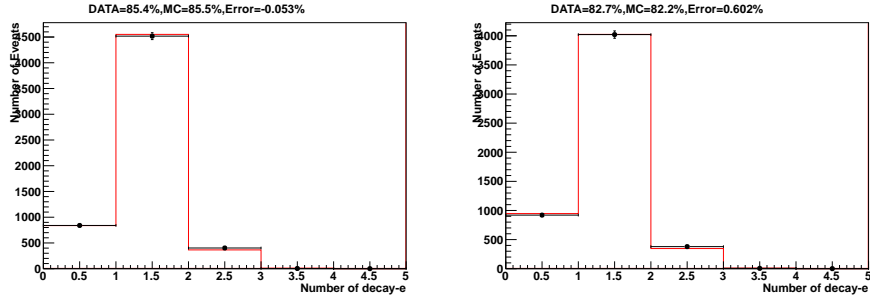


Figure 7.17: Distributions of the number of Michel electrons for both fitQun (left) and APfit (right). The dots (red lines) show the data (atmospheric neutrino MC) of the FCFV sub-GeV one μ -like ring events.

Neutron Tagging

In the SK-IV analysis, the neutron tagging information is used. The systematic error of the neutron tagging is estimated by comparing the number of tagged neutrons between the atmospheric neutrino MC and the data. The events outside the signal region are used in this check after applying the other selection criteria. Figure 7.18 shows the distributions of the number of neutrons. This systematic error for the signal efficiency is negligible small.

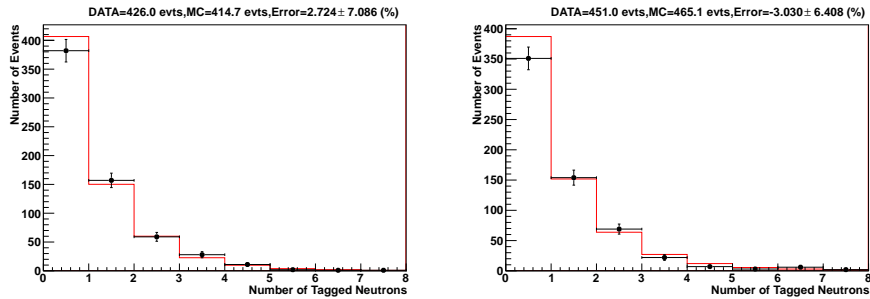


Figure 7.18: Distributions of the number of tagged neutrons for both fitQun (left) and APfit (right). The dots (red lines) show the data (atmospheric neutrino MC) of the events outside the signal region after applying the other selection criteria.

Table 7.6: Systematic errors for the signal efficiencies in SK-IV.

	fitQun		APfit (reference)	
	Low- P_{tot}	High- P_{tot}	Low- P_{tot}	High- P_{tot}
(Interaction)				
Pion FSI/SI	2.9%	11.9%	2.6%	11.7%
Correlated decay	2.0%	10.0%	1.9%	9.4%
Fermi motion	9.0%	10.3%	8.3%	6.2%
(Detector & Reconstruction)				
Fiducial volume	0.6%	0.6%	0.7%	0.7%
Detector non-uniformity	1.3%	0.5%	1.7%	0.3%
Energy scale	1.5%	2.1%	1.8%	1.9%
PID	0.3%	0.3%	2.7%	2.7%
Ring counting	0.3%	0.3%	0.1%	0.1%
Total	9.9%	18.8%	9.7%	16.6%

Summary of the Systematic Errors

Table 7.6 and 7.7 show the systematic errors for the signal efficiencies and the background rate. The systematic errors of the signal efficiency for fitQun (APfit) are 9.9% (9.7%) and 18.8% (16.6%) for the low- P_{tot} box and the high- P_{tot} box, respectively. The systematic errors of the background rate for fitQun (APfit) is 41.4% (40.6%) for the total P_{tot} box. Both fitQun and APfit have similar systematic errors in the SK-IV analysis.

Table 7.7: Systematic errors for the background rates for the total P_{tot} box in SK-IV.

	fiTQun	APfit (reference)
(Interaction)		
Neutrino flux	9.5%	8.3%
Neutrino cross section	21.6%	26.3%
Pion FSI/SI	9.3%	6.6%
(Detector & Reconstruction)		
Fiducial volume	0.6%	0.7%
Detector non-uniformity	10.3%	10.0%
Energy scale	29.4%	25.5%
PID	0.3%	2.7%
Ring counting	0.3%	0.1%
Michel electron	0.1%	0.6%
Neutron tagging	9.8%	9.4%
Total	41.4%	40.6%

7.3 MC-Data Agreement in the Outside the Signal Region

Before opening the data in the signal region, the agreement between the SK-IV data and the atmospheric neutrino MC is checked in the outside the signal region data with a margin of 100 MeV. Figure 7.19 - 7.23 show the distributions of the outside sample for the number of Michel electrons, π^0 mass, number of tagged neutrons, total momentum and invariant mass, respectively. In these distributions, there are no significant differences between the data and the MC can be found. The data was well reproduced by the MC.

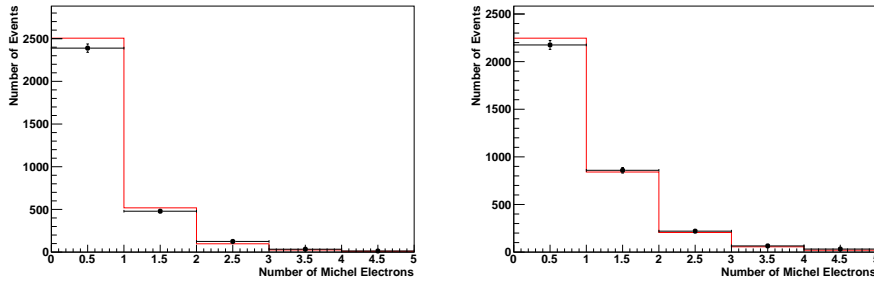


Figure 7.19: Number of Michel electrons distributions of fitQun (left) and APfit (right) for the outside the signal region sample in the SK-IV data (black) and the 500 years atmospheric neutrino MC (red) after applying the selection criteria 1-3. The MC is normalized by the live time of the data.

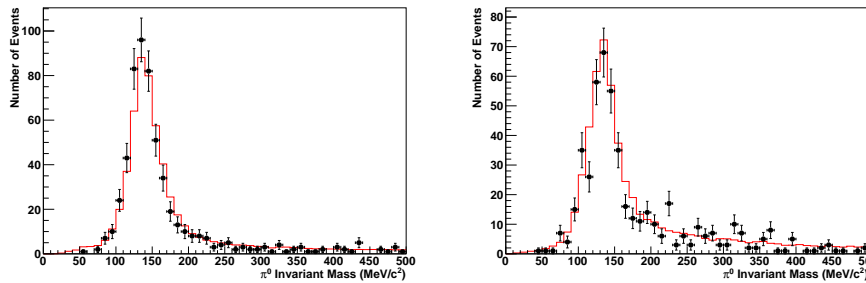


Figure 7.20: Distributions of π^0 mass of fitQun (left) and APfit (right) for the outside the signal region sample in the SK-IV data (black) and the 500 years atmospheric neutrino MC (red) after applying the selection criteria 1-4. The MC is normalized by the live time of the data.

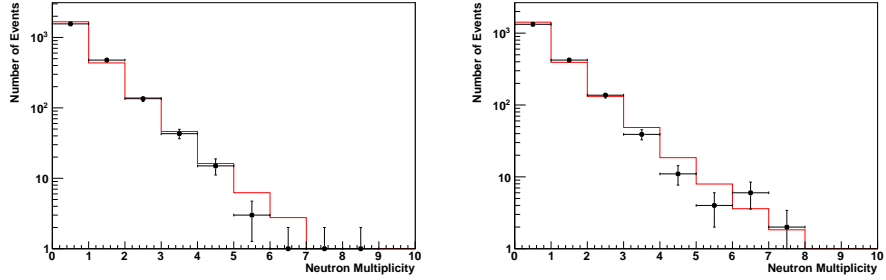


Figure 7.21: Number of tagged neutrons distributions of fitQun (left) and APfit (right) for the outside the signal region sample in the SK-IV data (black) and the 500 years atmospheric neutrino MC (red) after applying the selection criteria 1-5. The MC is normalized by the live time of the data.

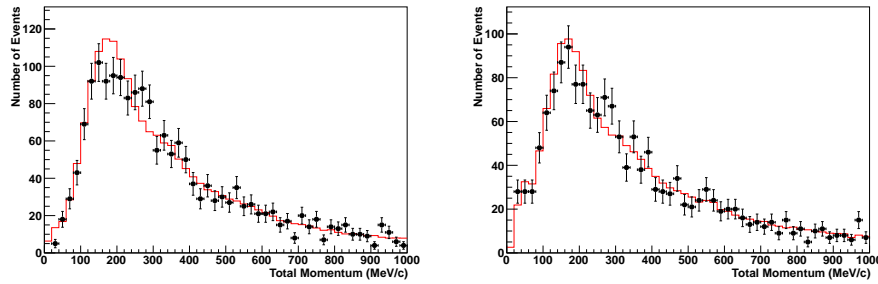


Figure 7.22: Distributions of the total momentum of fitQun (left) and APfit (right) for the outside the signal region sample in the SK-IV data (black) and the 500 years atmospheric neutrino MC (red) after applying the selection criteria 1-5. The MC is normalized by the live time of the data.

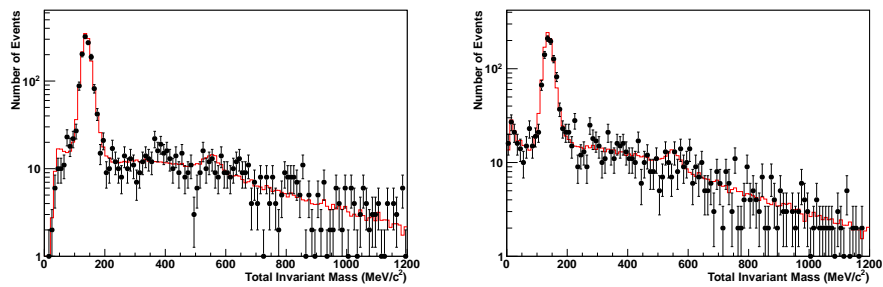


Figure 7.23: Total invariant mass distributions of fitQun (left) and APfit (right) for the outside the signal region sample in the SK-IV data (black) and the 500 years atmospheric neutrino MC (red) after applying the selection criteria 1-5. The MC is normalized by the live time of the data.

7.4 Result

Search for $p \rightarrow e^+\pi^0$ in the 179.5 (163.0) kton-years SK-IV data has been conducted by using fitQun (APfit) with the selection criteria described in Section 7.1. The number of expected background events in the total P_{tot} box for fitQun (APfit) is about 0.14 (0.19) events. No candidate event was found in the data for both fitQun and APfit.

The scatter plots of the 2-dimensional space of the total invariant mass and momentum for the signal MC, the atmospheric neutrino MC and the data in SK-IV are shown in Fig. 7.24 - 7.26. Figure 7.26 demonstrates that fitQun can perform a very clean search for proton decay as well as APfit. In order to compare the shape of the 2D distributions between the data and the MC, we use an estimator L which is defined as a minimum distance between an event point and a vertical line ($M_{\text{tot}} = 938.3 \text{ MeV}/c^2$, $0 \leq P_{\text{tot}} \leq 250 \text{ MeV}/c$) in the 2D space. The good agreement in the 2D distribution for both fitQun and APfit can be seen in Figure 7.27. The event reduction plots are shown in Figure 7.28, our MC reproduces the characteristics of the data well.

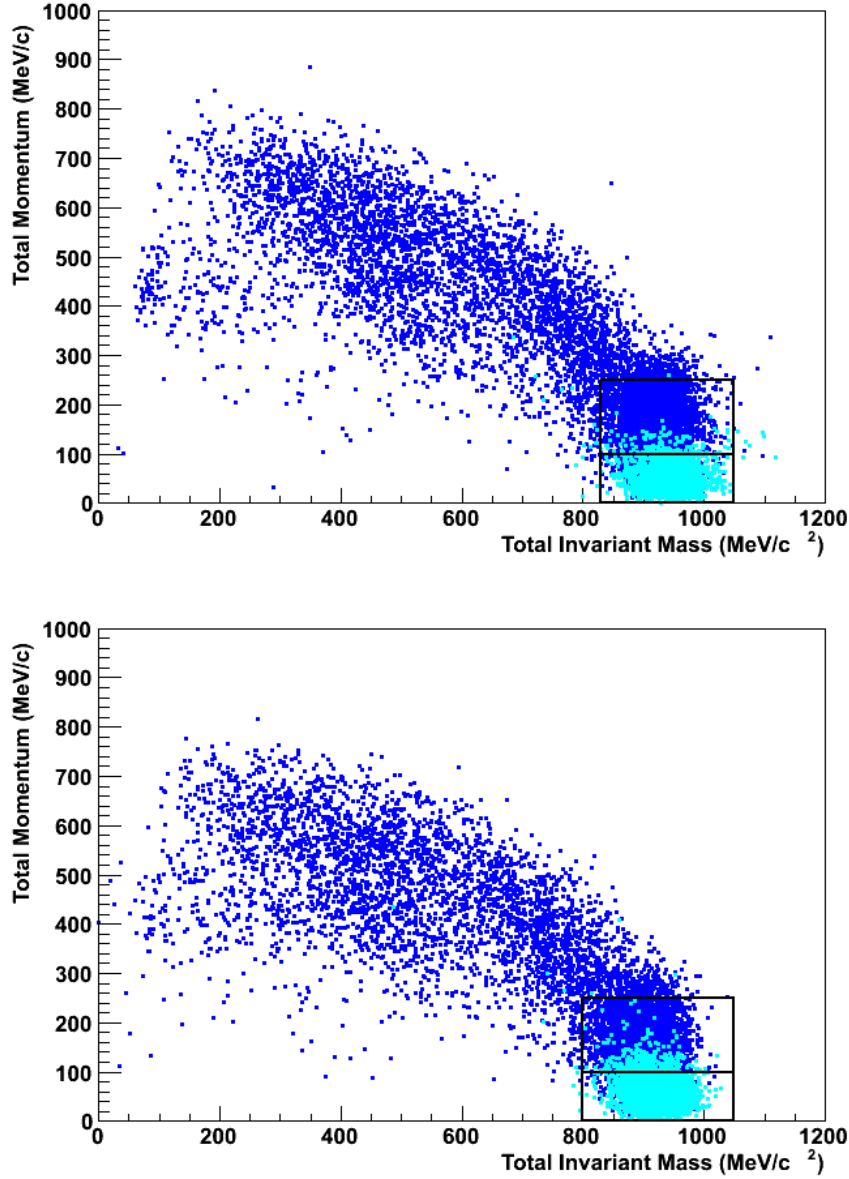


Figure 7.24: Total invariant mass and momentum scatter plots for the $p \rightarrow e^+\pi^0$ MC in SK-IV after applying the selection criteria 1-5 and 7. The top (bottom) figure is for fitQun (APfit). The light (dark) blue shows free (bound) proton decay events. The two boxes correspond to the $P_{\text{tot}} < 100$ MeV/c region (lower box) and $100 \leq P_{\text{tot}} < 250$ MeV/c region (upper box).

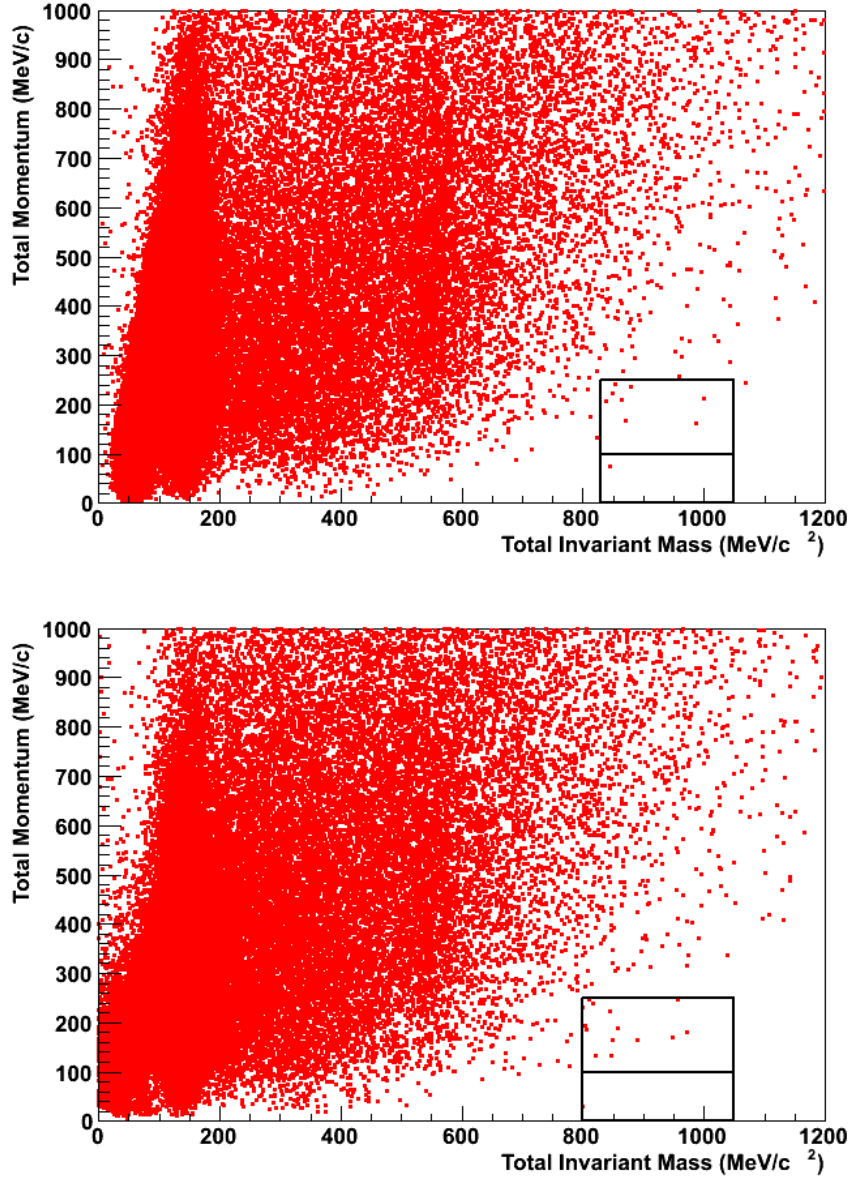


Figure 7.25: Total invariant mass and momentum scatter plots for the 500 years-live-time atmospheric neutrino MC in SK-IV after applying the selection criteria 1-5 and 7. The top (bottom) figure is for fitQun (APfit). The two boxes correspond to the $P_{\text{tot}} < 100$ MeV/c region (lower box) and $100 \leq P_{\text{tot}} < 250$ MeV/c region (upper box).

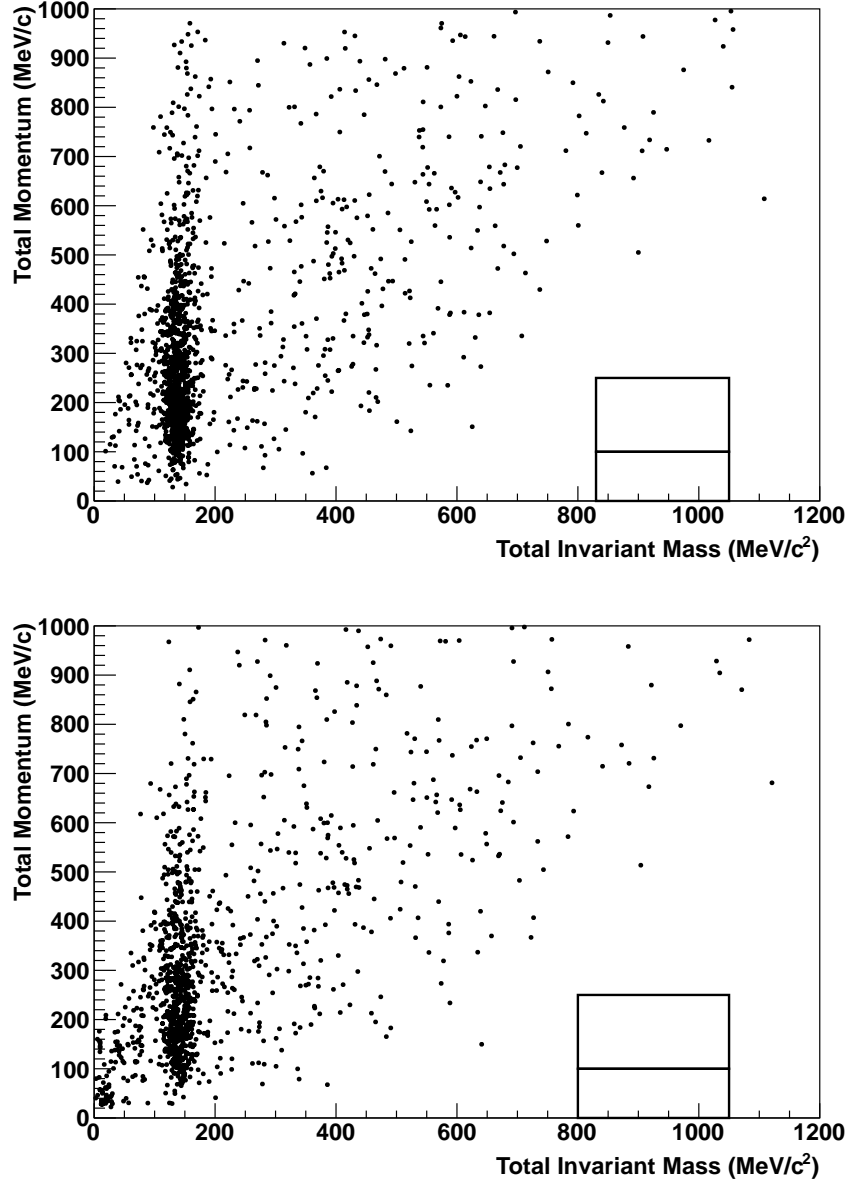


Figure 7.26: Total invariant mass and momentum scatter plots for the FC data set in SK-IV after applying the selection criteria 1-5 and 7. The top (bottom) figure is the result of the 179.5 kton-years data (163.0 kton-years data) with fitQun (APfit). The two boxes correspond to the $P_{\text{tot}} < 100$ MeV/c region (lower box) and $100 \leq P_{\text{tot}} < 250$ MeV/c region (upper box).

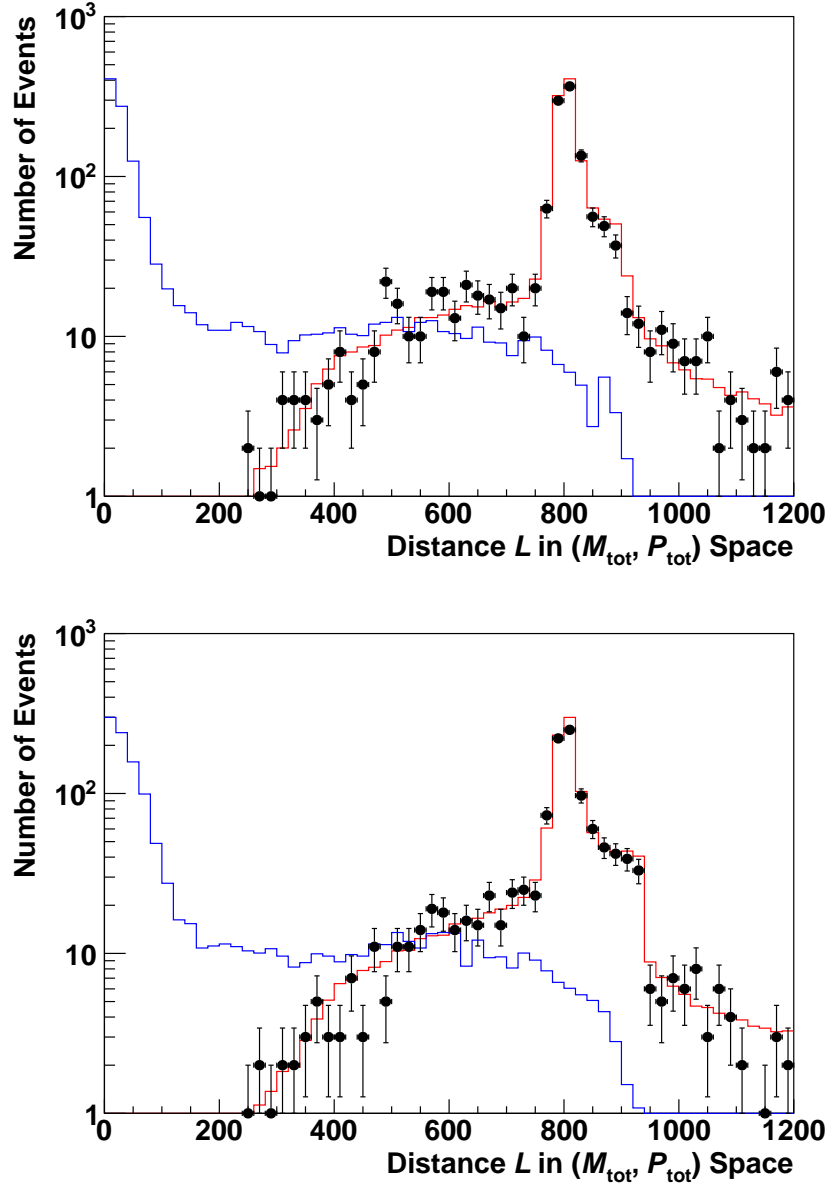


Figure 7.27: Distributions of the distance L in SK-IV after applying the selection criteria 1-5 and 7. The top (bottom) figure is for fitQun (APfit). The black points, red and blue histograms correspond to the FC data, the 500 years-live-time atmospheric neutrino MC and the $p \rightarrow e^+ \pi^0$ MC, respectively. The atmospheric neutrino MC is normalized by the live time of the data. The signal MC is scaled to the atmospheric neutrino MC.

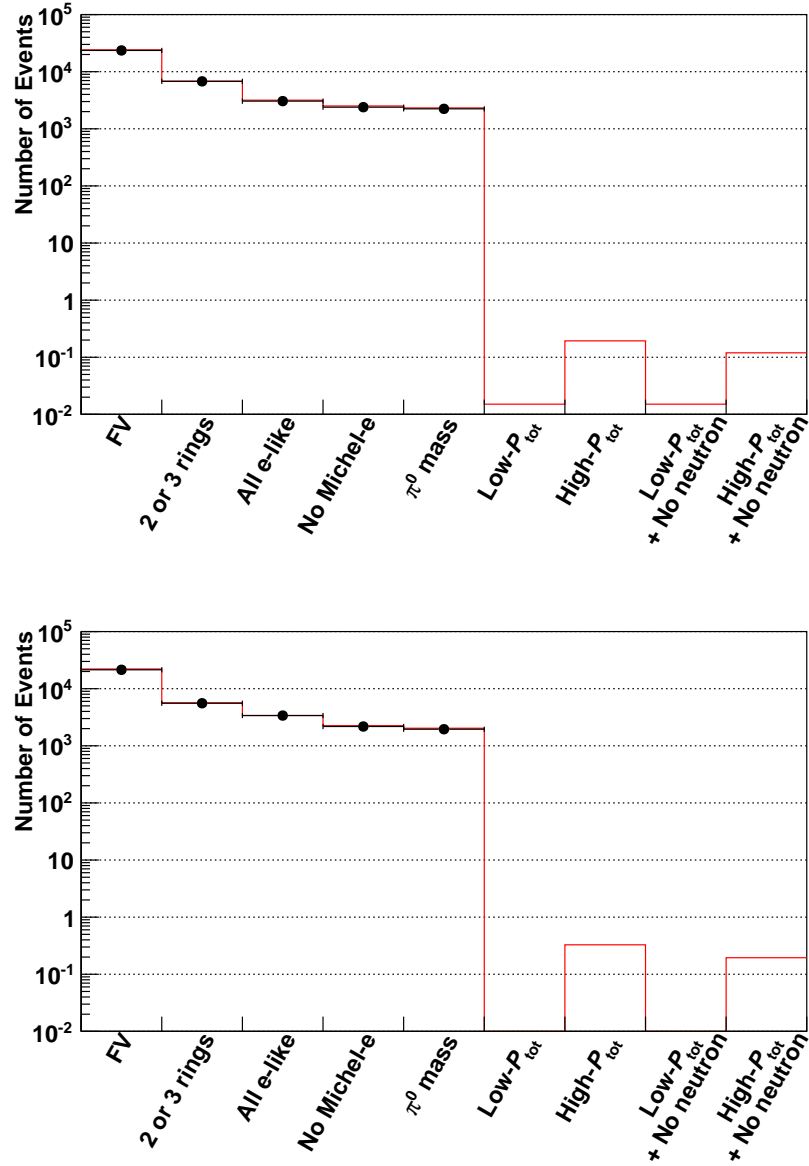


Figure 7.28: Number of events for the FC data set (black points) and the 500 years-live-time atmospheric neutrino MC (red) in SK-IV after each selection criterion. The top (bottom) figure is for fitQun (APfit). The atmospheric neutrino MC is normalized by the live time of the data.

7.5 Lifetime Limit

Although we could not find any candidate events for $p \rightarrow e^+\pi^0$, we can set the lower limit of the proton partial lifetime by using a Bayesian method. Since we have 8 independent searches for $p \rightarrow e^+\pi^0$ ($i = 1 \sim 4$ correspond to the low- P_{tot} box analyses for SK-I to SK-IV, $i = 5 \sim 8$ correspond to the high- P_{tot} box analyses for SK-I to SK-IV), we calculate the lower limit by combining the results. As for the APfit based analysis, the signal efficiencies and the expected background rates for SK-I to SK-III and the systematic errors for SK-I to SK-IV are taken from [1]. The signal efficiencies and the expected background rates for SK-IV and the systematic errors for the SK-IV fitQun based analysis are obtained by using the new MC described in Chapter 4.

The probability of detecting n events is given by a Poisson statistics if the decay rate Γ (> 0), the exposure λ_i (> 0), the signal efficiency ϵ_i ($0 < \epsilon_i < 1$) and the number of background b_i (> 0) are known.

$$P(n_i|\Gamma\lambda_i\epsilon_i b_i) = \frac{e^{-(\Gamma\lambda_i\epsilon_i+b_i)}(\Gamma\lambda_i\epsilon_i+b_i)^{n_i}}{n_i!} \quad (7.8)$$

Applying Bayes' theorem to this probability, we get the following formulas.

$$P(\Gamma\lambda_i\epsilon_i b_i|n_i)P(n_i) = P(n_i|\Gamma\lambda_i\epsilon_i b_i)P(\Gamma\lambda_i\epsilon_i b_i) \quad (7.9)$$

$$= P(n_i|\Gamma\lambda_i\epsilon_i b_i)P(\Gamma)P(\lambda_i)P(\epsilon_i)P(b_i) \quad (7.10)$$

Here, we use that the decay rate, the exposure, the signal efficiency and the number of background are independent. The probability density function of the decay rate is given as follows;

$$P(\Gamma|n_i) = \iiint P(\Gamma\lambda_i\epsilon_i b_i|n_i)d\epsilon_i d\lambda_i db_i \quad (7.11)$$

$$= \frac{1}{A_i} \iiint \frac{e^{-(\Gamma\lambda_i\epsilon_i+b_i)}(\Gamma\lambda_i\epsilon_i+b_i)^{n_i}}{n_i!} P(\Gamma)P(\epsilon_i)P(\lambda_i)P(b_i)d\epsilon_i d\lambda_i db_i, \quad (7.12)$$

where the normalization constant A_i is,

$$A_i = \int_0^\infty P(\Gamma|n_i)d\Gamma. \quad (7.13)$$

We assume the probability of the decay rate is uniform and the probabilities $P(\lambda_i)$ and $P(\epsilon_i)$ are defined as a Gaussian;

$$P(\Gamma) = 1, \quad (7.14)$$

$$P(\lambda_i) \propto e^{-(\lambda_i-\lambda_{0i})^2/2\sigma_{\lambda_i}^2} \quad (7.15)$$

and

$$P(\epsilon_i) \propto e^{-(\epsilon_i-\epsilon_{0i})^2/2\sigma_{\epsilon_i}^2}, \quad (7.16)$$

where λ_{0i} (σ_{λ_i}) and ϵ_{0i} (σ_{ϵ_i}) are the estimations (systematic errors) of the signal efficiency and the exposure, respectively. In order to take into account the statistical error of the number of background, we use a convolution of Poisson and Gaussian distributions for the probability of the number of background as follows;

$$P(b_i) \propto \int_0^\infty \frac{e^{-B} B^{n_{bi}}}{n_{bi}!} e^{-(C_i b_i - B)^2 / 2\sigma_{b_i}^2} dB, \quad (7.17)$$

where n_{bi} is the number of background events in the 3000 (500) years MC for SK-IV (SK-I to SK-III), C_i is a constant to normalize the MC live time to the data live time and σ_{b_i} is the systematic error of the number of background. The lower limit of the decay rate, Γ_{limit} , at 90% confidence level is given by,

$$0.9 = \int_{\Gamma=0}^{\Gamma_{\text{limit}}} \prod_{i=1}^{N=8} P(\Gamma|n_i) d\Gamma. \quad (7.18)$$

Then, the lower limit of the partial lifetime of $p \rightarrow e^+\pi^0$ is calculated as follows.

$$\tau/B_{p \rightarrow e^+\pi^0} = \frac{1}{\Gamma_{\text{limit}}} \quad (7.19)$$

By using only the SK-IV data, we obtain the lower partial lifetime limit of $p \rightarrow e^+\pi^0$ for the APfit based analysis as,

$$\tau/B_{p \rightarrow e^+\pi^0} = 8.58 \times 10^{33} \text{ years at 90\% C.L.}, \quad (7.20)$$

and for the fitQun based analysis as,

$$\tau/B_{p \rightarrow e^+\pi^0} = 9.47 \times 10^{33} \text{ years at 90\% C.L.} \quad (7.21)$$

The lower partial lifetime limit of $p \rightarrow e^+\pi^0$ can be calculated by using the results of the APfit based analyses for the SK-I to SK-IV data as,

$$\tau/B_{p \rightarrow e^+\pi^0} = 1.79 \times 10^{34} \text{ years at 90\% C.L.} \quad (7.22)$$

Finally, we conclude the lower partial lifetime limit of $p \rightarrow e^+\pi^0$ by combining the APfit based analysis for the SK-I to SK-III data with the fitQun based analysis for the SK-IV data as,

$$\tau/B_{p \rightarrow e^+\pi^0} = 1.88 \times 10^{34} \text{ years at 90\% C.L.} \quad (7.23)$$

This lifetime limit is 18% longer than that of the latest published paper (1.6 \times 10³⁴ years) [1].

Chapter 8

Discussion

8.1 Comparison with GUT models

We discussed several attractive GUT models in Chapter 2, the predictions of the proton partial lifetime for $p \rightarrow e^+ \pi^0$ are rewritten as follows [9, 14, 22, 23].

$$\text{Minimal } SU(5) : 10^{31 \pm 1} \text{ years} \quad (8.1)$$

$$\text{Minimal SUSY } SU(5) : > 4.1 \times 10^{33} \text{ years} \quad (8.2)$$

$$\text{Minimal } SO(10) : 10^{32} - 10^{39} \text{ years} \quad (8.3)$$

In contrast to these predictions, we obtain the world best experimental limit by replacing the reconstruction algorithm applied to the half of the data set from APfit to fitQun as,

$$\tau/B_{p \rightarrow e^+ \pi^0} = 1.88 \times 10^{34} \text{ years at 90\% CL.} \quad (8.4)$$

By this result, we can reconfirm that the minimal $SU(5)$ model is completely ruled out. Note that this conclusion can be derived only from the fitQun result and it is not trivial in case of a new reconstruction algorithm. This experimental result excludes part of the predicted regions of both the minimal SUSY $SU(5)$ and minimal $SO(10)$.

In order to estimate how much our energy frontier is expanded, we can roughly write down the lifetime assuming the mass of a mediated boson M_X is enough large as,

$$\tau_p \sim \frac{1}{\alpha_G^2} \frac{M_X^4}{m_p^5}. \quad (8.5)$$

where α_G is the coupling constant at the GUT scale. Assuming $\alpha_G = 40^{-1}$ by looking at Figure 2.2, the lower limit of the GUT energy scale is obtained as follow.

$$M_X \gtrsim 4.5 \times 10^{15} \text{ GeV} \quad (8.6)$$

This corresponds to the length of 4.4×10^{-32} m (the Planck scale is 1.62×10^{-35} m). This experimental limit is the highest energy frontier for humanity measured on the earth at this moment.

8.2 Further Improvements for fitQun

In this section, we discuss about possibilities of further improvements for fitQun. The dominant background for $p \rightarrow e^+\pi^0$ are ν_e CC events leaving a primary e^\pm and 2γ s from a π^0 in final state. On the other hand, NC events can mimic such an event topology by generating $2\pi^0$ s (NC $2\pi^0$) when one of four gammas from them does not have enough energy to produce a visible ring for the fitter. The ring counting of fitQun tends to find more rings compared to that of APfit and thus fitQun can reject more NC $2\pi^0$ events by correctly finding all rings. An example of a NC $2\pi^0$ event which is a background event for the APfit based analysis in SK-IV but not for fitQun is displayed in Figure 8.1. In this figure, it can be seen that fitQun found all four e-like rings (APfit did not reconstruct the larger ring in the top). However, as shown in Table 7.3, there are remaining background NC events. Figure 8.2 shows an example of such events, the ring counting of fitQun did not work well for this event (a similar situation can be found in APfit). Therefore, it may be possible to achieve an analysis with no NC background event by improving the ring counting algorithm in fitQun.

Since fitQun is the maximum likelihood fitter, it may be natural to construct a $p \rightarrow e^+\pi^0$ hypothesis likelihood and conduct a likelihood analysis. For example, if we use a three-e-like-ring hypothesis while fixing a π^0 mass for signal events instead of the multi-ring hypothesis, it is naively expected to have better momentum resolution and thus a higher signal efficiency. In order to establish a likelihood analysis by using such a dedicated likelihood fitter, we need a larger statistics of the atmospheric neutrino MC to estimate the likelihood distribution for background events because the background rate should be very small for a $p \rightarrow e^+\pi^0$ search. However, the process of the fitter will take unrealistic time if we want to generate an over-thousand-years full MC. For that purpose, the preselected method described in Appendix D will be useful to extract the events of interest.

8.3 Discovery Potential in Future

Although we may observe proton decay in SK in future, it is necessary to have a bigger detector in order to determine a correct GUT model by measuring the branching ratios for many proton decay modes. The Hyper-Kamiokande (HK) project is proposed as a next generation water Cherenkov detector [101] (Figure 8.3). The detector consists of a cylindrical stainless tank, 258 kton ultra-pure light water and 40,000 20-inch PMTs (40% photocoverage). The fiducial volume is 187 kton (178 kton) when we use a region of $D_{\text{wall}} > 1.5$ (2.0) m. In HK, it is expected to use a new type of photosensor which has

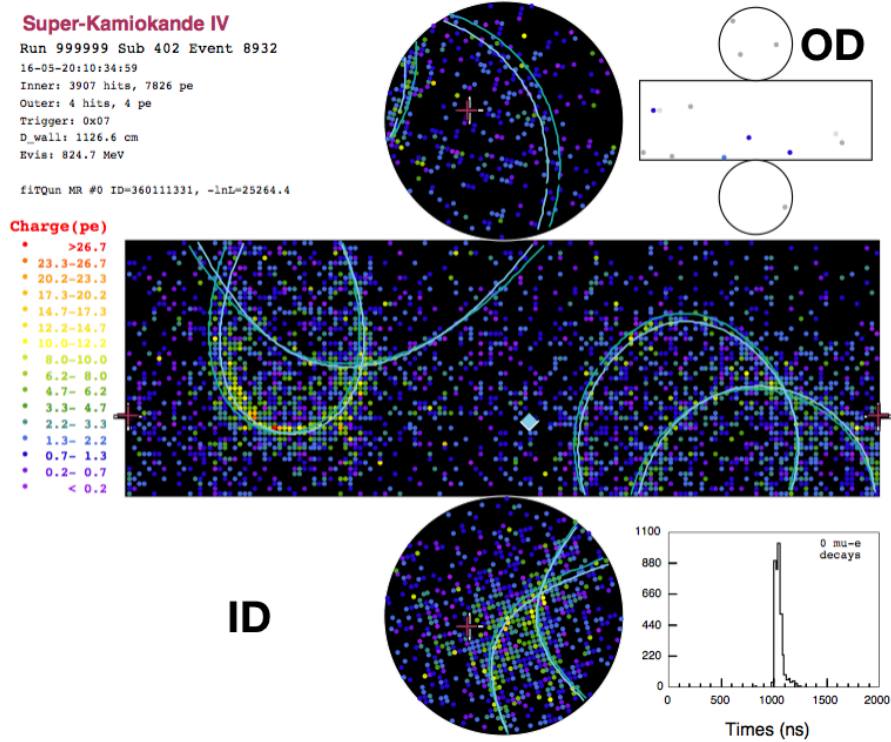


Figure 8.1: Typical $\text{NC}2\pi^0$ event display in the SK-IV atmospheric neutrino MC. The four solid blue (green) lines are the fitQun reconstructed e -like rings (MC true shower rings from gammas). FitQun found all four rings whereas APfit did not reconstruct the larger ring in the top.

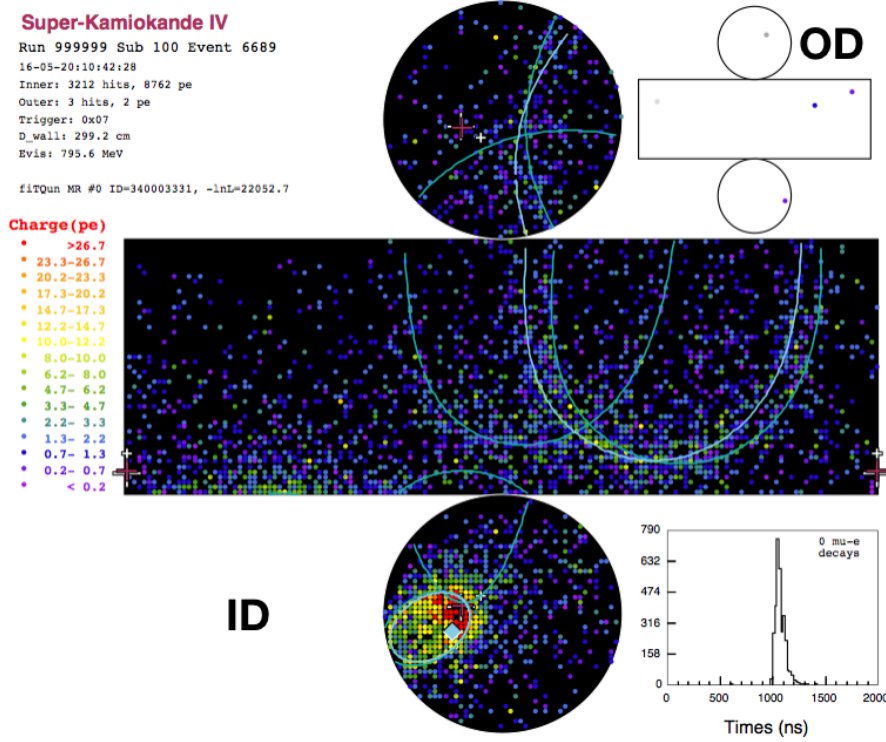


Figure 8.2: A $\text{NC}2\pi^0$ event display in the SK-IV atmospheric neutrino MC. The four solid blue (green) lines are the fitQun reconstructed e -like rings (MC true shower rings from gammas). FiTQun failed to reconstruct two of four true rings (APfit also failed).

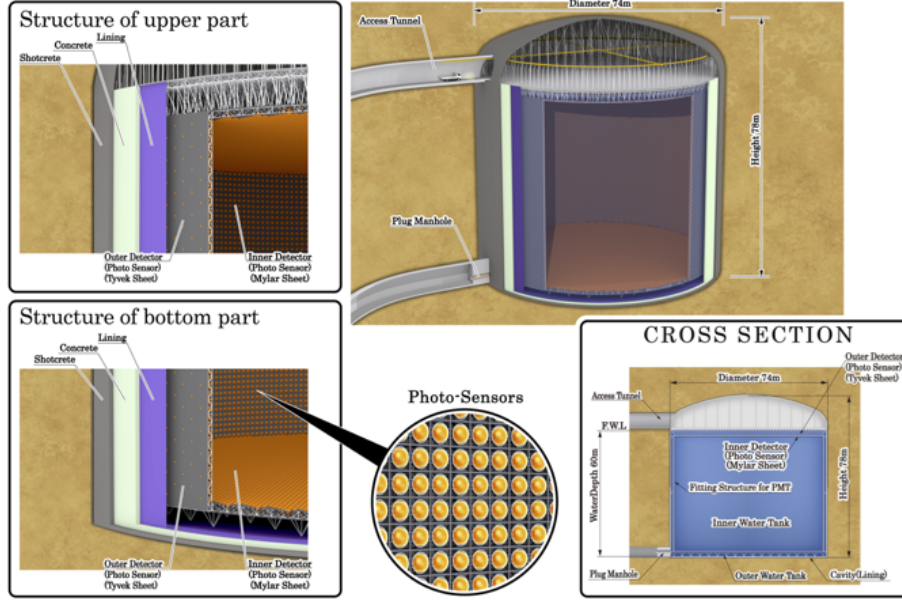


Figure 8.3: Schematic view of the Hyper-Kamiokande detector. Taken from [101].

better performance than that of the SK PMT.

In principle, fiTQun is expected to work on HK since HK is a natural extension of SK. However, it should be taken into account of the difference of PMTs and so on. In the following sentence, we discuss advantages to use fiTQun in both SK and HK by comparing a discovery potential of $p \rightarrow e^+\pi^0$ for both APfit ($D_{\text{wall}} > 2.0$ m) and fiTQun ($D_{\text{wall}} > 1.5$ m) assuming the HK performance is the same as SK-IV whose photocoverage is the same as that of HK. Here, we adopt the two-box analysis for both SK and HK.

The discovery potential for $p \rightarrow e^+\pi^0$ is calculated by using the profile likelihood ratio method [102]. A test statistic q_0 is defined as the log likelihood ratio between the null hypothesis (background-only) and the signal hypothesis (signal+background);

$$q_0 = \begin{cases} -2 \ln \frac{L(0, \hat{\hat{\theta}})}{L(\hat{\mu}, \hat{\theta})} & \hat{\mu} \geq 0 \\ 0 & \hat{\mu} < 0 \end{cases} \quad (8.7)$$

where $\hat{\mu}$ is the signal strength which means the decay rate Γ in this case. θ is a nuisance parameter while $\hat{\mu}$ is a parameter of interest. The null hypothesis likelihood in the numerator is maximized by an estimator $\hat{\hat{\theta}}$, whereas the signal

hypothesis one in the denominator is maximized by an estimator $\hat{\theta}$. That is,

$$L(\Gamma, \hat{\theta}) = \prod_{i=0}^N \frac{(S_i + B_i)^{n_i}}{n_i!} \times \frac{1}{2\pi\sigma_{\text{eff},i}^2\sigma_{\text{bkg},i}^2} \exp\left(-\frac{\theta_{\text{eff},i}^2}{2\sigma_{\text{eff},i}^2} - \frac{\theta_{\text{bkg},i}^2}{2\sigma_{\text{bkg},i}^2}\right), \quad (8.8)$$

where N is the number of analysis bins for each total momentum box and each SK, $\sigma_{\text{eff},i}$ ($\sigma_{\text{bkg},i}$) and $\theta_{\text{eff},i}$ ($\theta_{\text{bkg},i}$) are the systematic error and its nuisance parameter for the signal efficiency (number of background) in the i -th bin. The expected number n_i is given as $S_i + B_i$, where $S_i = \Gamma\lambda_i\epsilon_i \times (1 + \theta_{\text{eff},i})$ and $B_i = b_i \times (1 + \theta_{\text{bkg},i})$. The probability function of q_0 for the $\mu = 0$ case is given as,

$$f(q_0|0) = \frac{1}{2}\delta(q_0) + \frac{1}{2\sqrt{2\pi}}\frac{1}{\sqrt{q_0}}\exp\left(-\frac{q_0}{2}\right) \quad (8.9)$$

Using the cumulative distribution of Equation 8.9, Φ , the p-value of the null hypothesis is then calculated as,

$$p_0 = 1 - \Phi(\sqrt{q_0}) \quad (8.10)$$

By using Equation 8.10, the median significance for the signal hypothesis can be calculated.

The 3σ discovery corresponding proton partial lifetime as a function of live time is obtained for both SK and HK as shown in Figure 8.4-8.5. As for the APfit based analysis, the signal efficiencies and expected background rates for SK-I to SK-III and the systematic errors for SK-I to SK-IV are taken from [1]. The signal efficiencies and expected background rates for SK-IV and the systematic errors for the SK-IV fitQun based analysis are obtained by using the new MC described in Chapter 4. At the point of the 30th year of exposure of SK (after 15 years of exposure from today), the APfit based analysis can approach at 3.14×10^{34} years while the combined analysis (APfit for SK-I to SK-III and fitQun for SK-IV) can approach at 3.48×10^{34} years which is 11% higher sensitivity. After 30 years of exposure of HK (solid lines), the APfit based analysis can approach at 1.46×10^{35} years while the fitQun based analysis can approach at 1.56×10^{35} years which is 7% higher sensitivity. There may be a possibility to construct a second HK tank which has the same configuration as the first one after six years of the one tank operation. If we consider such a two tank operation, the fitQun (APfit) based analysis can approach at 2.30 (2.16) $\times 10^{35}$ years after 30 years of exposure of HK (dotted lines).

Once fitQun is able to work for the whole SK period properly, the discovery potential of the full fitQun based analysis is expected to much better. As an example of the full fitQun based analysis, we calculate the 3σ discovery potential assuming the performance (signal efficiency, background rate and systematic errors) in SK-I to SK-III to be the same as that of SK-IV as shown in Figure 8.4 (green line) get the value of 3.91×10^{34} years after 30 years of exposure.

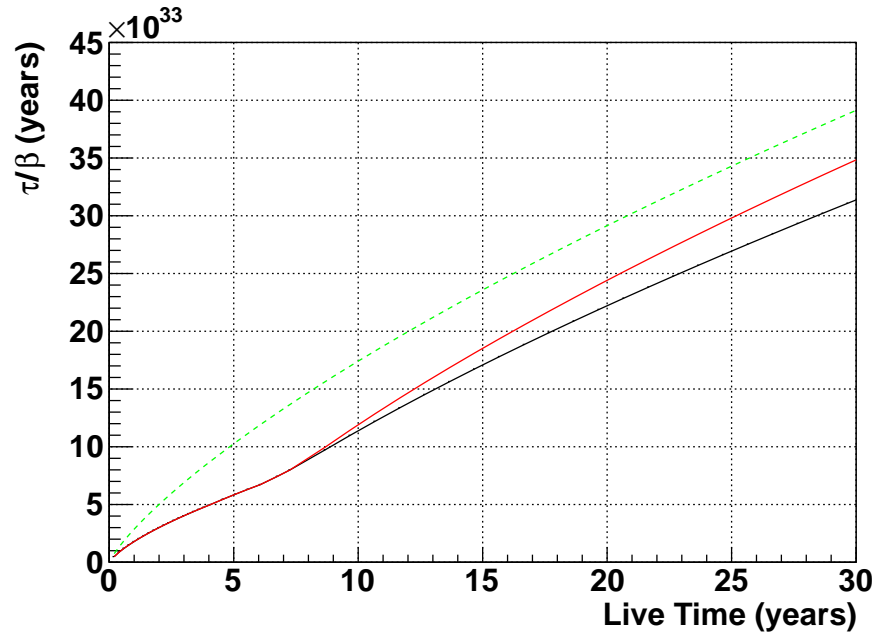


Figure 8.4: 3σ discovery potential for $p \rightarrow e^+\pi^0$ in SK as a function of live time. Each line shows the different analysis; Black: SK-I to SK-IV based on APfit, Red: SK-I to SK-III based on APfit and SK-IV based on fitQun, Green: SK-IV based on fitQun. In this thesis, we stand on the point of 14.9 years in SK.

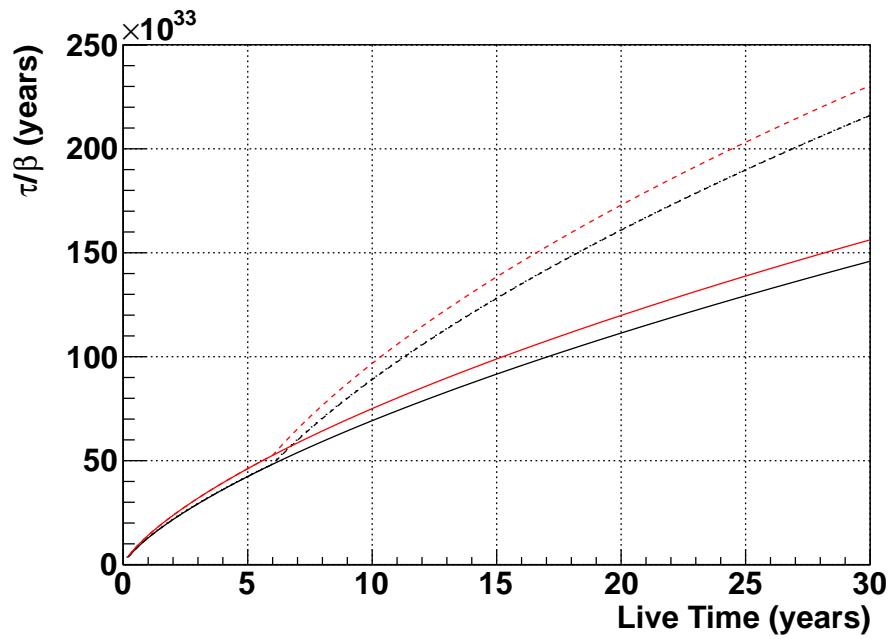


Figure 8.5: 3σ discovery potential for $p \rightarrow e^+\pi^0$ in HK as a function of live time. Black (Red) line shows the HK based on APfit (fiTQun) assuming its performance is the same as that of SK-IV. Dotted lines show the HK two tank operation assumed to start after six years of the one tank operation.

It may become a long journey for mankind to discover proton decay, but it is just a moment for protons. If we really want to know the deep inside of nature, we must keep observation and improve our detectors and techniques in a long-term strategy.

Chapter 9

Conclusion

A proton decay search for $p \rightarrow e^+\pi^0$ using the improved event reconstruction algorithm in Super-Kamiokande was discussed. We have newly developed the new event reconstruction algorithm, fitQun, based on the maximum likelihood method. This is the first time to change the concept of the event reconstruction for SK proton decay analyses. We choose $p \rightarrow e^+\pi^0$ as a first application of fitQun based proton decay analyses since this decay mode is the most dominant in many non-SUSY GUTs and the most sensitive in SK. In this thesis, we applied fitQun for the SK-IV data whose live time is almost half of the entire SK live time.

In the signal MC study, fitQun shows better performance compared to the conventional algorithm, called APfit. While keeping the same level of the signal efficiency as APfit, the fiducial volume of fitQun is defined as 24.7 kton which is 10% higher than that of APfit. One may expect signal candidates will be found in this unexplored volume region by using fitQun instead of APfit. The three ring fraction of fitQun (APfit) for free proton decay events is 77.5% (60.5%). The total invariant mass peak and its width of fitQun (APfit) for free proton decay events are 941.7 MeV/c² (921.4 MeV/c²) and 27.6 MeV/c² (30.2 MeV/c²), respectively. Thanks to this better mass reconstruction performance of fitQun, we can reduce the atmospheric neutrino background rate about -30% compared to APfit by applying the tighter total invariant mass cut (800 ~ 1050 MeV/c² → 830 ~ 1050 MeV/c²). After the proper calibrations for both the data and fitQun was done, fitQun's energy scale and detector non-uniformity error became similar to those of APfit (energy scale: 2.1% (2.1%), non-uniformity: 1.0% (0.9%) for fitQun (APfit)). The new electronics, QBEE, employed in SK-IV enabled us to reduce the background by approximately half using the neutron tagging technique.

We have searched for $p \rightarrow e^+\pi^0$ in the 179.5 kton·years FC data taken in SK-IV from Sep. 2008 to Aug. 2016 by using fitQun. Since the latest published paper [1], 483 live days data were added from 4973 live days to 5456 live days (including the SK-I to SK-III data). For more accurate background estimation, we newly generated and used the 2500 years atmospheric neutrino MC with the

pre-selection for $p \rightarrow e^+\pi^0$, in addition to the conventional 500 years MC. In the total signal region (=low- P_{tot} box + high- P_{tot} box), the signal efficiency and number of expected background events are about 38% and 0.14 events, respectively. Unfortunately, no signal candidate was found in our data. Then, the lower partial lifetime limit of $p \rightarrow e^+\pi^0$ for the fitQun based analysis can be calculated by using Bayes' theorem as 9.47×10^{33} years at 90 % C.L. This limit is 10% longer than that of the APfit based analysis (8.58×10^{33} years), mainly due to the larger fiducial volume of fitQun. Finally, we combined the APfit results for SK-I to SK-III (172.5 kton-years) [1] and the fitQun result for SK-IV, the lower lifetime limit is given as,

$$\tau/B_{p \rightarrow e^+\pi^0} = 1.88 \times 10^{34} \text{ years at 90\% C.L.}$$

This lower lifetime limit is 18% longer than that of the latest published SK paper (1.6×10^{34} years [1]) and thus the most stringent constraint on non-SUSY GUTs in the world.

Appendix A

Special Handling for the Blasting in the Mine

During May 7th to Aug. 4th in 2015, the blasting work was conducted in the Kamioka mine for constructing a room of a new water system for SK-Gd project. The location of the blasting point is about 100 m away from the SK site. The total number of blasting is 132 times and the blasting timing is recorded by a person in charge of the Kamioka Mining and Smelting Company.

By eye-scanning the final FC data sample, we noticed that there are two flasher events coincided with the blasting moments, which survived several flasher rejection algorithms in the FC reduction (Fig. A.1). Figure A.2 shows some FC reduction output rates as a function of the time difference between the SK DAQ time and the blasting time (top left: FC 3rd reduction output, top right: Rejected events in FC 4th reduction, bottom left: FC 5th reduction output, bottom right: FCFV output). From these figures, it is obvious that the blasting work caused flasher events although the mechanism is unknown (shaking the tank, fluctuating the grounding etc). In the top left figure, the peak position and width are fitted to be -39 s and 61 s by a function of $f(t) = p_0 \times \exp[-(t-p_1)^2/(2p_2)^2] + p_3$, respectively. The non-zero peak position is considered to be due to the systematic time gap between SK and the mine company.

Since the mechanism of flasher is uncertain, we decided not to use the data which recorded at a time between -500 s and 400 s from the blasting time in any high energy analysis for the sake of cleanness of the data set. The dead time due to this handling is about 1.4 days (~ 11 FC neutrino events).

APPENDIX A. SPECIAL HANDLING FOR THE BLASTING IN THE MINE

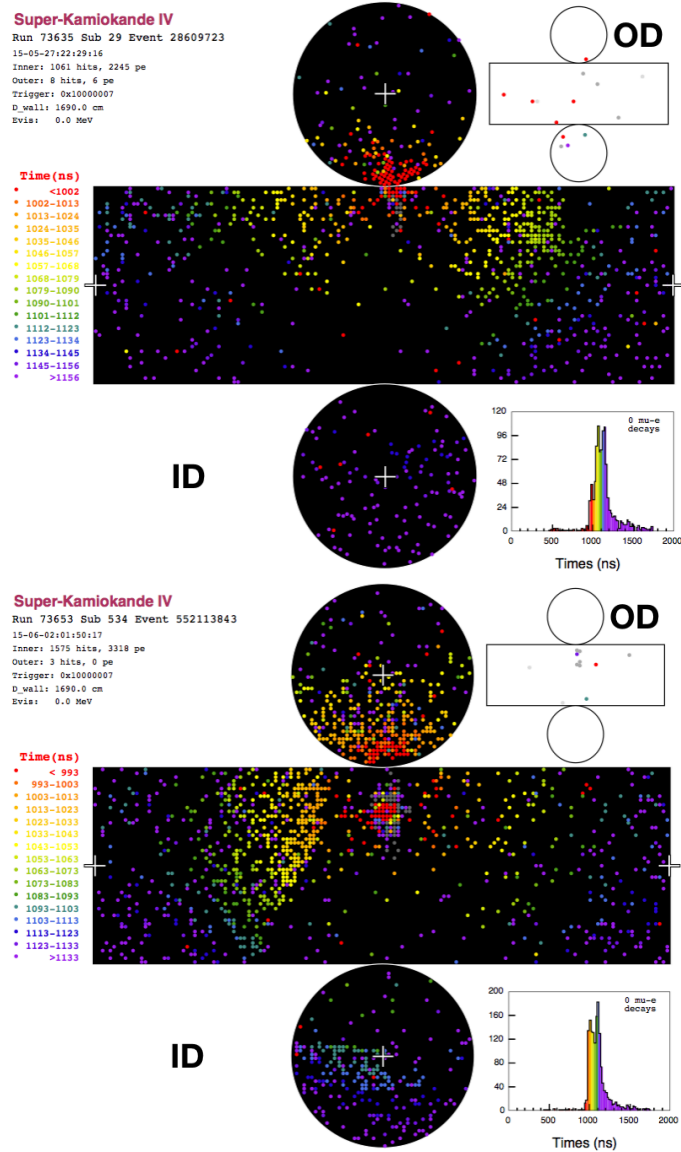


Figure A.1: Flasher events coincided with the blasting moments. The color indicates the hit timing (red: early hit, blue: late hit). The top (bottom) event happened at May 27th, 2015 at 22:29 JST (June 2nd, 2015 at 01:50 JST), it is the same time as the nearby blasting moment.

APPENDIX A. SPECIAL HANDLING FOR THE BLASTING IN THE MINE

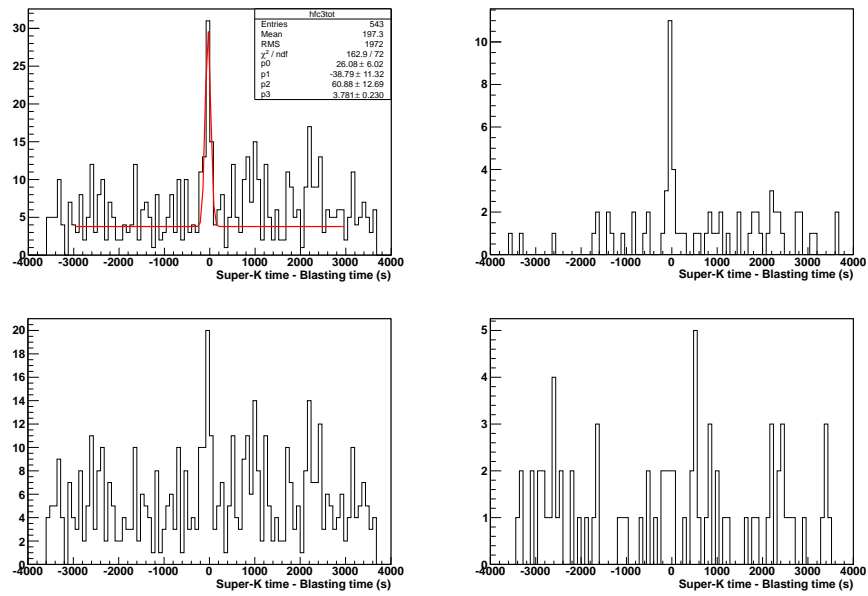


Figure A.2: Some FC reduction output rates as a function of the time difference between the SK DAQ time and the blasting time. Top left: FC 3rd reduction output, top right: Rejected event in FC 4th reduction, bottom left: FC 5th reduction output, bottom right: FCFV output.

Appendix B

Time Variation of PMT Hit Rate

It is empirically known that the PMT hit rate has a time dependence and its variation varies depending on the detector period. Since the PMT gain is increasing but the hit threshold does not change, there might include such a threshold effect in the change of the PMT hit rate. However, if we compare the PMT hit distributions with different time periods, it appears that the distribution shape does not change but the number of hits is increased (Fig. B.1). Thus, it seems that the dark rate of PMTs has been also changing. In any case, those PMT hit rate change will affect to physics analysis in particular for low energy events. As described Appendix C, the reconstructed momentum of Michel electrons changed in time due to the PMT hit rate change. In order to correct such effect, the PMT hit rate plot as a function of time is necessary. Also, it is worth to make it since there was no time variation plot of the hit rate with a consistent estimation method for whole SK period.

For the time variation plot of the PMT hit rate, the stopping muon data sample was used because it is well understand and available in whole SK period. First of all, the stopping muon fitter was applied to the data. Using the reconstructed entering point of muons, the time-of-flight subtracted hit timing distribution can be made (Fig. B.2). Then, the early off timing hits in a 100 ns (250 ns) time window for SK-I to SK-III (for SK-IV) are counted up. The time window is set to be a sufficiently flat area. Finally, the run-by-run averaged hit rate is estimated by the following formula.

$$\text{PMT hit rate (kHz)} = \sum_i^n \frac{\text{nHIT}_i}{T \times \text{nEV}_i \times (\text{nPMT} - \text{nBAD}_i)} \times 10^6 \quad (\text{B.1})$$

where nHIT_i is the number of hits in the i -th run in the time window T , nEV_i is the number of events in the i -th run, nPMT is the number of ID PMTs and nBAD_i is the number of bad ID PMTs on average in the i -th run. Figure B.3 shows the time variation of the averaged PMT hit rate for whole SK period. The

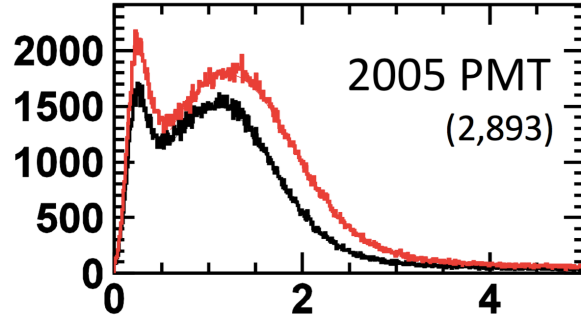


Figure B.1: Hit charge distributions for a PMT set of a same production year (the hit charge (p.e.s) vs. the number of events). Black histogram is for the period from Dec. 2008 to Jan. 2009. Red histogram is for the period on Mar. 2015. Taken from a SK internal document.

PMT hit rate is increasing as a whole although there is variation. A significant decrease in SK-II can be seen, it is thought that it is due to the decay of a flash light rate caused by a chemical reaction in the FRP case. That flasher from the FRP case seems to be defeated by the other hit rate source at around 2008. The gap between the end point of SK-II and the start point of SK-III might be due to the tank opening, it activated the dark rate of PMTs. The replacement of electronic boards is the reason why the gap between the end point of SK-III and the start point of SK-IV happened.

An application of the time dependent PMT hit rate for fitQun is shown in Appendix C.

APPENDIX B. TIME VARIATION OF PMT HIT RATE

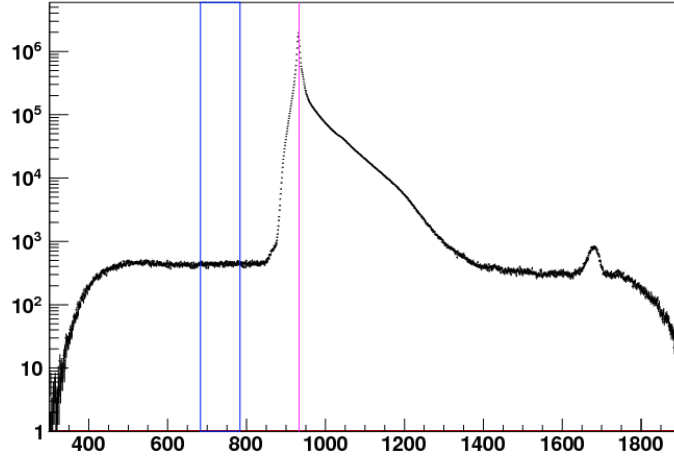


Figure B.2: Time-of-flight subtracted hit timing distribution for SK-II (the hit timing (ns) vs. the number of events). Magenta line shows the peak position and two blue lines indicate the time window. The peak around 1700 ns is due to the signal reflection between a PMT and an ATM board.

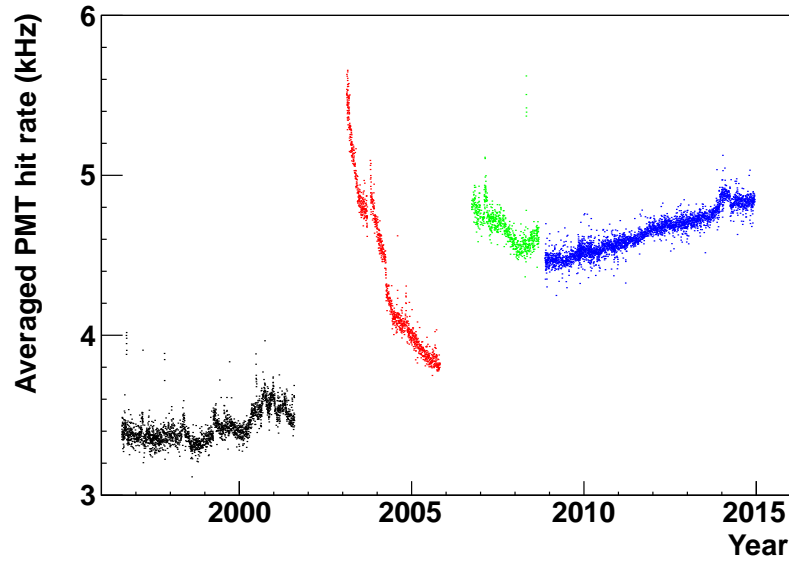


Figure B.3: Time variation of the averaged PMT hit rate from the beginning of SK to mid. 2015. The colors shows the detector periods; black, red, green and blue show SK-I, -II, -III and -IV, respectively.

Appendix C

Development of FiTQun for SK-I to SK-III

Almost half of the observed data in whole SK period at this moment consists of SK-I, II and III data, and there might be proton decay events which were not discovered by APfit. Towards full fitQun-based analysis for SK-I to SK-IV, we have developed fitQun not only for SK-IV but also SK-I to SK-III. By replacing the Cherenkov profiles, the timing distribution, etc., fitQun can work on SK-I to SK-III properly. We have slightly modified the code regarding the data taking by the ATM during the development. After the basic development, MC based performance for SK-I to SK-III became similar to that of SK-IV.

The detector quality had been largely changed over time as described in Section 3.6 and Appendix B, such as the water attenuation length, the PMT gain and dark rate. It affects the reconstructed momentum in data, and then made large data-MC discrepancies. Therefore, the time dependent corrections of the detector variables were implemented to fitQun. Figure C.1 shows the time variation plots of the muon momentum over range (p/range) for the stopping muon data in SK-I with a no correction case, with a PMT gain correction case and with a PMT gain and water attenuation length correction case. After the time dependent corrections, the time dependence of p/range was reduced significantly. In addition to the above corrections, the dark rate correction in time was useful for the low energy reconstruction such as Michel electron momentum. Figure C.2 shows the time variation plots of Michel electrons in the stopping muon sample with the no correction case and with the dark rate correction case. Since the number of hits are low for Michel electrons, the reconstructed momentum is largely affected by the effect of the PMT dark rate. After the dark rate correction, the time dependence of the Michel electron momentum becomes flat.

However, there are still non-negligible data-MC discrepancies for SK-I to SK-III. Figure C.3 shows the PID likelihood ratio ($\ln L_e/L_\mu$) distributions of both the data and MC for the FC sub-GeV single-ring atmospheric neutrino

APPENDIX C. DEVELOPMENT OF FITQUN FOR SK-I TO SK-III

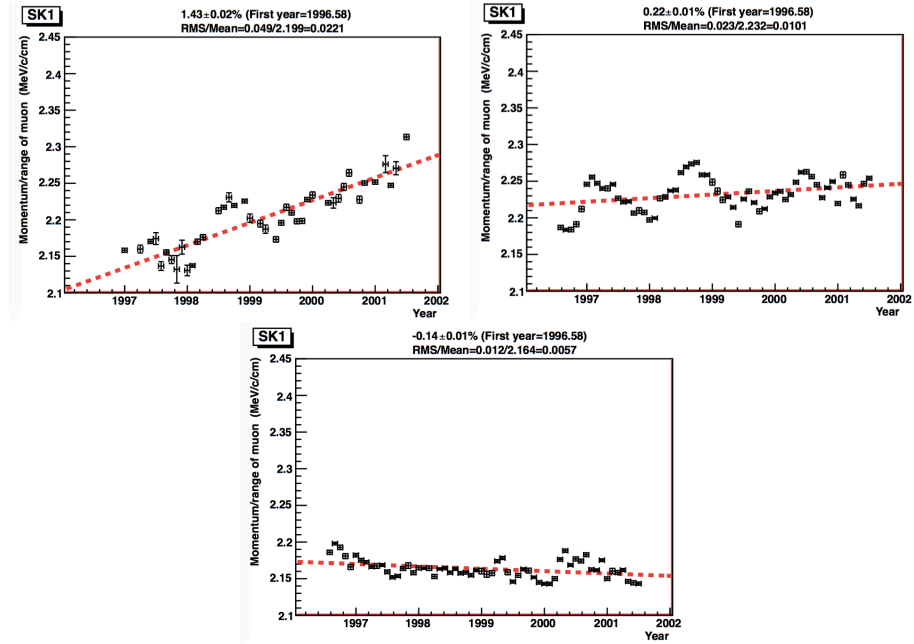


Figure C.1: Time variation plots of the muon momentum over range for the stopping muon data in SK-I. The top left, right and bottom plots are for the no correction case, with the PMT gain correction case and with the PMT gain and water attenuation length correction case. The dotted red lines show linear fitted slopes.

events. The data distributions for SK-I to SK-III shifted to the left (more μ -like) while good agreement of data-MC can be seen in SK-IV. It is considered that these discrepancies come from the time distribution difference between the real PMT response and the MC modeling in the ATM. Although the PMT time distribution is an asymmetric Gaussian, SKDETSIM for SK-I to SK-III (ATM period) assume a symmetric Gaussian. In near future, fitQun will be able to reconstruct all the SK data by improving the detector simulation.

APPENDIX C. DEVELOPMENT OF FITQUN FOR SK-I TO SK-III

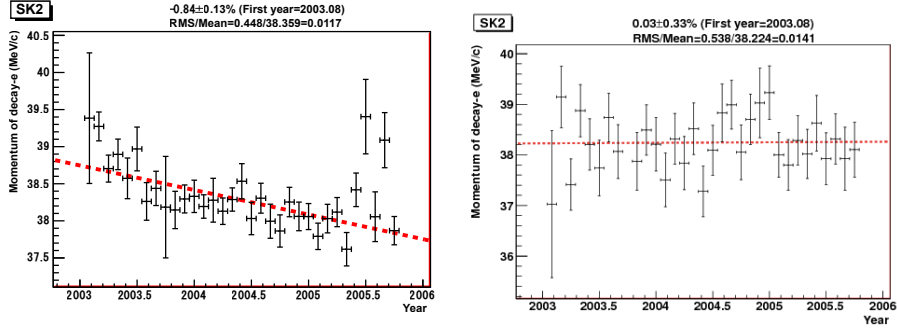


Figure C.2: Time variation of the Michel electron momentum for the stopping muon data in SK-II after the PMT gain and water attenuation length correction. Left (right) figure shows the momentum before (after) the PMT dark rate correction. The dotted red lines show linear fitted slopes.

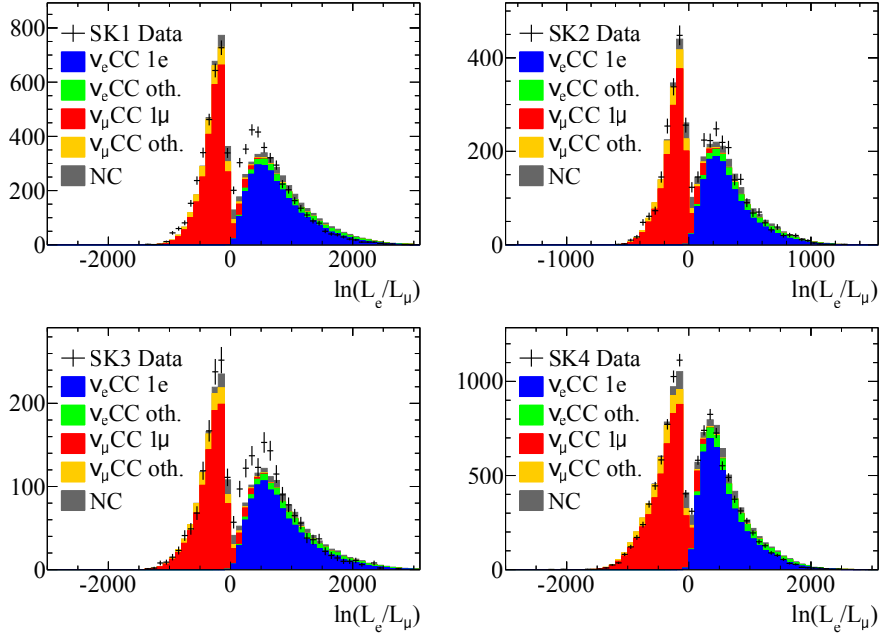


Figure C.3: Distributions of the PID log likelihood ratio ($\ln L_e/L_\mu$) of both the data (dots) and MC (stacked histograms) for the FC sub-GeV single-ring atmospheric neutrino events. Taken from [97].

Appendix D

Mass Production of Atmospheric Neutrino MC

In order to obtain the background rate for the $p \rightarrow e^+\pi^0$ analysis, we conventionally used the MC for 500 years of livetime for each SK which is 25 times longer than the current SK observation time. Since this analysis is very clean, the number of background events in the 500 years MC is low (around 10 events) and thus the statistical error is large. In addition to that, it is worth to check the difference of the background tendency between APfit and fitQun because it is the first time to apply fitQun to this analysis. Therefore, we need a statistically larger atmospheric neutrino MC event set for SK-IV. Taking into account the statistical error size and our computer resource (Process speed of fitQun multi-ring fit in our computer system is about 8.8 min/events for the preselected events described below), the target livetime is set to be 3000 years. We produce an additional 2500 years MC for SK-IV.

The following criteria are applied to the MC events before processing both APfit and fitQun since most of events are out of the signal region and it takes amount of time to process the event reconstruction;

1. NHITAC < 16,
2. 6,000p.e.s < PE_{tot} < 13,000p.e.s,
3. $\frac{|\sum_i q_i \vec{r}_i|}{PE_{tot}} < 0.5$,

where \vec{r}_i is a unit vector pointing to the i -th PMT which observes charge of q_i from a timing based fitted vertex. The first criterion is the one of the fully-contained cut. Since the energy region of proton decay is around 1 GeV, the second criterion is chosen so that both the signal and background events are contained with a margin as shown in Figure D.1. The third criterion represents the cut for an anisotropy in the observed charge of an event. Since a positron and a neutral pion are emitted back-to-back, the anisotropy of the signal events is

APPENDIX D. MASS PRODUCTION OF ATMOSPHERIC NEUTRINO
MC

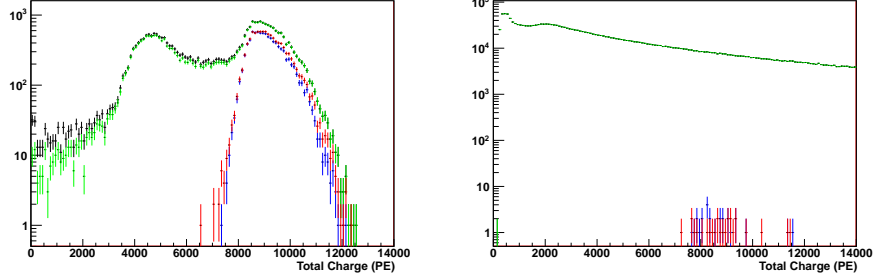


Figure D.1: Total observed charge distributions for the $p \rightarrow e^+\pi^0$ MC (left) and the 500 years atmospheric neutrino MC (right). The histograms are the original events (black), the events after the NHITAC cut (green), the final events selected by APfit without both the fiducial volume and neutron cut (blue) and the final events selected by fitQun without both the fiducial volume and neutron cut (red), respectively.

expected to be small while neutrino induced particles are boosted to the incident neutrino direction. Figure D.2 shows the anisotropy distributions. The fraction of survived background events is 3.5% after applying these criteria. After the preselection for $p \rightarrow e^+\pi^0$, both APfit and fitQun are applied and then the resultant 3000 years MC is then used in this analysis.

The validation of the preselection is done by comparing the nominal 500 years MC and the preselected 3000 years MC for both APfit and fitQun. Figure D.3 and D.4 show the reconstructed total momentum and invariant mass distributions. In these figures, the 3000 years MC is normalized by the livetime of the other MC. It can be seen the good agreement between both the MC inside and around the signal region. Thus, the preselection does not affect the distribution shape and the number of background events. Figure D.5 shows the total invariant mass and momentum scatter plots in the preselected 3000 years MC for APfit and fitQun after applying the selection criteria 1-5 for $p \rightarrow e^+\pi^0$ (not applied the neutron tagging cut).

APPENDIX D. MASS PRODUCTION OF ATMOSPHERIC NEUTRINO MC

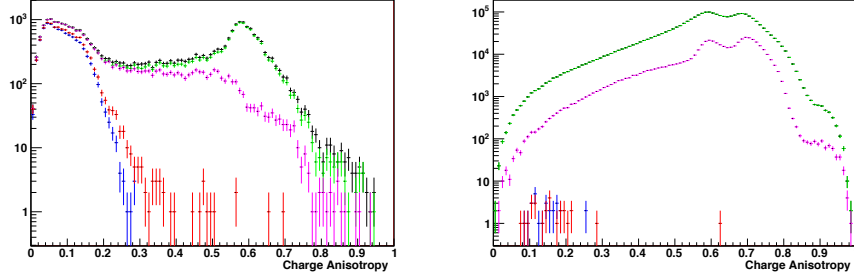


Figure D.2: Charge anisotropy distributions for the $p \rightarrow e^+\pi^0$ MC (left) and the 500 years atmospheric neutrino MC (right). The histograms are the original events (black), the events after the NHITAC cut (green), the events after the NHITAC and the total observed charge cut (purple), the final events selected by APfit without both the fiducial volume and neutron cut (blue) and the final events selected by fitQun without both the fiducial volume and neutron cut (red), respectively.

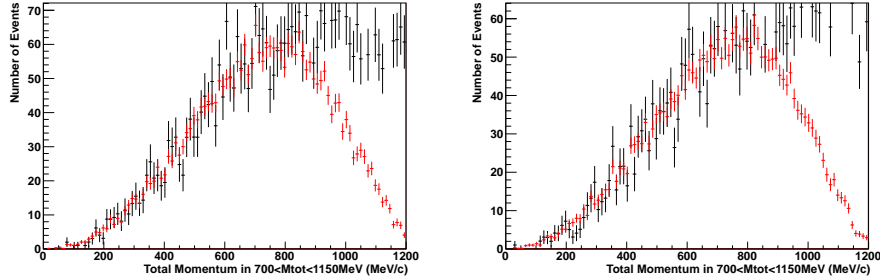


Figure D.3: Total momentum distributions in both the nominal 500 years (black) and preselected 3000 years (red) MC for fitQun (left) and APfit (right). The selection criteria 1-5 for $p \rightarrow e^+\pi^0$ and the $700 \text{ MeV} < M_{\text{tot}} < 1150 \text{ MeV}$ cut are applied.

APPENDIX D. MASS PRODUCTION OF ATMOSPHERIC NEUTRINO
MC

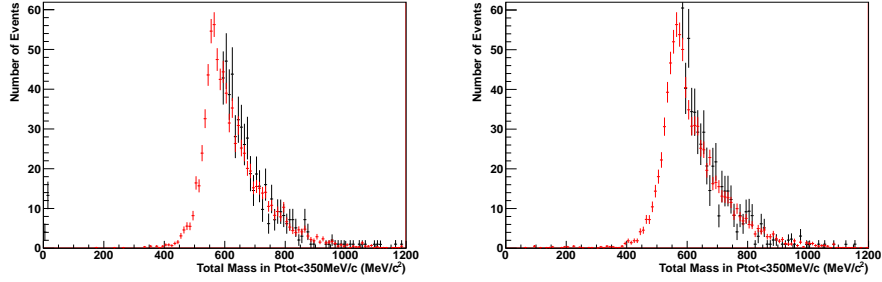


Figure D.4: Total invariant mass distributions in both the nominal 500 years (black) and preselected 3000 years (red) MC for fitQun (left) and APfit (right). The selection criteria 1-5 for $p \rightarrow e^+\pi^0$ and the $P_{\text{tot}} < 350$ MeV cut are applied.

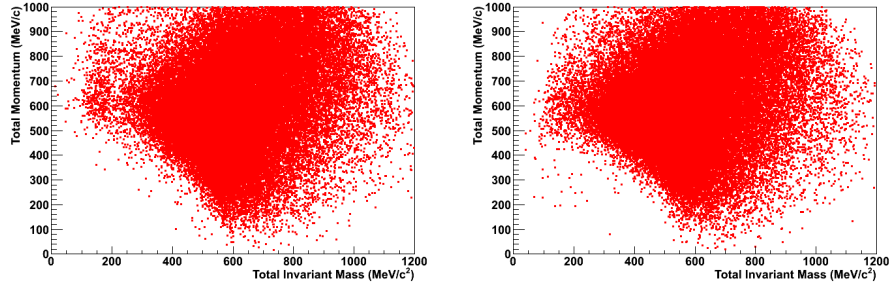


Figure D.5: Total invariant mass and momentum scatter plots in the preselected 3000 years MC for fitQun (left) and APfit (right). The selection criteria 1-5 for $p \rightarrow e^+\pi^0$ are applied.

Bibliography

- [1] K. Abe et al. “Search for proton decay via $p \rightarrow e^+\pi^0$ and $p \rightarrow \mu^+\pi^0$ in 0.31megatonyears exposure of the Super-Kamiokande water Cherenkov detector”. Phys. Rev., D95(1):012004, 2017.
- [2] B. P. Abbott et al. “Observation of Gravitational Waves from a Binary Black Hole Merger”. Phys. Rev. Lett., 116(6):061102, 2016.
- [3] G. Aad et al. “Observation of a new particle in the search for the Standard Model Higgs boson with the ATLAS detector at the LHC”. Phys. Lett., B716:1–29, 2012.
- [4] S. Chatrchyan et al. “Observation of a new boson at a mass of 125 GeV with the CMS experiment at the LHC”. Phys. Lett., B716:30–61, 2012.
- [5] Y. Fukuda et al. “Evidence for oscillation of atmospheric neutrinos”. Phys. Rev. Lett., 81:1562–1567, 1998.
- [6] H. F. Dylla and J. G. King. “Neutrality of Molecules by a New Method”. Phys. Rev., A7:1224–1229, 1973.
- [7] C. Patrignani et al. “Review of Particle Physics”. Chin. Phys., C40(10):100001, 2016.
- [8] H. Georgi and S. L. Glashow. “Unity of All Elementary Particle Forces”. Phys. Rev. Lett., 32:438–441, 1974.
- [9] P. Langacker. “Grand unification and the standard model”. arXiv, hep-ph/9411247.
- [10] P. Langacker and N. Polonsky. “Uncertainties in coupling constant unification”. Phys. Rev., D47:4028–4045, 1993.
- [11] U. Amaldi et al. “Comparison of grand unified theories with electroweak and strong coupling constants measured at LEP”. Phys. Lett., B260:447–455, 1991.
- [12] J. R. Ellis, S. Kelley, and D. V. Nanopoulos. “Probing the desert using gauge coupling unification”. Phys. Lett., B260:131–137, 1991.

BIBLIOGRAPHY

- [13] P. Langacker and M. Luo. “Implications of precision electroweak experiments for M_t , ρ_0 , $\sin^2 \theta_W$ and grand unification”. Phys. Rev., D44:817–822, 1991.
- [14] J. Hisano, H. Murayama, and T. Yanagida. “Nucleon decay in the minimal supersymmetric SU(5) grand unification”. Nucl. Phys., B402:46–84, 1993.
- [15] H. Murayama and A. Pierce. “Not even decoupling can save minimal supersymmetric SU(5)”. Phys. Rev., D65:055009, 2002.
- [16] S. P. Martin. “A Supersymmetry primer”. 1997. [Adv. Ser. Direct. High Energy Phys.18,1(1998)].
- [17] P. Minkowski. “ $\mu \rightarrow e\gamma$ at a Rate of One Out of 10^9 Muon Decays?”. Phys. Lett., B67:421–428, 1977.
- [18] T. Yanagida. “Horizontal Symmetry and Masses of Neutrinos”. Prog. Theor. Phys., 64:1103, 1980.
- [19] M. Gell-Mann, P. Ramond, and R. Slansky. “Complex Spinors and Unified Theories”. Conf. Proc., C790927:315–321, 1979.
- [20] H. Georgi. “The State of the Art Gauge Theories”. AIP Conf. Proc., 23:575–582, 1975.
- [21] H. Fritzsch and P. Minkowski. “Unified Interactions of Leptons and Hadrons”. Annals Phys., 93:193–266, 1975.
- [22] N. T. Shaban and W. James Stirling. “Minimal left-right symmetry and SO(10) grand unification using LEP coupling constant measurements”. Phys. Lett., B291:281–287, 1992.
- [23] D. Lee, R. N. Mohapatra, M. K. Parida, and M. Rani. “Predictions for proton lifetime in minimal nonsupersymmetric SO(10) models: An update”. Phys. Rev., D51:229–235, 1995.
- [24] H. Weyl. “Electron and Gravitation. I.”. Z. Phys., 56:330–352, 1929.
- [25] E. C. G. Stueckelberg. “Interaction forces in electrodynamics and in the field theory of nuclear forces”. Helv. Phys. Acta, 11:299–328, 1938.
- [26] E. P. Wigner. “Invariance in Physical Theory”. Am. Phil. Soc., 93:521, 1949.
- [27] F. Reines, C. L. Cowan, and M. Goldhaber. “Conservation of the number of nucleons”. Phys. Rev., 96:1157–1158, 1954.
- [28] S. P. Rosen. “Another Method of Searching for Proton Decay”. Phys. Rev. Lett., 34:774, 1975.

BIBLIOGRAPHY

- [29] G. N. Flerov, D. S. Klovkov, V. S. Skobkin, and V. V. Terent'ev. "Spontaneous fission of Th*232 and the stability of nucleons". Sov. Phys. Dokl., 3:79, 1958.
- [30] J. C. Evans, Jr. and R. I. Steinberg. "Nucleon Stability: A Geochemical Test Independent of Decay Mode". Science, 197:989–991, 1977.
- [31] E. L. Fireman. "Depth Dependence Of Ar-37 From K-39: Consequences For Solar Neutrino Experiments And The Baryon Conservation Principle.". pages 389–393, 1979.
- [32] C. L. Bennett. "Limitations on Proton Decay Modes from a Passive Detection Scheme". pages 120–124, 1981.
- [33] F. Reines, C. L. Cowan, and H. W. Kruse. "Conservation of the number of nucleons". Phys. Rev., 109:609–610, 1958.
- [34] G. K. Backenstoss et al. "An investigation of the stability of nucleons". Nuovo Cimento, 16:749–755, 1960.
- [35] C. C. Giamati and F. Reines. "Experimental test of the conservation of nucleons". Phys. Rev., 126:2178–2188, 1962.
- [36] W. R. Kropp and F. Reines. "Experimental test of baryon conservation and neutrino flux limits". Phys. Rev., 137:B740–B751, 1965.
- [37] H. S. Gurr, W. R. Kropp, F. Reines, and B. Meyer. "Experimental test of baryon conservation". Phys. Rev., 158:1321–1330, 1967.
- [38] L. Bergamasco and P. Picchi. "An Experimental Lower Limit on the Proton Lifetime". Nuovo Cim. Lett., 11:636, 1974.
- [39] F. Reines and M. F. Crouch. "Baryon conservation limit". Phys. Rev. Lett., 32:493–494, 1974.
- [40] J. Learned, F. Reines, and A. Soni. "Limits on Nonconservation of Baryon Number". Phys. Rev. Lett., 43:907, 1979. [Erratum: Phys. Rev. Lett.43,1626(1979)].
- [41] G. Battistoni et al. "Fully Contained Events in the Mont Blanc Nucleon Decay Detector". Phys. Lett., B118:461, 1982.
- [42] M. R. Krishnaswamy, M. G. K. Menon, N. K. Mondal, V. S. Narasimham, B. V. Sreekantan, Y. Hayashi, N. Ito, S. Kawakami, and S. Miyake. "Results From the Kgf Proton Decay Experiment". Nuovo Cim., C9:167–181, 1986. [Conf. Proc.C850418,97(1985)].
- [43] John E. Bartelt et al. "Monopole Flux and Proton Decay Limits From the Soudan-i Detector". Phys. Rev., D36:1990, 1987. [Erratum: Phys. Rev.D40,1701(1989)].

BIBLIOGRAPHY

- [44] Christoph Berger et al. “Results from the Frejus experiment on nucleon decay modes with charged leptons”. Z. Phys., C50:385–394, 1991.
- [45] M. L. Cherry, M. Deakayne, K. Lande, C. K. Lee, R. I. Steinberg, and B. T. Cleveland. “Experimental Test of Baryon Conservation: A New Limit on the Nucleon Lifetime”. Phys. Rev. Lett., 47:1507–1510, 1981.
- [46] C. McGrew et al. “Search for nucleon decay using the IMB-3 detector”. Phys. Rev., D59:052004, 1999.
- [47] K. S. Hirata et al. “Experimental Limits on Nucleon Lifetime for Lepton + Meson Decay Modes”. Phys. Lett., B220:308–316, 1989.
- [48] M. Shiozawa et al. “Search for proton decay via $p \rightarrow e^+ \pi^0$ in a large water Cherenkov detector”. Phys. Rev. Lett., 81:3319–3323, 1998.
- [49] H. Nishino et al. “Search for Nucleon Decay into Charged Anti-lepton plus Meson in Super-Kamiokande I and II”. Phys. Rev., D85:112001, 2012.
- [50] K. Abe et al. “Search for proton decay via $p \rightarrow \nu K^+$ using 260kilotonyear data of Super-Kamiokande”. Phys. Rev., D90(7):072005, 2014.
- [51] Y. Fukuda et al. “The Super-Kamiokande detector”. Nucl. Instrum. Meth., A501:418–462, 2003.
- [52] R. Becker-Szendy et al. “IMB-3: A Large water Cherenkov detector for nucleon decay and neutrino interactions”. Nucl. Instrum. Meth., A324:363–382, 1993.
- [53] H. Ikeda et al. “Front end hybrid circuit for Super-Kamiokande”. Nucl. Instrum. Meth., A320:310–316, 1992.
- [54] H. Nishino et al. “High-speed charge-to-time converter ASIC for the Super-Kamiokande detector”. Nucl. Instrum. Meth., A610:710–717, 2009.
- [55] K. Abe et al. “Calibration of the Super-Kamiokande Detector”. Nucl. Instrum. Meth., A737:253–272, 2014.
- [56] R. Pope and E. Fry. “Absorption spectrum (380-700 nm) of pure water. II. Integrating cavity measurements”. Applied Optics, 33:8710–8723, 1997.
- [57] K. Nakamura et al. “The Reaction C-12 (e, e’ p) at 700-MeV and DWIA Analysis”. Nucl. Phys., A268:381–407, 1976.
- [58] T. Yamazaki and Y. Akaishi. “Nuclear medium effects on invariant mass spectra of hadrons decaying in nuclei”. Phys. Lett., B453:1–6, 2000.
- [59] Y. Hayato. “NEUT”. Nucl. Phys. Proc. Suppl., 112:171–176, 2002.
- [60] L. L. Salcedo et al. “Computer Simulation of Inclusive Pion Nuclear Reactions”. Nucl. Phys., A484:557–592, 1988.

BIBLIOGRAPHY

- [61] P. de Perio. “NEUT pion FSI”. *AIP Conf. Proc.*, 1405:223–228, 2011.
- [62] G. Rowe, M. Salomon, and R. H. Landau. “An Energy Dependent Phase Shift Analysis of Pion - Nucleon Scattering Below 400-MeV”. *Phys. Rev.*, C18:584–589, 1978.
- [63] R. D. Woods and D. S. Saxon. “Diffuse Surface Optical Model for Nucleon-Nuclei Scattering”. *Phys. Rev.*, 95:577–578, 1954.
- [64] H. Ejiri. “Nuclear deexcitations of nucleon holes associated with nucleon decays in nuclei”. *Phys. Rev.*, C48:1442–1444, 1993.
- [65] M. Honda et al. “Calculation of atmospheric neutrino flux using the interaction model calibrated with atmospheric muon data”. *Phys. Rev.*, D75:043006, 2007.
- [66] M. Honda et al. “Improvement of low energy atmospheric neutrino flux calculation using the JAM nuclear interaction model”. *Phys. Rev.*, D83:123001, 2011.
- [67] J. Alcaraz et al. “Cosmic protons”. *Phys. Lett.*, B490:27–35, 2000.
- [68] J. Alcaraz et al. “Helium in near Earth orbit”. *Phys. Lett.*, B494:193–202, 2000.
- [69] T. Sanuki et al. “Precise measurement of cosmic ray proton and helium spectra with the BESS spectrometer”. *Astrophys. J.*, 545:1135, 2000.
- [70] S. Haino et al. “Measurements of primary and atmospheric cosmic - ray spectra with the BESS-TeV spectrometer”. *Phys. Lett.*, B594:35–46, 2004.
- [71] K. Niita et al. “PHITS: A particle and heavy ion transport code system”. *Radiat. Meas.*, 41:1080–1090, 2006.
- [72] S. Roesler et al. “The Monte Carlo event generator DPMJET-III”. *arXiv*, hep-ph/0012252:1033–1038, 2000.
- [73] G. Battistoni et al. “The FLUKA atmospheric neutrino flux calculation”. *Astropart. Phys.*, 19:269–290, 2003. [Erratum: *Astropart. Phys.*19,291(2003)].
- [74] G. D. Barr et al. “A Three - dimensional calculation of atmospheric neutrinos”. *Phys. Rev.*, D70:023006, 2004.
- [75] J. A. Formaggio and G. P. Zeller. “From eV to EeV: Neutrino Cross Sections Across Energy Scales”. *Rev. Mod. Phys.*, 84:1307–1341, 2012.
- [76] S. Jadach et al. “The tau decay library TAUOLA: Version 2.4”. *Comput. Phys. Commun.*, 76:361–380, 1993.

BIBLIOGRAPHY

- [77] T. J. Irvine. “Development of Neutron-Tagging Techniques and Application to Atmospheric Neutrino Oscillation Analysis in Super-Kamiokande”. Ph. D. Thesis, University of Tokyo, 2014.
- [78] C. H. Llewellyn Smith. “Neutrino Reactions at Accelerator Energies”. Phys. Rept., 3:261–379, 1972.
- [79] R. A. Smith and E. J. Moniz. “NEUTRINO REACTIONS ON NUCLEAR TARGETS”. Nucl. Phys., B43:605, 1972. [Erratum: Nucl. Phys.B101,547(1975)].
- [80] R. Gran et al. “Measurement of the quasi-elastic axial vector mass in neutrino-oxygen interactions”. Phys. Rev., D74:052002, 2006.
- [81] A. A. Aguilar-Arevalo et al. “First Measurement of the Muon Neutrino Charged Current Quasielastic Double Differential Cross Section”. Phys. Rev., D81:092005, 2010.
- [82] J. Nieves, I. Ruiz Simo, and M. J. Vicente Vacas. “Inclusive Charged-Current Neutrino-Nucleus Reactions”. Phys. Rev., C83:045501, 2011.
- [83] D. Rein and L. M. Sehgal. “Neutrino Excitation of Baryon Resonances and Single Pion Production”. Annals Phys., 133:79–153, 1981.
- [84] K. M. Graczyk and J. T. Sobczyk. “Form Factors in the Quark Resonance Model”. Phys. Rev., D77:053001, 2008. [Erratum: Phys. Rev.D79,079903(2009)].
- [85] C. Wilkinson et al. “Reanalysis of bubble chamber measurements of muon-neutrino induced single pion production”. Phys. Rev., D90(11):112017, 2014.
- [86] D. Rein and L. M. Sehgal. “Coherent π^0 Production in Neutrino Reactions”. Nucl. Phys., B223:29–44, 1983.
- [87] M. Glck, E. Reya, and A. Vogt. “Dynamical parton distributions revisited”. Eur. Phys. J., C5:461–470, 1998.
- [88] A. Bodek and U. K. Yang. “Modeling neutrino and electron scattering cross-sections in the few GeV region with effective LO PDFs”. AIP Conf. Proc., 670:110–117, 2003. [110(2003)].
- [89] M. Derrick et al. “Properties of the Hadronic System Resulting from anti-Muon-neutrino p Interactions”. Phys. Rev., D17:1, 1978.
- [90] S. Barlag et al. “Charged Hadron Multiplicities in High-energy Anti-muon Neutrino n and Anti-muon Neutrino p Interactions”. Z. Phys., C11:283, 1982. [Erratum: Z. Phys.C14,281(1982)].
- [91] T. Sjostrand. “PYTHIA 5.7 and JETSET 7.4 physics and manual”. 1994.

BIBLIOGRAPHY

- [92] R. Brun et al. “GEANT3”. 1987.
- [93] C. Zeitnitz and T. A. Gabriel. “The GEANT - CALOR interface and benchmark calculations of ZEUS test calorimeters”. Nucl. Instrum. Meth., A349:106–111, 1994.
- [94] R. B. Patterson and others. “The Extended-track reconstruction for Mini-BooNE”. Nucl. Instrum. Meth., A608:206–224, 2009.
- [95] M. Shiozawa. “Reconstruction algorithms in the Super-Kamiokande large water Cherenkov detector”. Nucl. Instrum. Meth., A433:240–246, 1999.
- [96] H. Nishino. “Search for Nucleon Decay into Charged Antilepton plus Meson in Super-Kamiokande”. Ph. D. Thesis, University of Tokyo, 2009.
- [97] S. Tobayama. “An Analysis of the Oscillation of Atmospheric Neutrinos”. Ph. D. Thesis, University of British Columbia, 2016.
- [98] S. Mine et al. “Experimental study of the atmospheric neutrino backgrounds for $p \rightarrow e^+\pi^0$ searches in water Cherenkov detectors”. Phys. Rev., D77:032003, 2008.
- [99] Y. Ashie et al. “A Measurement of atmospheric neutrino oscillation parameters by SUPER-KAMIOKANDE I”. Phys. Rev., D71:112005, 2005.
- [100] G. Mitsuka. “Study of Non-Standard Neutrino Interactions with Atmospheric Neutrino Data in Super-Kamiokande”. Ph. D. Thesis, University of Tokyo, 2009.
- [101] K. Abe *et al.* “Hyper-Kamiokande Design Report”. KEK-PREPRINT-2016-21, ICRR-REPORT-701-2016-1, 2016.
- [102] G. Cowan et al. “Asymptotic formulae for likelihood-based tests of new physics”. Eur. Phys. J., C71:1554, 2011. [Erratum: Eur. Phys. J.C73,2501(2013)].